Quantitative Ion Spectrometry and first laser-ion acceleration results at the Centre for Advanced Laser Applications

Jens Hartmann

München 2022

Quantitative Ion Spectrometry and first laser-ion acceleration results at the Centre for Advanced Laser Applications

Jens Hartmann

Dissertation
an der Fakultät für Physik
der Ludwig–Maximilians–Universität
München

vorgelegt von
Jens Hartmann
geboren in Dillingen an der Donau

München, den 3. Juni 2022

Erstgutachter: Prof. Dr. Jörg Schreiber

Zweitgutachter: Prof. Dr. Peter Thirolf

Tag der mündlichen Prüfung: 27. Juli 2022

Contents

List of Figures

List of Tables

Zusammenfassung

Diese Arbeit beschreibt den ersten Forschungsabschnitt der laserbasierten Beschleunigung von Ionenstrahlen in Plasmen am Centre for Advanced Laser Applications in Garching bei München. Das laserbasierte Ionenbeschleunigungssystem basiert auf dem gechirpten Pulsverstärkersystem 'Advanced-Titanium:Saphire-Laser' (ATLAS), das in naher Zukunft in der Lage sein wird, Femtosekundenpulse mit mehr als 1 Petawatt Spitzenleistung zu liefern. Die hier vorgestellten Ergebnisse basieren auf Bestrahlungsstudien von nanometerdünnen Filmen mit reduzierter Spitzenleistung von bis zu 300 TW. Auf dieser Grundlage wurde die Laser-Ionen-Beschleunigungsbeamline (LION) entwickelt und in Betrieb genommen, die nun eine reproduzierbare Protonenbeschleunigung auf kinetische Energien von bis zu 23 MeV ermöglicht.

Eine neuartige Technik der quantitativen Ionenspektrometrie (QIS) wurde entwickelt, um absolute differentielle Energiespektralinformationen der beschleunigten Ionen zu erhalten. Es wird gezeigt, wie ein pixelierter Siliziumdetektor nur unter der Berücksichtigung der statistischen Natur des Energieverlustes von Teilchen in der dünnen Dektorschicht für Protonen und Kohlenstoffionen kalibriert werden kann. Dieser Ansatz wird um die Verteilung der Teilchen auf einzelne Pixel erweitert, was die Bestimmung der absoluten Teilchenzahl ohne vorherige detaillierte Kenntnis des Sensors ermöglicht. Simulationen zeigen, dass diese Methode in einem Bereich zwischen sehr niedrigem Teilchenfluss (Einzelteilchen) und sehr hohem Teilchenfluss (nahe Sättigung) am besten funktioniert. Daher kann QIS das eminente Problem der quantitativen Detektorkalibrierung lösen, sogar nach einer Experimentkampagne.

Die QIS-Methode wurde zur quantitativen Auswertung der Protonen- und Kohlenstoffionendaten von 42 ausgewählten Laserschüssen auf 400 nm-Targets verwendet. Das Hauptaugenmerk lag auf der Stabilität der Protonenteilchenzahl bei Energien von 12, 15 und 18 MeV. Es wurden zwei Arten von Variationen identifiziert. Wir beobachten einen Winkelbereich von 2° innerhalb des emittierten Strahls und beobachten Teilchenzahlschwankungen um bis zu einem Faktor zwei innerhalb einzelner Schüsse.

Über mehrere Schüsse hinweg divergiert die winkelgemittelte Teilchenzahl um bis zu drei Größenordnungen, was einem An-Aus-Verhalten ähnelt, das vor allem in der Nähe der maximalen Protonenenergie zu beobachten ist. Die Schuss-zu-Schuss-Fluktuationen der Protonenausbeute gingen bei 7 MeV auf eine Größenordnung zurück. Gelegentlich wurde beobachtet, dass Kohlenstoffionen effizient mit Protonen mitbeschleunigt wurden und kinetische Energien von 23 MeV/u erreichten.

Diese Arbeit lieferte die Grundlage für Anwendungsexperimente bei moderater Teilchenenergie, insbesondere durch die Einrichtung einer Strahlführung für den Transport von laserbeschleunigten Protonen zu einer Plattform an Luft. Erste Demonstrationsexperimente umfassen Fokussierung von Protonen, Detektortests und eine Protonenradiographie.

Abstract

This work describes the first research period of laser-based acceleration of ion beams in plasmas at the Centre for Advanced Laser Applications in Garching near Munich. The laser-driven ion acceleration system relies on the chirped pulse amplification Advanced-Titanium:Saphire-Laser (ATLAS) system, which will be able to deliver femtosecond pulses with more than 1 Petawatt peak power in the near future. Findings presented here rely on irradiation studies of nanometer-thin films with reduced peak power of up to 300 TW. On this basis, the laser-ion (LION) acceleration experimental beamline was developed and put into operation and now enables reproducible proton acceleration to kinetic energies of up to 23 MeV.

A novel Quantitative Ion Spectrometry (QIS) technique was developed to obtain absolute differential energy spectral information of the accelerated ions. It is shown how a pixelated silicon detector can be calibrated for protons and carbon ions only by considering the statistical nature of the energy loss of particles in the thin detector layer. This approach is extended to include the distribution of particles over individual pixels, which allows the absolute number of detected particles to be determined without prior detailed knowledge of the sensor. Simulations show that this method works best in a range between very low particle flux (single particles) and very high particle flux (near saturation). Therefore, QIS can solve the eminent problem of quantitative detector calibration, even posterior of experimental campaigns.

The QIS method was used to evaluate quantitatively the proton and carbon ion data of 42 selected laser shots on 400 nm targets. Main focus was on the stability of the proton particle number at energies of 12, 15, and 18 MeV. Two kinds of variations were identified. We access an angular range of 2° within the emitted beam and observe particle number fluctuations by up to a factor of two within individual shots. Over multiple shots, angle-averaged particle numbers diverge by up to three orders of magnitude, resembling an on-off behavior that is mostly observed near the maximum proton energy. The shot-to-shot fluctuations of the proton yield reduced to one order

of magnitude at 7 MeV. It was occasionally observed that carbon ions were efficiently co-accelerated with protons and reached kinetic energies of 23 MeV/u.

The work provided the basis for application experiments at moderate particle energy, in particular by establishing a beamline for transporting laser-accelerated protons to a platform in air. First demonstration experiments include proton focusing, detector tests and a proton radiography.

Chapter 1

Introduction

The groundbreaking work in nuclear physics at the beginning of the 20th century was fueled by experiments with moving particles. The understanding of a nucleus as concentrated charge in the center of the atom was derived from scattering experiments of Rutherford, Geiger and Marsden [1]. These experiments used the natural α-decay of radioactive Radium as their particle source which limited their kinetic energy and particle flux. It took Rutherford two days of irradiating a glass tube with α-particles to demonstrate that these are in fact charged Helium nuclei [2]. However, such results sparked interest in increasing the kinetic energy and flux of the irradiation particles, and the idea of an artificial source, a particle accelerator, developed.

A charged particle is attracted by its opposite charge. If placed inside a charged capacitor with an applied voltage potential, it will drift along the electric field towards the plate with opposite charge whilst gaining kinetic energy. Decreasing the width of the capacitor gap, as well as increasing the charge on its plates will increase the electric field strength. The limitation of such constant field accelerators soon became apparent, but the main concept remains also for alternating fields. The linear accelerator is based on the same principle and its first demonstration was done by Wideröe [3]. It consisted of a tube shaped vacuum vessel, which had a thermal emission tube on one end, and two adjacent metal tubes, separated by a narrow gap. Opposite charges where applied to these tubes by an alternating voltage source. Slowly moving particles from thermal emission were attracted towards the entrance of the first tube, and entered it. Inside the tube the potential was shielded, and the particle continued ballistically with constant speed. The alternating voltage source was adjusted such that it could finish a complete charge reversal while the particle was still inside the tube. As it arrived at the gap between the tubes, it was accelerated again by the potential in the gap between the

first and second tube [3].

Additional tubes will accelerate the particle further to higher speeds, but also enlarge the device. This can be countered by reducing the drift tube length. Increased particle speed and shorter tubes result in less time to switch the voltage, thus demand higher frequencies for the voltage source. Current radio-frequency cavity structures operate at MHz to GHz and generate fields on the order of megavolts per meter.

Particles with MeV kinetic energies are of great interest for research and industry. These would ideally be accelerated by small, maybe even mobile, machines on the laboratory table. Recently, a radio-frequency structure operating at 750 MHz has demonstrated the acceleration from incident keV protons to 5 MeV, bunching to 250 µs duration and focusing to a 1 mm diameter spot. It has been optimized to be used for non-destructive in-situ analysis of cultural heritage using Proton Induced X-ray Emission (PIXE). This accelerator has been designed to be movable and compact, with a length of 2 m [4].

Reducing the accelerator size further by increasing field strength is limited by discharges at high voltages, increasing the driver frequency above tens of GHz is complicated by the current lack of efficient and powerful sources of electromagnetic fields. Lasers, however, operate at tens of THz frequency. They can achieve high peak power using the concept of Chirped-Pulse Amplification (CPA) [5], for which Strickland and Mourou received the Nobel Prize in 2018. Continuous development of CPA lasers enabled petawatt laser pulse peak power. In a laser focus, the coherent nature of laser light results in strong peak fields, and thus high acceleration potential, allowing field gradients to the order of teravolt per meter.

Employing these high fields for acceleration requires to rethink the accelerator design. The related light intensities above $10^{18}\,\mathrm{W\,cm^{-2}}$ in the laser focal spot are well above ionization thresholds for all matter. Thus, the matter in the volume in which the acceleration field is present is almost instantly converted into a plasma state and the target material has to be replaced for the next 'laser shot'. Particle motion inside this plasma primarily is governed by the electromagnetic field of the laser pulse and can lead to plasma fields due to collective motion. Based on the idea of coherent acceleration by Veksler [6], Tajima theoretically examined laser-driven particle acceleration in a plasma. In his theoretical work, a laser pulse with an intensity of $10^{18}\,\mathrm{W\,cm^{-2}}$ traversed the plasma and accelerated electrons in its wake [7]. This process is now referred to as 'laser wakefield acceleration' and has made tremendous progress in developing towards a laser-plasma accelerator [8].

The laser-plasma source can also accelerate heavier charged particles, such as ions. The irradiation of a 100 µm thick foil with the first available petawatt pulse resulted in protons with kinetic energies up to 58 MeV in 2000 [9]. This sparked interest into laser-driven acceleration of ions and started many investigations into their improvements. Yet, in contrast to electrons, even nowadays available laser intensities are insufficient to accelerate ions to relativistic speed in a well structured acceleration potential. Instead, the laser-driven source is a microscopic high-energy-density plasma much like a (very hot) emission anode, but with a variety of unique features: Ions, electrons and photons are co-emitted simultaneously from the same spot, which can be controlled to some extent by target composition and treatment. Ions originate from a micrometer small volume with a divergence half angle between a few to a few tens of degrees. The emitted ions obey a broad exponentially decaying spectrum which can be characterized by a maximum energy E_{max}. The initial ion-bunch duration is on the order of the laser pulse duration, but increases during propagation due to dispersion. Laser-accelerated solid-state density ion bunches are a key element to the fission-fusion reaction process which can improve the insight on nuclear astrophysical processes [10]. The laser-driven source also offers the unique availability of synchronized laser pulses that can be used as probes [11].

In particular this availability of synchronized particle bunches and photon pulses offers many possibilities. For example, plasmas can be probed by accelerated protons [11]. The laser can drive strong currents to induce magnetic fields, which can be measured by protons [12]. Laser-driven plasmas can serve as Gabor lenses for electrons [13] and protons [14]. The multi-modal simultaneous emission of protons and x-rays has also been used for combined imaging [15]. The large angular emission allows for analyzing larger surface areas in material analysis, such as PIXE [16]. Converting the short ion bunch into a short neutron bunch allows for good time resolution in time-of-flight-based material analysis [17]. The laser-driven source enables energy deposition of fast protons in water on a pico-second scale and, combined with a synchronized laser probe pulse, allows to investigate the ultrafast mechanisms in proton water radiolysis [18] [19].

However, establishing the basis for exploring new application possibilities or considering the plasma as a source for further acceleration (a photo anode) requires quantitative knowledge of the parameters of the emitted bunch. While the maximum energy E_{max} is a useful performance parameter, applications require information of particle numbers within a certain energy interval. Extracting this data from a very large va-

riety of experimental campaigns is not yet standardized and requires partly laborious calibration effort. Typically cross-calibration employs single-use CR-39 detectors [20]. CR-39 is a transparent plastic in which single-ion impacts become visible under a microscope after a laborious etching process, which of course has to be repeated for every exposed CR-39 plate.

Once the source is quantified, tailored beamlines are required to relay and prepare the ion bunch for applications. Magnetic dipole fields introduce angular dispersion based on the incident particle charge to mass ratio and speed. This can be used for particle detection [21] [22] or for narrowing the energy spread [23] [24]. Magnetic quadrupole fields allow to focus or de-focus an ion-bunch spatially and pulsed solenoids [25] as well as permanent magnets [26] [27] have been demonstrated. Such ion-beam transport devices are essential for applications, such as the proton beam based tumor treatment [28]. A phase space rotator can recover the initial short bunch duration for an energy range at the application, and has been successfully demonstrated for 9.55 MeV and 500 ps duration proton bunches focused to a focal spot size of 1.1 x 1.2 mm [29]. Important steps have been made towards biological and medical application, in particular the recent demonstration of a suitable stable setup for small animal irradiation with ≈ 20 MeV protons [30] and consequently the first mouse irradiation study has been performed [28]. Demonstrated maximum kinetic proton energies do not increase significantly, although ≈ 90 MeV have meanwhile been demonstrated [31] [32] with laser systems smaller than the first petawatt machine. It is still debated whether human proton therapy treatment, which requires around 200 MeV proton energy [33], can be performed on the basis of laser-driven acceleration.

Developing laser-driven particle acceleration for providing new tools for medical physics, in particular diagnostics and therapy, has been one research area of the Munich-Centre for Advanced Photonics (MAP) [34]. This excellence cluster provided the basis for developments at LMU and the Max-Planck Institute for Quantum Optics (MPQ) from 2006 to 2019. Up to 2014 Laser-driven ION (LION) experiments have been carried out at the Advanced Titanium Saphire Laser (ATLAS)-10 (10 TW peak power) operated at MPQ. The laser was then moved to the Laboratory of Extreme (LEX) Photonics, in Garching near Munich, upgraded to 300 terawatt peak power in 2014. Regular LEX-LION experiments at this ATLAS-300 system during 2015 and 2016 have been investigating diverse branches of laser-driven sources. The setup has been used to demonstrate a high-repetition rate target system [35], ion-bunch transport [27], first detection of laser-driven protons with water [36] and the first irradiation

of zebrafish embryos with laser-driven protons [37]. Research into the spatial distribution of the laser focus [38] and plasma development [39] as well as experiments with pulse cleaning [40] added new insights in laser-plasma dynamics. Further information on the work done during this time can be found in [41] [42].

Irradiation experiments in LEX-LION have been limited by proton $E_{max} \approx 8\,\mathrm{MeV}$, mainly due to two detrimental pre-pulses that originated from the regenerative amplifier in the laser chain [41].

LEX Photonics has since been extended into a larger laboratory, the Centre for Advanced Laser Applications (CALA), which is depicted schematically in figure 1.1.

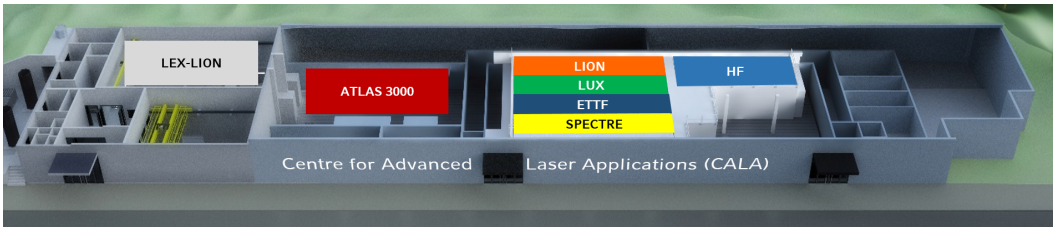

Figure 1.1: Overview of the Centre for Advanced Laser Applications (CALA). The left third of the building (CALA minor) containing LEX-LION has already been used for experiments in 2015-2016. The extension of the building (CALA major) has been finished in late 2016.

This thesis work has begun in February 2017, right after the construction work of the CALA building [43] had been completed.

While the laser as well as experiments had previously been restricted to the room marked as 'LEX-LION', the extension allowed for significant upgrades, in particular increasing the ATLAS peak power by a factor of ten to 3 PW. The upgrade also included a replacement of the regenerative amplifier with a ring-cavity design, which eliminated detrimental pre-pulses.

Five different Experimental BeamLines (EBL) situated in their respective radiation protection caves can be supplied with laser pulses. Three are considered for electron acceleration and related generation of radiation: The Laser-driven Undulator X-Ray Source (LUX), the Electron and Thomson Test Facility (ETTF), and the Source for Powerful Energetic Compact Thomson Radiation Experiments (SPECTRE). The High Field (HF) Physics EBL is designated to fundamental research, in particular in the commissioning for heavy ion-acceleration as a tool for investigating the r-process via ultra-fast fission-fusion processes in dense plasmas [10]. The LION EBL currently concentrates on the acceleration of proton and carbon bunches. Its design relies on the experiences and developments made in LEX Photonics and before. Its practical

setup and the realization of the design constituted a major part of this thesis work.

Thesis contents This thesis reports on the first two years of ion acceleration at the LION EBL in CALA, based on the ATLAS system with laser pulses up to 300 TW peak power. Up to 400 shots per venting cycle have been achieved and ion energy distributions spectra extended up to $E_{max} \approx 23\,\mathrm{MeV}$ proton and up to $E_{max} \approx 22\,\mathrm{MeV/u}$ for carbon ions. The integrated ion-bunch transport system demonstrated proton foci with diameters down to several hundred micrometer. This setup is the basis for future applications of which some have been already tested. The main focus was on quantifying the ion source performance, and for doing so, a new approach for quantitatively evaluating pixelated thin-film detectors has been developed and investigated in depth. Using the single-proton sensibility of the RadEye1 detector, this method does only rely on basic physical principles and does not require a cumbersome reference calibration from a known particle source. The new method compares well to to an older evaluation approach based on calibrated detectors, though raising the question of ground truth.

Chapter 2 explains the experimental equipment. The generation of high-intensity laser pulses by ATLAS and their transport to the experiment is explained. Setup and integration of the LION laser-plasma interaction chamber are described. The main focus is on the ion diagnostic setup.

Chapter 3 will provide physical background and theoretical concepts for evaluating the presented experimental data. First, laser-driven ion acceleration will be framed to highlight the properties of emitted particle bunches and associated diagnostic tools. Particular emphasis in this thesis setup is on the deflection by a magnetic dipole with in-homogeneous field, for which the amount of deflection with respect to kinetic energy is modeled. The working principle of the employed silicon detector is explained. The amount of deposited energy in thin layers will be explained, as well as their statistical distribution. This feature is important for understanding the core of our evaluation method dubbed Signal Distribution Function (SDF). Finally, simulations show the performance of this new method and introduce validity constraints.

Chapter 4 describes the new approach of our Quantitative Ion Spectrometry (QIS). It is based on the statistical response of pixelated detectors on protons and carbon ions with energies up to 23 MeV/u. Combined with the theoretical understanding of the expected energy loss distribution of particles, the number of ions on the detector surface is calculated. This enables evaluation of the differential kinetic energy distribution. Current limits for application to higher proton energies at low

signal levels as well as potential causes and improvements are discussed. The new calibration method is compared to the single calibration factor that was used as of now.

Chapter 5 presents recent results obtained at LION and their evaluation in the framework of QIS. The achieved performance enabled proton bunch transport with magnetic quadrupoles and a simple demonstration of proton imaging.

Chapter 6 discusses the results, in particular the relevance of QIS in light of higher ion energies that are expected for increased laser power, and puts the LION performance in broader context to laser ion acceleration results achieved in other laboratories.

Chapter 2

LION at CALA

We will start this chapter with a recap of the timeline from 2017 to 2022. Then we will describe the setup of the ATLAS 3000 laser which drives the high-intensity laser-plasma experiments in CALA. We will explain how laser pulses are distributed via the Laser Beamline Delivery (LBD). Finally, the LION experiment and its diagnostics relevant for this work will be presented.

2.1 History and Development

Figure 2.1: Setup of the LION experiment at CALA over the course of this thesis. The CALA building was finished in 2016, frames for the vacuum chambers arrived in 2017. First ions could be demonstrated in June 2019. Picture from [41].

This thesis started right after the previous LION experiment at the LEX Photonics laboratory had been disassembled. The images in figure 2.1 are representative for the progress since then. One of the first tasks has been moving experiment devices from LEX Photonics to CALA. These new laboratories had to be prepared by setting up

basic infrastructure such as power, telephones and local area network access. The laboratory was equipped with cupboards and workbenches. We have planned diagnostic and testing setups and ordered their respective parts, such as oscilloscopes, computers and software, etc.

With the arrival of the vacuum chambers in late 2017 first tests could be done. Tightness of the vacuum chambers without and with planned feedthroughs was confirmed. Quadrupole mass spectrometers allowed repeated measurements of total and partial pressures associated with hydrocarbons confirmed that the system stayed within the specified defined upper limits. Dose rates from primary and secondary radiation of the experiment have been calculated using FLUKA [44][45] simulations [46]. Based on these calculations, a composite beamdump has been designed, ordered and installed. It is positioned adjacent to the vacuum chamber, on axis with the main propagation direction for the laser-accelerated ion beams. The simulations have been summarized and prepared for submission to obtain the operation permit for the experiments. This permit has been granted in 2018.

Meanwhile, preparations for the experimental setup progressed as well. All motorized mirror mounts where custom made to fit the substrates for the 28 cm diameter laser beam. After their manufacturing these had to be cleaned, assembled, tested with dummy weights and revised for a second design iteration. The LBD is a network of mirrors inside vacuum tubes that connects the laser-hall and the EBL. First, two parallel pilot beams, spaced 28 cm apart, have been used to confirm that a full aperture laser beam can propagate through the LBD. Then, a centered pilot beam was sent from through the LBD to measured position jitter at its destination. This allowed to pin point several vibrational coupling issues within the LBD and resulted in moving vacuum pumps to different locations and identifying problems with malfunctioning decouplings. The remaining jitter of this pilot beam focus was on the order of one focal spot. For ease of use and alignment the difference between the system state 'full vacuum' and 'on air' should be as small as possible. During vacuum tests it was noticed that the mirror holder in the last LBD vacuum chamber, designated 'W1', was moving too much to be tolerable. This movement has been sufficiently suppressed with additional reinforcements of the breadboard holder, fixing it tightly to the buildings base plate.

As the experiment is completely enclosed in the vacuum chamber, all devices requiring fine adjustment had to be motorized connected via manufactured vacuum compatible cables. Cables from the previous setup have been tested and refurbished

before re-usage. Cable feedthroughs are required to bridge cables between air and vacuum side. These had to be tested for electrical conductivity and for vacuum leakage. With increasing complexity of the setup, the number of cables also increases, which can make troubleshooting electrical issues very complicated. Due to bad experiences with rapid cable growth in the previous setup, a plan had been devised for cabling. A secondary framework of aluminum construction profiles have been installed inside the framework of the vacuum chambers. This allowed to easily mount a variety of equipment. Two large cable channels have been installed in the framework of the vacuum chamber, spanning its complete length: One designated for 230 V power supply cables, and the other for device control and signal cables. Several 230 V distributors had been fixed along the framework to shorten power cable lengths. These were each connected to separate outlets of the building, distributing the power load over several fuses. Three motor controls, each controlling between five and ten motor axis, have been distributed along the chamber length to allow for short cable runs. They have been fixed into the aluminum framework as well. Additional devices and controllers that are part of the general experimental setup are also fixed inside this frame. Most of these controllers can either be directly connected via Ethernet, or require a connection to a computer, which in turn is connected to the local area network. Two 16 port network switches deliver just enough ports for these connections. A smaller 8 port switch is dedicated to general setup cameras. The two main switches are connected to the building network via two separate LAN lines from the next largest hub. For cabling in general it is important to enforce these structures with an expanding setup. This allows for increased reliability and simplified troubleshooting.

The software infrastructure was built on an Ethernet bus system, TANGO Controls [47]. It is an open-source framework bus-system that has been established for particle accelerator control. Based on a code already in use during the LEX Photonics experiments, this had been expanded to incorporate most devices in the setup. The benefits are best explained with the motor control example. In the previous setup, one computer had been directly connected with a motor controller. All movement requests had to be made through this specific computer, as well as all requests on motor status, such as position. With TANGO, a general device server is instanced for every motor controller. This device server controls all detailed settings related to the controller and its respective axis. It can translate simple user input into the actual motor movement command and can also be expanded to incorporate safety features or storing favorite positions. A user can then request motor movement from anywhere

within the TANGO system, and even recall information such as motor position or favorite settings. Access from multiple machines at the same time is possible as well. This greatly decreases complexity of programs incorporating several motors, and also makes them easier to service, as basic motor features are confined within the TANGO device server. If the controller itself has to be replaced with a different one, only the device server has to be reprogrammed, and not all user code using motor movement. Many devices are directly Ethernet enabled, and thus several TANGO device servers run on a single virtual machine, which improves maintainability. These benefits justify the choice of TANGO for incorporating all diagnostic controls in the future.

The mirror holders to mount the chamber mirrors have been ready for cleaning and installation by 2018. During this time an alignment strategy for the elements of the chamber was devised and tested, allowing to focus first full-aperture pilot laser light in the LION EBL. An Off-Axis-Parabolic mirror (OAP) with high optical quality allows close to diffraction limited focusing. However, first laser foci with this setup had unsatisfactory laser focus quality. After some investigation it was confirmed that the quality of the OAP was insufficient due to surface deformations degrading the wavefront. A full aperture beam size adaptive mirror in the LBD beam path, which became operational in December 2018 did not solve these problems [48]. A setup to test the focus quality of OAPs has been developed and set up to investigate this issue further. After some months of investigation it was concluded that five of the OAPs (made of copper) that were delivered had surface deformations. The most severe deformations came from mounting threads in their bulk material, that approached close to the mirrors surface. With the test setup we could confirm that tightening or loosening the screws had an impact on the focus shape. It was decided that these OAPs had to be refurbished by the manufacturer. In the first step the manufacturer refurbished the surface, and in the second revision a new holder that did not exert tension on the mirror substrate was introduced. After testing this tedious process on one OAP, this is in use now since end of 2021. This problem delayed laser-plasma experiments in LION until the delivery of a coated glass OAP with focal length f = 150 cm, 20° off-axis angle, mounted in a holder designed not to apply tension on the substrate. The first run in the test setup showed that it was performing within specifications, and was suitable for experiments.

First ATLAS pulses were sent to LION in March 2019, and after installation of the glass OAP in April 2019, a high quality ATLAS focus in the LION EBL has then been demonstrated in May 2019. With this, the last missing piece of the experiment had

been installed. The first laser-plasma experiment in CALA was performed on the 8th of May 2019 with a laser pulse energy $< 100\,\mathrm{mJ}$ on target. This did not yield any proton signal. On 26th of June the laser pulse energy could be increased to 2 J on target and the first laser-driven particles - protons - have been detected in CALA. This marked the start of the LION commissioning phase. Regular experiments, often on a weekly basis, led to identification and fixing of remaining issues of hard- and software. Based on the thorough preparations, quick progress has been made to demonstrate the same stage of extension of the setup as in LEX Photonics. Reproducible proton acceleration with kinetic energies $> 12\,\mathrm{MeV}$ allowed to use the permanent quadrupole ion beamline setup from LEX Photonics. A first proton focus was demonstrated on 28th of October 2019. With this, the setup of the LION-LEX experiment had been reproduced with significantly increased proton energy and particle number, as well as stability. Experiments continued in a reduced manner during the 2020 restrictions. A proof of principle proton radiography experiment has been carried out in October 2020 and presents a notable first milestone (see A.0.1). Protons with kinetic energies $> 15\,\mathrm{MeV}$ were available on a day to day basis, and these energies have been achieved in most shots during a beamtime. Although the proton energy distribution has remained fluctuating, the setup was stable enough for first applications of laser-driven ion bunches. Three master thesis projects have investigated parameters of laser-driven ion bunches at the LION experiment during that time. These were further contributions to the setup to prepare it for more advanced applications. One thesis designed and tested the Foil-electrode Ionization chambeR For Laser-driven Ions (FIREFLI), a very small gap ionization gas chamber for proton bunch measurements. The small gap minimizes energy loss, and thus makes it a perfect detector to be used in transmission, ideally right be fore the irradiation object [49]. The second work concerned light scattered or emitted by the laser-plasma interaction. This may yield additional information on the acceleration process and could provide a complementary, non-invasive diagnostic for the ion source. During this work, the light-based laser-plasma metrology was installed on top of the LION vacuum chamber [50]. The effect of field- and alignment errors on the proton focus shape of the permanent magnet quadrupole doublet has been investigated in a third thesis project. The required ion beam optical elements have to be pre-aligned precisely for minimizing the required shots for in-beam optimization. The acquired experience and knowledge now allows to optimize the proton focus in only a handful of shots [51].

2.2 The ATLAS Infrastructure at CALA

Zentrale Steuerung A central control system is overseeing the laser and acceleration operation in CALA. This Zentrale Steuerung (ZS) is the main control system in CALA. It consists of a programmable logic controller with sensors incorporated in the building and experimental infrastructure. Sensors are installed to monitor the status of, for example, radiation safety doors and other safety devices, target positions and the state of the laser system. A high-level interface allows direct communication and information such as operation mode is shared with the laser system. The ZS can also trigger an instant laser shutdown as a safety interlock. The LBD can communicate with the ZS as well. For example, the selected laser beam path (the positioning of mirrors) is monitored to ensure that pulses reach their designated target. Another important system is the vacuum control system, which sends information on residual gas pressures in the various vacuum sections to the ZS. The ZS oversees all subsystems and ensures defined operating conditions. High peak power experiments, for example, require closed radiation protection doors of the EBL, correct LBD mirror positions and low residual pressure in the vacuum system. Building infrastructure does also provide data for the ZS, such as temperature or humidity in the ATLAS laser hall. The ZS system can be accessed from two desktop computers in the experiment control room. The ZS operation mode and warnings, for example too high humidity or temperature, are distributed to status monitors in CALA, for example next to the EBL doors or in the ATLAS laser hall.

In order to conduct a laser-plasma experiment in LION, the experimentalist has to switch the ZS into 'Full operation CAVE' mode. The software will list all the requirements to achieve that mode. It will also send a request to move all LBD mirrors to the desired configuration. As soon as the ZS has the confirmation that all requirements are satisfied, for example the mirrors have been moved into the right positions, 'Full operation CAVE' mode is set.

Radiation shielding calculation The laser-plasma interaction accelerates particles that are energetic enough to produce significant amounts of secondary radiation when interacting with material, such as the vacuum chamber walls. Prior to obtaining an official permit to operate a particle accelerator, the dose rate in and adjacent to the particle beam had to be evaluated by simulations. These simulations showed that the EBL walls were not sufficient to restrict radiation in unsupervised areas adjacent to the cave, and an additional local beam dump was required, as already expected from

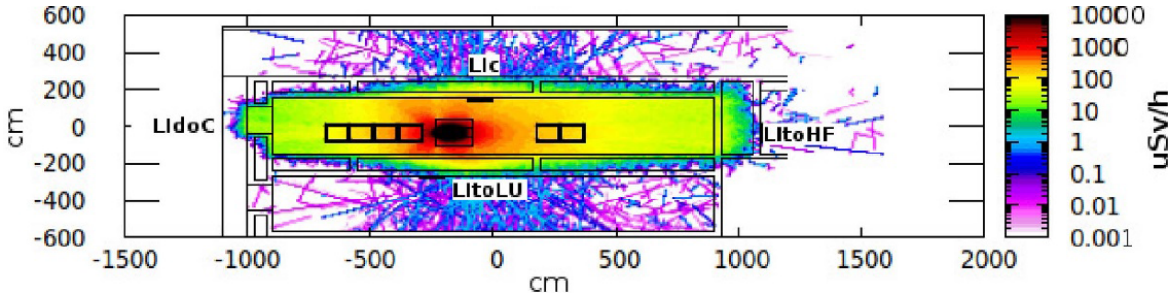

Figure 2.2: Top view of a LION EBL radiation protection simulation indicating the expected dose rate distributions in colour from an optimized ^{12}C source at -500 cm on the horizontal axis. The LION Cave extends horizontally from -1000 to +900 cm, vertically from -200 to 200 cm. Walls as well as vacuum chamber elements are schematically drawn with black lines. This distribution is a slice on target height. Additional scoring areas are positioned at critical dose rate areas and indicated with their abbreviations. The composite beamdump is located at -100 cm horizontally. Figure from [46].

the planning-phase. A thorough compilation on these simulations for CALA has been published by Englbrecht et al. [46].

Dose rates have been calculated for the case of optimized laser-driven ion acceleration, the case with the highest expected dose rates. Monte Carlo simulations have been carried out using FLUKA. The source terms for these simulations have been based on recent publications and have been extrapolated optimistically to model ion acceleration at optimal CALA parameters. Separate simulations for a proton and carbon beam have been evaluated, each including the same electron source. The distribution of the case with highest dose rates - which is optimized carbon ion acceleration - is shown in figure 2.2. Inside the LION cave dose rates ranging from 10 µSv h^{-1} to over 1000 µSv h^{-1} are reached at working areas. The radiation is contained by the walls made of a magnetite aggregate and magnetite concrete, ranging in thickness between 100 cm and 200 cm. The cave roof consists of three steel roof bar layers, also filled with magnetite aggregate [52].

Areas where the expected dose is lower than 6 mSv/a do not require laboratory personnel to be equipped with dosimeters. This equals an average dose rate of 3 µSv h^{-1} over the expected operating time of 2000 h per year. Since access to the LION cave is prohibited during accelerator operation, and the dose rates outside of the cave are below the self-set limit of 2.5 µSv h^{-1}, personal dosimeters are not necessary in CALA.

Even though the cave walls are good radiation shields, the accelerated ions require special treatment and are sent towards a beamdump, where a majority of radiation

can be contained. As they hit the beamdump, the primary (ion) radiation is converted to secondary radiation (e.g. photons or neutrons). Initial dose-rate simulations by Nuclear Technologies suggested an iron beamdump weighing 28 t at 60 cm distance from the ion source. With this design, they could achieve dose rates lower than the dosimeter threshold. This design would have been impractical though. The close distance to the ion source would have made many application experiments impossible, and motivated a redesign. G. Dedes and F. Englbrecht have first reproduced the NT data in-house successfully, and provided additional simulations where a novel beamdump design could be investigated.

This improved beamdump is a water - concrete hybrid. A cubic box with 49 cm width made of Plexiglas and filled with ultra clean water is surrounded by reworked concrete blocks from the previous setup at LEX Photonics. The total weight of this design is 12 t. Simulations confirmed that this design was effectively containing radiation (keeping radiation outside LION below 2.5 µSv h^{-1}), even placed at a distance of 2.3 m from the source. This enabled a 50 cm gap between the LION vacuum chamber and the beamdump, which allows for on-air irradiation experiments.

ATLAS is a Chirped Pulse Amplification (CPA) system that has been operated since late 1990s and dubbed Advanced Titanium:Saphire LAser System. It is meanwhile operated in the ATLAS 3000 hall (see figure 2.3). We will review the main improvements that were made during the last upgrade phase to enable laser-ion acceleration experiments in LION. Figure 2.4 shows the most important components in this context.

Figure 2.3: ATLAS 3000 hall during the commissioning phase in 2020. The first stages ('front-end') are seen in the left picture. The right picture shows the components and size of the final two amplifiers, which are covered by red lids.

The spectrum of ATLAS pulses ranges from $\lambda_L = 750$ nm to 850 nm. It can pro-

duce pulses as short as $\tau_L = 20\,\text{fs}$ FWHM duration, though during the commissioning phase a typical pulse length has been $\tau_L = 32\,\text{fs}$ (12th of May 2021). The system is designed to deliver up to $E_L = 60\,\text{J}$ after compression in a single pulse. The peak performance values promise to reach $P_0 = 3\,\text{PW}$ peak power, but the pulse energies during commissioning remained below 10 J on target. The final beam diameter of ATLAS is $d_L = 28\,\text{cm}$.

Intense light can also travel 'up-stream', thus the opposite direction, from the laser-plasma experiment towards the oscillator. These photons are created or scattered back during the laser-plasma interaction, and are re-collimated by the final focusing optics. As they travel further up-stream, they pass through the final laser-amplifier crystals. The amplifier crystals may still have some remaining pump energy stored in form of inversion, so that up-stream photons can be multiplied. The back-ward propagating pulse can thus be amplified, and finally damage components inside the laser. Therefore these pulses, or 'backreflected light', have to be suppressed. In ATLAS a Large Pockels Cell (LPC) for a 6 cm diameter beam has been installed for this purpose, as well as two photo-diodes that measure the amount of backreflected light. A passive protection (Faraday isolator) has been installed as well. We shall now follow an ATLAS seed pulse

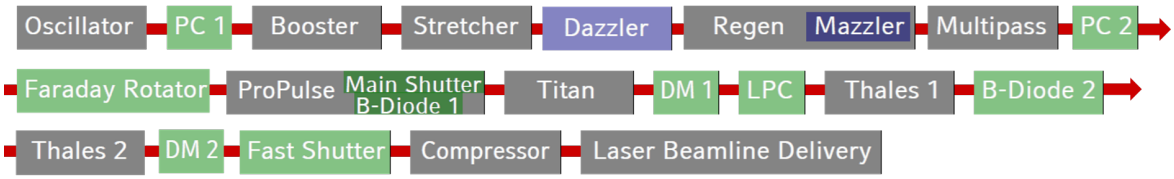

Figure 2.4: ATLAS 3000 schematic. Laser pulses are generated by the Oscillator in the top left. The red line is indicating the path of the seed pulses, which is travelling towards the Laser-Beamline-Delivery.

through the amplification chain, as shown in figure 2.4.

The actively mode locked oscillator generates fs-short pulses with 80 MHz repetition rate and a pulse energy of nJ. A Pockels cell is then picking pulses with 10 Hz. These are sent in to a multi-pass amplifier called 'Booster', the first amplification stage. The following grating stretcher increases the pulse length to 1 ns. The following 'Dazzler' [53], an acousto-optic programmable dispersive filter, allows to introduce a desired group delay for each spectral component of the pulse. It can pre-compensate dispersion that is produced before or after this element in the laser chain, allowing to nearly perfectly re-compress the pulses after amplification. The next amplifier stage is a regenerative amplifier, referred to as 'Regen'. Its purpose is to smoothen energy

fluctuations from the prior stages, and to shape the spectrum with a 'Mazzler' [54]. This device is an acousto-optic programmable gain filter. The following multi-pass stage is called 'Regen multi-pass'.

The next element is a pulse-picker Pockels cell (PC2). It has a very fast rise-time $< 1\,\mathrm{ns}$, and operates at 1 Hz repetition rate. The fast rise-time is critical to reduce the duration of the ns-long Amplified Spontaneous Emission (ASE) preceding the seed pulse. Prior to an experiment, the timing of this Pockels cell is adjusted in 100 ps steps to move the rising edge as close to the pulse as possible.

After that, the pulse passes through a Faraday isolator, which is acting like an optical diode. Pulses traveling down-stream can pass, up-stream pulses are deflected out of the beam path. The following multi-pass amplifier 'Propulse' amplifies up to 300 mJ. Within this stage, the 'main shutter' is installed. It is a small motorized plate that can either block the laser-seed path, or allow pulses to pass. After the following 'Titan' multi-pass amplifier, pulses contain up to 1 J of energy. A deformable mirror (DM1) is correcting for potential wavefront errors, before the pulse is sent to the final two large multi-pass amplifiers 'Thales 1' and 'Thales 2', which allow pulses to be amplified up to 90 J. For commissioning, we mostly operated at reduced pumping power yielding around 20 J. The following adaptive mirror (DM2) is compensating wave-front errors.

The pulses then enter a vacuum chamber and after the final telescope and spatial filter are re-compressed in time by a grating compressor.

After compression, the beam can be coupled out of the vacuum towards a diagnostics setup. A third order auto-correlator 'Tundra' [55] allows to scan laser contrast on a 2 ns delay range with typically 11 orders of magnitude dynamic contrast (Figure 3.1 shows an example trace). A frequency-resolved-optical-gating (FROG [56]) device estimates the exact pulse duration. A 'Wizzler' [57] can also estimate the group-delay of the pulse spectral components. This information is then used for a feed-back loop to the Dazzler (at the stretcher). This loop allows to optimize for the shortest laser pulse duration. More details on ATLAS are available at [58].

For alignment purposes and as a pilot beam, a diode laser can be coupled into the beampath after 'Thales 1'. A switchable beam expander enables operation of two beam sizes in the LBD, 3 cm or full aperture 28 cm diameter beam.

Laser-beam-delivery LBD The Laser-Beamline Delivery (LBD) connects the laser (currently ATLAS 3000) with five EBL. The complete system is below ground level.

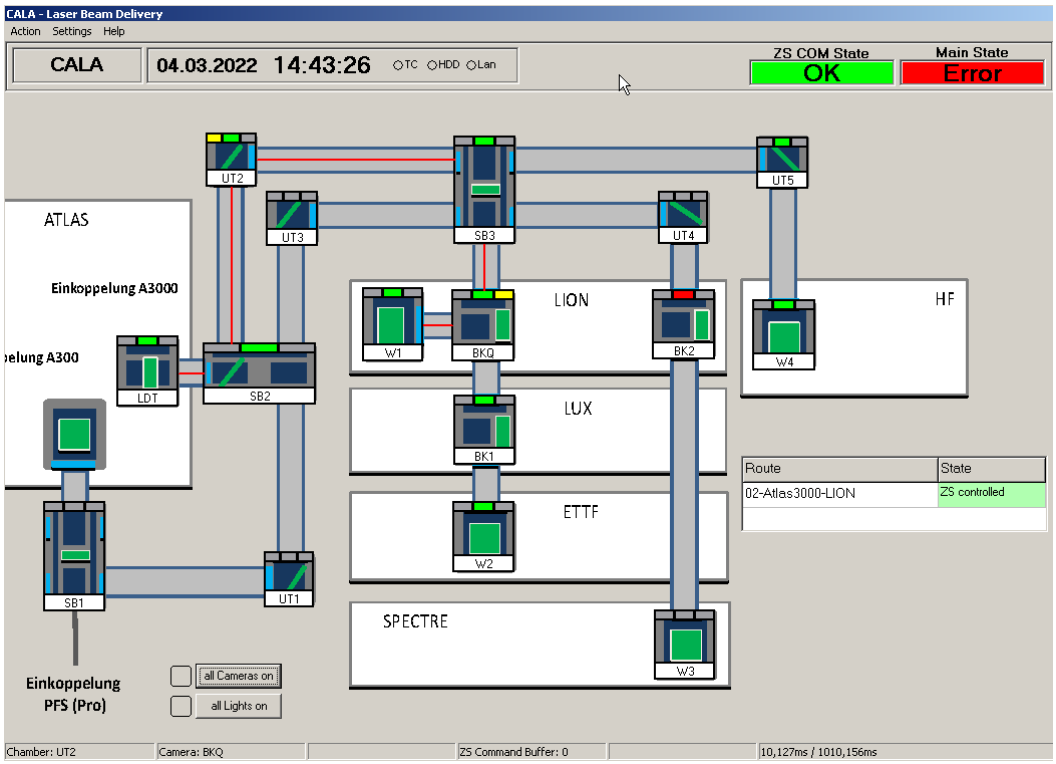

Figure 2.5: Screenshot of the LBD control software showing a map of the LBD vacuum boxes and their respective names. A route from ATLAS 3000 towards LION has been selected incorporating DM3 in the box UT2. Laser pulses will be sent along the red line. This is the setup used during the experiments.

The building floor is 100 cm below the false floor height. Thus, the laser beam passes a periscope at the entrance and exit of the LBD. The complete LBD system is on vacuum and consists of 16 vacuum chambers connected by tubes with 32 cm aperture. Each vacuum chamber contains a motorized mirror-holder that can be remotely controlled by the LBD control software (screenshot of the user-interface in figure 2.5). Each mirror holder can adjust its tip and tilt. Switch boxes (labeled SB) have an additional 'move' axis. It can move the holder out of the beam path completely, or for parallel tubes, into the adjacent tube.

Each mirror holder contains a 30 x 42 x 8 cm^3 mirror substrate. On the side facing the laser beam, they have a high reflectivity (HR) coating for the ATLAS spectral range, which is specified to a minimal reflectivity $R_{min} \geq 99\%$ at the extremes of the reflection band [740 - 860 nm] for an incidence angle of 45°. Reflecting a laser beam over six such mirrors already has a total reflectivity - or 'transmission' - of 94%. The pulses propagating parallel to the ground through the LBD are s-polarized, on the lower periscope mirrors the beam is p-polarized with respect to the mirror

surface. Reflectivity has been measured for each mirror in both polarizations and their installation point has been selected to allow for maximum transmission through the LBD for all EBL.

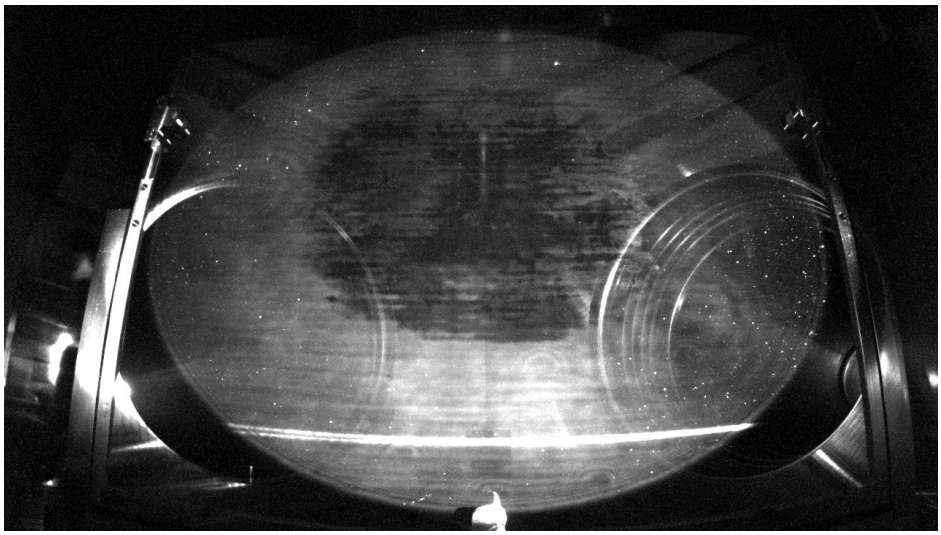

Figure 2.6: SB2 camera image illuminated with a full aperture beam. AMP1 and AMP2 have been turned off for capturing this picture. The large illuminated ellipsoid in the center is laser light scattered off the reflective mirror surface. Left and right of it the mirror holder is slightly illuminated. The dark spot in the center of the laser beam is an indication of a decreased reflection performance, likely due to carbon contaminants.

Vacuum compatible cameras are installed to monitor each mirror in the LBD. This is required to confirm the position of the laser beam during alignment. Additionally, it can give information on the beam fluence distribution and potential problems or clips. An example image is shown in figure 2.6. In this image, the bright ellipsoid beam is visible. The darkened spot in the beam center is indicating degradation of the HR-coating, which results in reduced transmission through the LBD.

A deformable mirror (DM3) is installed in LBD chamber 'UT2'. This allows wavefront correction introduced by the compressor gratings and LBD mirrors, hence optimizing the final focus.

Upon selecting an experiment route in the ZS, the LBD will adjust the mirror-move axis accordingly such that laser pulses from ATLAS arrive at the desired EBL. The route from ATLAS to LION incorporates six mirrors.

2.3 LION

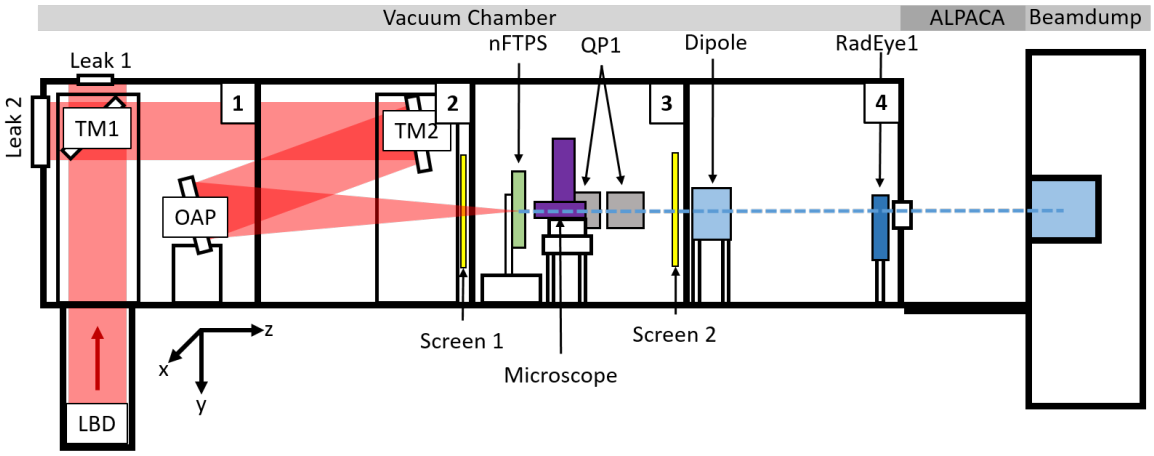

Figure 2.7: Schematic of the LION setup in side view. It consists of three major parts, the vacuum chamber, the application platform, and the beamdump. Laser pulses, red color, enter the chamber from the LBD. The laser focal spot is in the target plane of the nano-Foil Target Positioning System (nFTPS). There, the laser-plasma interaction accelerates particles. Accelerated ions, blue color, propagate in positive z direction along the dashed line. A 50 x 50 cm breadboard adjacent to the chamber rear allows to position experiments that use the accelerated proton bunch. It has been named 'A Laser-driven Proton-ACcelerator Applications-platform' (ALPACA).

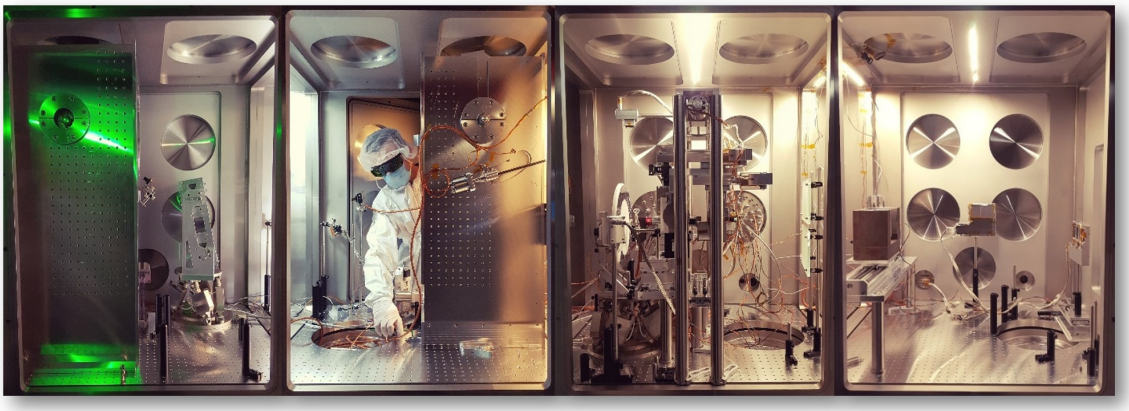

Figure 2.8: LION EBL vacuum chamber interior at the end of 2020, same perspective as figure 2.7. Onset of rapid cable growth is visible. Picture by M. Speicher and including L. Doyle.

The LION EBL is designed to deliver protons with kinetic energies up to 100 MeV, and carbon ions with kinetic energies up to 400 MeV/u for applications.

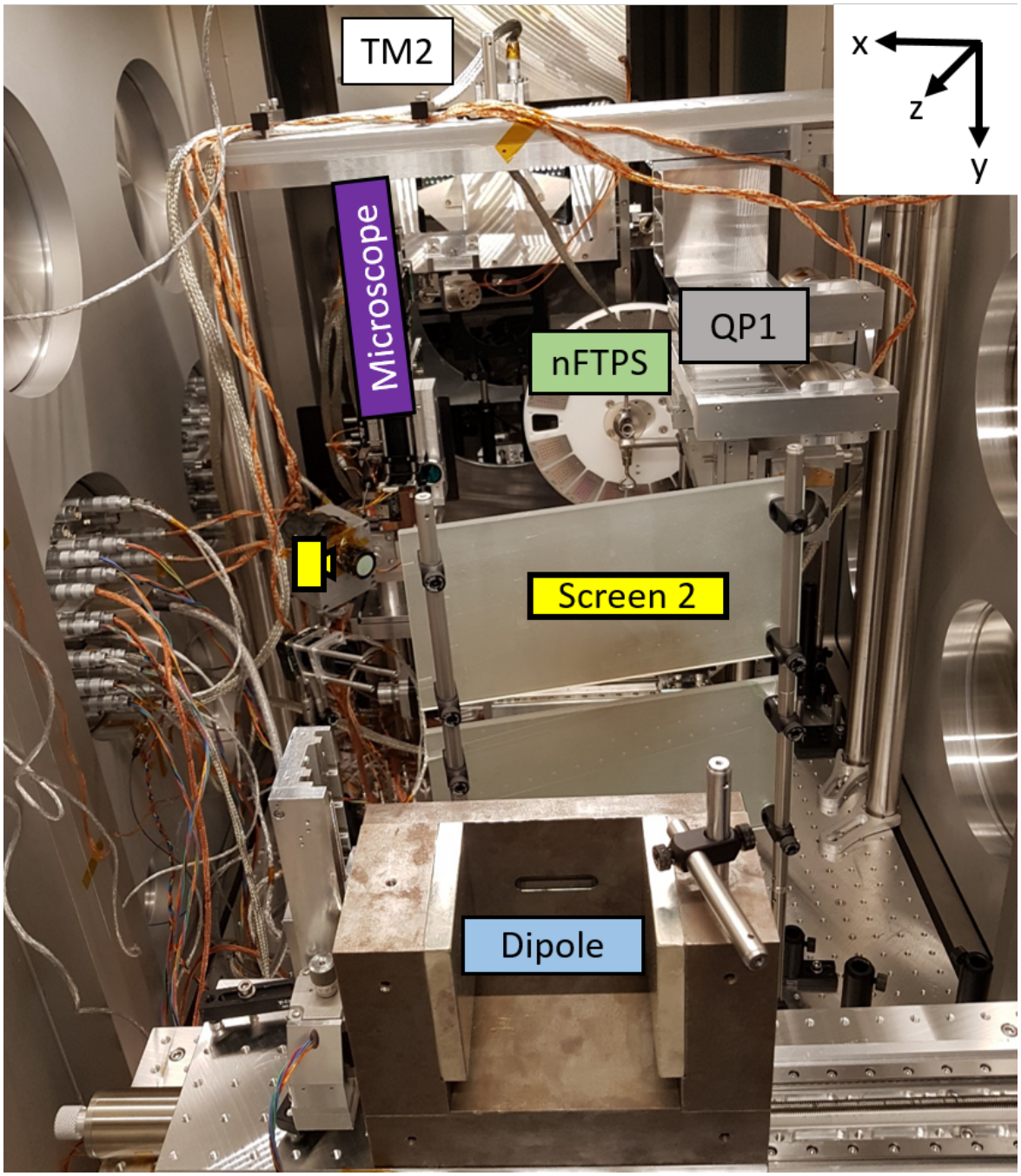

Figure 2.9: LION interior, view from chamber 4 to 3.

We explain the components of the laser-plasma experiment setup and all diagnostics relevant for this thesis. The schematic in figure 2.7, and the picture in figure 2.8 represent the setup from late 2019 to mid 2021. We will refer to experimental components with the annotations of the schematic. First, we follow laser propagation towards the laser-plasma interaction. We will explain the determination of the laser

fluence distribution and related peak intensity, the recording of scattered/transmitted light, the target positioning system and the magnetic deflection and detection of ions.

Laser propagation Laser pulses from the LBD enter the LION vacuum chamber through the periscope between the last LBD mirror (W1) and first LION turning-mirror (TM1). TM1 incorporates a special dielectric coating, allowing 1% of the incident light to transmit. This light then passes through 'Leak 1'. It is sent to the 'incoming light' diagnostic, where the incident laser pulse energy as well as focus quality and spectrum can be recorded. An example use is a diagnostic that records the focus position drift at this port [59]. Note that 'Leak 1' has an aperture of 12 cm, thus does not allow to sample the complete beam. Light recollimated from the laser-plasma interaction is sent through the 'backscatter' diagnostic positioned at 'Leak 2'. This window is large enough to allow the full aperture 28 cm beam to pass through, however, the mirror holder of TM1 clips a few cm of the beam. At the backscatter diagnostic, a spectrometer is set up as well as an equivalent-plane-monitor [50].

The second turning-mirror (TM2) is silver coated. It is designed to have high-reflectivity for the two planned OAP angles. First, an angle of 45° - to be used to reflect the beam on to a 90° OAP - or second 10° - for a 20° OAP. To accommodate this, it has a longer tilt axis then TM1.

As explained in section 2.1, a glass OAP has provided the best focus. This OAP has a focal length of $f_L = 1.5\,\mathrm{m}$, and an off-axis angle of 20° and reflects and focuses the beam to focal spot sizes approaching the resolution limit. The focal spot position in the target chamber is referred to as Target-Chamber-Center (TCC).

Vacuum microscope The focal spot is measured by recording a fluence distribution of the attenuated laser beam with a vacuum compatible microscope [60]. It is mounted on a motorized stage and can be moved, either allowing it to monitor TCC or be retracted towards the vacuum chamber wall, out of the laser beam or ion-bunch path. Light from TCC is collimated by a microscope objective, and distributed via beamsplitters to four vacuum-compatible cameras. The attenuator reduces the laser pulse energy by eight orders of magnitude and is inserted into the beam path prior compression. Additional filters inside the microscope reduce the pulse energy by another six orders of magnitude.

The microscope is mounted on three motorized stages. 50 cm travel along the x-axis allow to move the microscope far away from the laser-plasma interaction during the experiment. A rotational stage adjusts the viewing angle in the horizontal x-

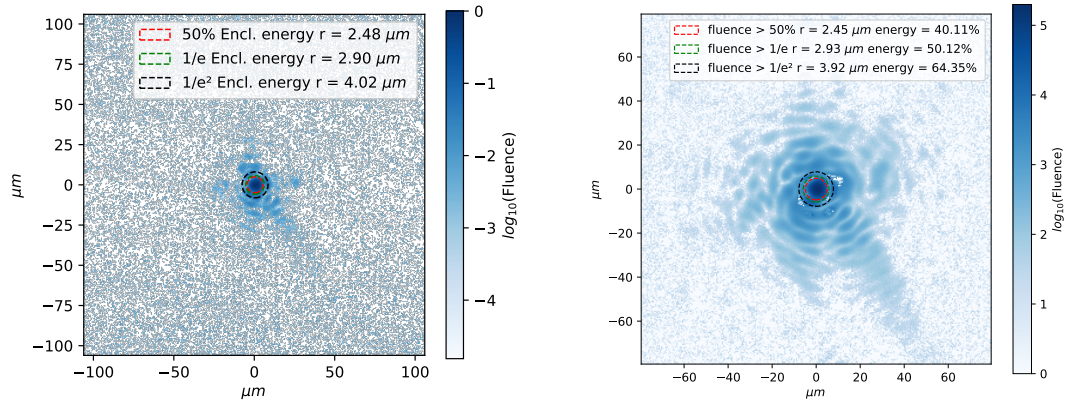

Figure 2.10: LION EBL laser-focus images. Single-shot low-dynamic range laser fluence on the left, high-dynamic range laser fluence on the right. Both recorded on the 12th of May 2021.

z plane. The light has to enter perpendicular to the microscope objective's front surface to reduce imaging aberration, which must be confirmed regularly. To allow the microscope to inspect the laser beam, currently incident at 6.8° with respect to the chamber z-axis, and targets, which are at 0° with respect to the chamber z-axis, the microscope incorporates a rotational stage. As this rotation is off-center, two additional stages compensate for the shift in x- and z-direction during rotation. Parallel to the microscope objective, a white-light distance sensor is mounted, which works on the basis of a chromatic confocal setup. The sensor has a working range of 10 mm and a sub-µm accuracy. It is used for automated target alignment.

The microscope is equipped with a Mitutoyo APO NIR 20x objective [61] with a long working distance of 20 mm. It collimates the light from the focal plane. Directly behind the objective mount, the incident light is split by a beamsplitter. The horizontal path uses a short 3 cm focal length tube lens to re-image the focus to realize a 1.3 times magnification (Low-Mag). It features a larger field of view, which is helpful for focus and target alignment. The other beampath is then split again by a beamsplitter. One arm is sent to the High-Mag camera, which features a 20 cm focal length tube lens to achieve the designed 20 x magnification of the objective. The focus images of figure **??** have been recorded with this camera, and it is also used for target plane fine alignment. By definition, the plane that is focused on this camera, is the TCC plane where the laser focus is overlapped with the target. The second beampath in this arm is used to illuminate the target surface by an infrared LED. The last arm hosts a telescope to image a plane in close vicinity to DM3, the deformable mirror in the LBD. The

resulting near-field is split again onto one camera imaging the near-field. Clips in the beamline and artifacts from incorrectly illuminating the OAP can be identified with this camera. The replica is sent through a micro-lens array, and then onto the Wavefront-Sensor camera. A tilted wavefront will shift the foci of the micro-lenses. By comparing their shifts to a reference image, obtained with a 2 µm pinhole in focus, the wavefront shift can be calculated. This is fed back and driving adjustments on DM3 in the LBD, enabling the adaptive optics loop. Thus, in this setup, DM3 can optimize the focus of the experiment, though only with strongly attenuated pulses and filters inserted [48].

The laser focus fluence has been evaluated from images recorded with the high-dynamic-range stacking technique: The cameras of the microscope have a dynamic range of 10-bit. The beam is filtered such that it exploits this dynamic range of the camera, and the resulting image is saved (Low-Dynamic-Range LDR, example in figure 2.10 a). By consecutively recording a series of images with decreasing filter strength, an increasing number of pixels will saturate. Light that has not been detected in the first picture (at the edges of the focus distribution of the first picture) will become visible. A program stacks these images by replacing saturated pixels with unsaturated ones from a recording with more filters, and the result is shown in figure 2.10 b). During this process, the filter ratio between the acquisitions is considered. This extends the dynamic range in our case by two orders of magnitude [38].

For the LDR image, the focal spot is confined to the center, and noise is visible. The HDR image shows a much larger distribution of laser light, despite some artifacts from the stacking process. The intensity distribution of the collimated beam in the LBD and on the OAP is approximately flat-top. As such, the focus images show centered circular ripples. These are expected, as the beam profile on the LBD mirrors approximates a flat-top distribution. We have calculated the peak intensity from this image to be $1.07 \cdot 10^{21} \mathrm{W\,cm^{-2}}$ (see C).

nano-Foil-Target-Positioning-System The target system is responsible to provide and replace the targets for each laser shot during the experiment. The system ideally is easy to use for the experimentalist and thus has a high degree of automation. Additionally, target-replacement at the same speed as laser pulse repetition rate is desirable. The nano-Foil-Target-Positioning-System (nFTPS) consists of a wheel with 19 windows for target holders. One target holder is a 500 µm thick steel plate with 40 holes in an area of 1.7 x 2.8 $\mathrm{cm^2}$, over which the target foil has been attached.

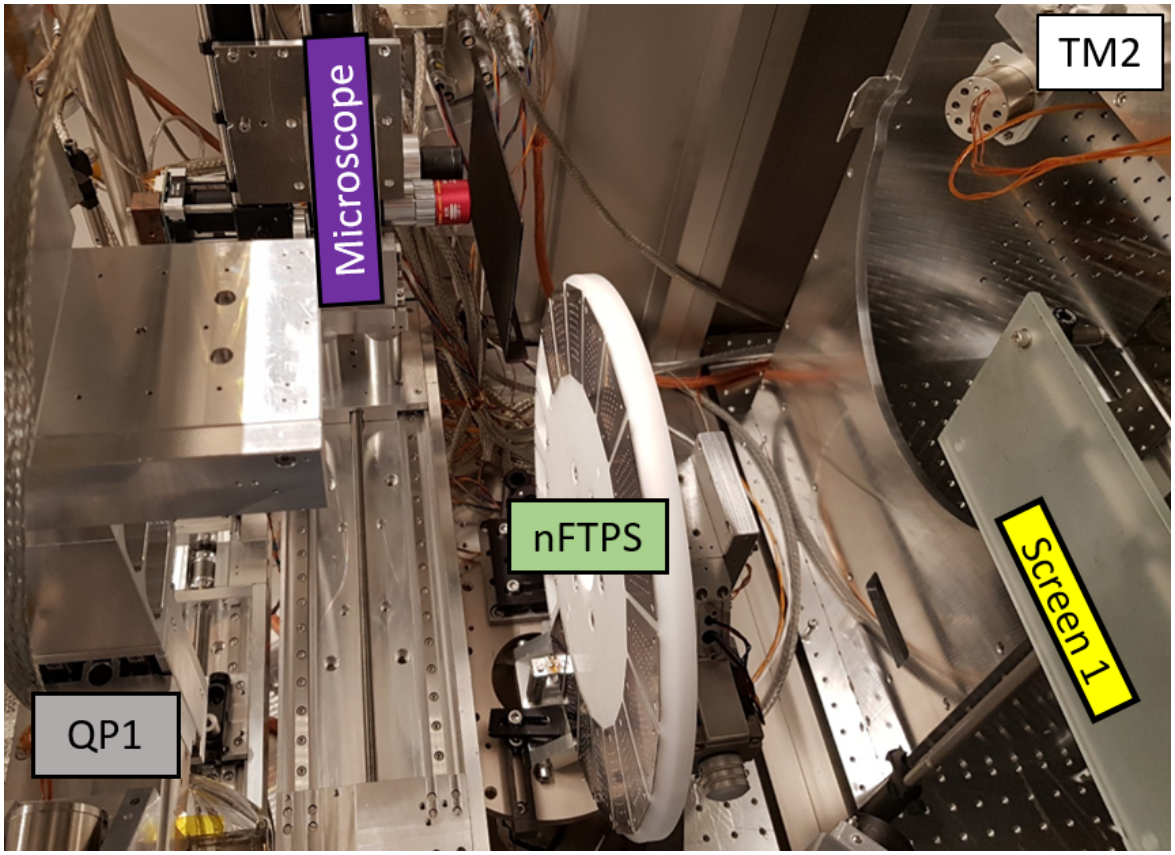

Figure 2.11: Side view of the target system. The microscope assembly is on the left. The white target wheel is on the right side.

This allows a variety of foil-target materials to be used, such as aluminum, gold and plastic foils with thicknesses from tens of nm to few µm. The wheel can easily be extracted and re-mounted, and target holders are replaced on the workbench. The previous version of this system has successfully been used in LEX-LION [35]. Since then, its hardware and software have been improved.

To achieve the highest intensity in the interaction, the target has to be positioned along the z-axis with an accuracy much smaller than the Rayleigh length, in which the intensity decreases by a factor of two. In case of the obtained focus from the 1.5 m focal length OAP, the Rayleigh length is 60 µm, which is significantly larger then the nFTPS accuracy of 5 µm.

In the revised design used in this thesis the heavy aluminum wheel was replaced by a lightweight non-conductive plastic (Polyoxymethylen) to reduce weight on the mechanics and decrease EMP generation from the assembly. Figure 2.11 shows a picture taken in the LION EBL. The target hole diameter has been increased from 0.5 to

1.5 mm. The mounting process was changed to an easier accessible magnetic clip-on for each target holder. The plastic wheel with the magnetic mounts has significantly higher mounting tolerances compared to the previous version, which had to be compensated by a new routine allowing for a much larger spatial fine correction than in the first version.

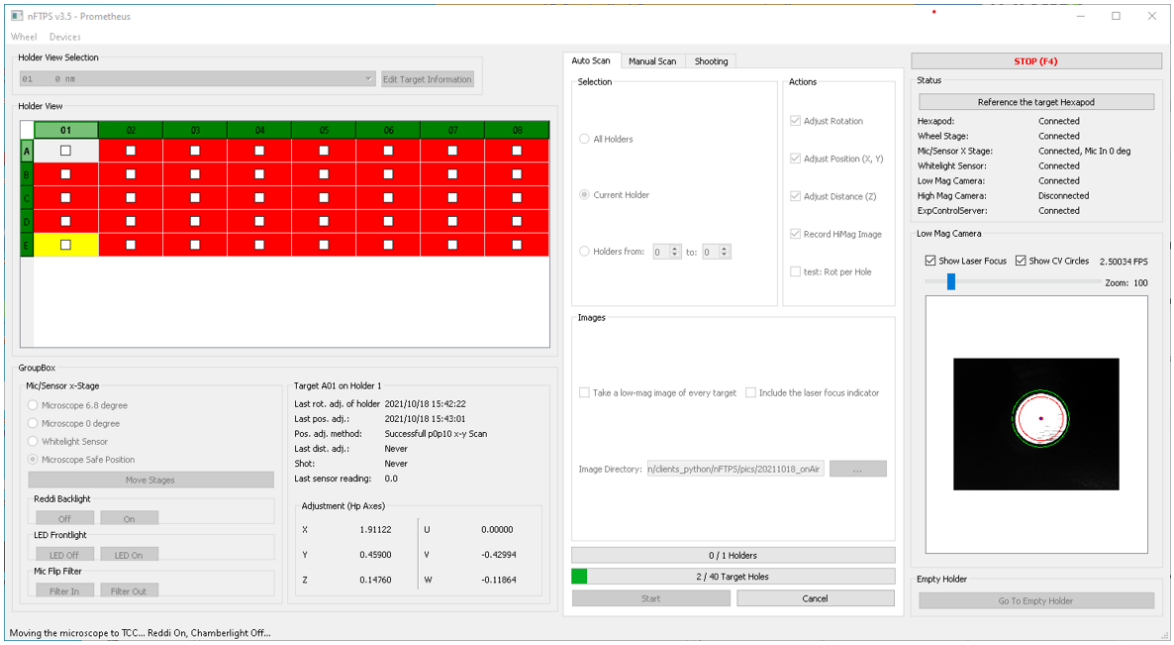

Figure 2.12: Screenshot of the advanced nFTPS control software. In the upper left a schematic of a target holder gives visual feedback on the state of each hole and allows target selection. Below are the microscope positions and filtering as well as object illumination controls. The center section of the program allows to switch between automated scan, manual scan and the shooting operation mode. The right side provides information on the current motor stage status. A preview window provides a live-feed of the Low-Mag during the scanning routine, and switches to a preview of scanned targets upon switching into shooting mode.

Over the course of this thesis, the nFTPS control software has been re-coded in python. A screenshot of the user interface can be seen in figure 2.12. This software was designed around the new TANGO based interfaces, such as the motor control device servers. Additionally, the grade of automation could be increased with a novel completely automated search mode: The rotation of the target-wheel will be referenced first, which has to be done after target holders have been replaced on the workbench and the wheel is re-mounted. Then, the following routine is repeated for each target holder separately. The position corrections obtained by previous steps are always used in the next steps. Target holder tip/tilt is adjusted by scanning with the white-light

sensor the distance of two points 2 cm apart for the x- and y-dimensions, allowing to calculate the required compensation angles for each dimension. After correcting these with the six-axis hexapod the target holder is perpendicular to the microscope objective. Then, the target holder is moved into the TCC x-y-plane by measuring the distance at the target holder center, and compensating accordingly. Second, a back-illumination laser is switched on and three targets at the edges of the target holder are monitored with the low-magnification microscope camera. The center of brightness of the respective target image is calculated and used to estimate the required correction in the x-y-plane by the hexapod. Each correction step is only driving 90 % of the calculated offset, and the routine repeated until the positioning criterium, currently 40 µm, is achieved. As the target holder is a solid structure with a defined geometry, this alignment is good enough to derive the x-y-offset corrections for all remaining targets on this holder. Third, the white-light sensor records and compensates twice the distance for each hole, as this is the most critical alignment along the z-axis. Fourth and last, a picture is recorded by the low-mag camera for every hole using the illumination LED installed in the microscope. Thin transparent plastic foils will reflect much less than gold foils for example. These images are highly useful to determine the foil quality during and after the experiment for each shot. Excluding significantly damaged foils has been beneficial to reduce shots with high laser-light transmission and made the ion-bunch acceleration more robust. The presented routine scans without manual corrections all 19 target holders with 40 holes each, 760 targets in total, within 4 hours.

Laser-plasma scatter diagnostic A 20 cm by 20 cm sanded glass screen (Screen 2) at a distance of 90 cm from TCC is positioned such that the full near-field of the laser pulse transmitted through TCC is collected. The camera has been set up in an EMP safe housing. Scattered light passes three filters by Thorlabs, which are, in the order of the incident light: FELH0700, NE40A-B, NE10A-B. This setting ensures good illumination without saturation from an empty shot from a laser pulse with 3.5 J in the chamber and provides the reference for calculating the transmission through the target in a real shot. A typical image obtained from the camera monitoring this screen, also referred to as transmission screen, is shown in figure 2.13. A similar diagnostic has been set up in reverse direction (Screen 1). This is referred to as backscatter screen.

Permanent-quadrupole (PMQ) doublet Permanent quadrupole lenses can be inserted to transport the ions from the target to the application platform (QP1 in

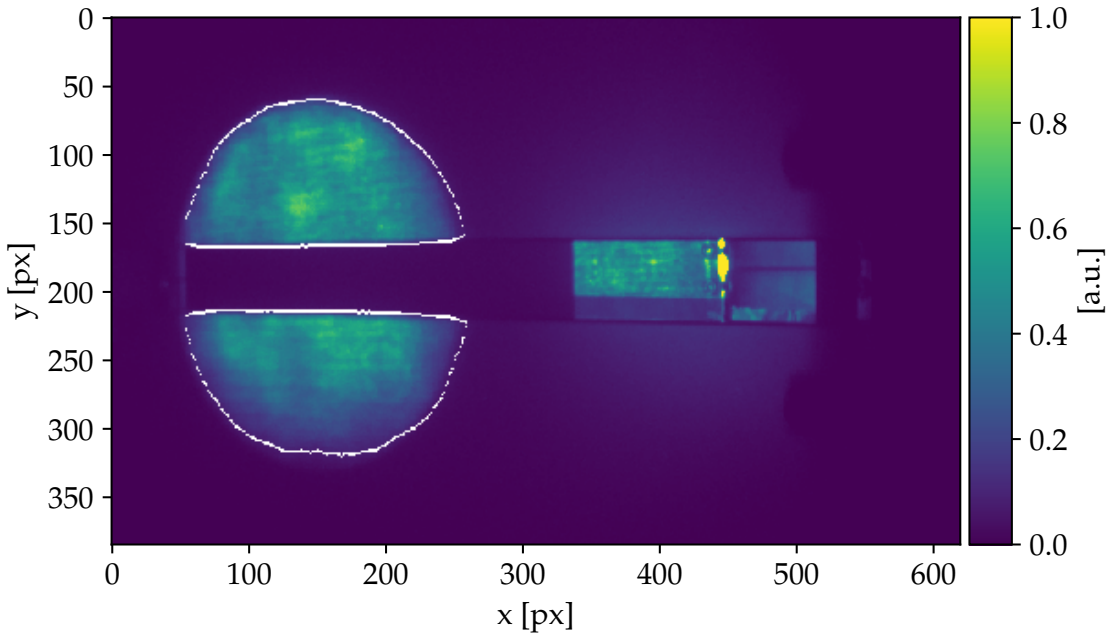

Figure 2.13: Image obtained by the camera monitoring transmission from an empty shot with an energy low enough that it does not saturate any of the pixels. The screen is divided into two parts spaced about 2 cm apart allowing the accelerated ions to pass through. Most of the light is hitting the screen in the left part of the image, but some is transmitted through the slit and reflected by the magnet in the right half. The evaluated area is enclosed by a white line.

figure 2.7). Details of this setup and its performance have been described by Rösch [27] [62].

Chapter 3

Physical Backgrounds and Theoretical Framework

The following chapter will give the physicals context for this thesis work. Laser-driven ion acceleration theory will be explained in appropriate depth of this work. Theoretical calculations of the dispersion of proton bunches with broad energy spread by inhomogeneous magnetic dipole fields is explained in detail as well as the basis for the new Quantitative Ion Spectrometry (QIS). The basic process of energy deposition in silicon detectors and their read-out are described. It is estimated how much energy a particle deposits in the active layer of the detector and with which probability. This understanding is essential for interpreting the raw signal histograms, which are generated from two dimensional signal distributions of the pixelated detector. Finally, the statistical model for QIS is explained. Its validity and performance is demonstrated on the basis of simulated histograms.

3.1 Laser-driven Ion Acceleration

Currently available laser intensities are well beyond 10^{18} $\mathrm{W\,cm^{-2}}$, the relativistic threshold of optical radiation. The current work was performed with laser pulse energies between 0.1 and 9.9 J on target, and pulse durations of 32 fs focussed up to intensities of $I_L = 1.07 \cdot 10^{21}$ $\mathrm{W\,cm^{-2}}$ (calculation see C). Thin formvar foils with thicknesses between 20 and 600 nm were irradiated. Consequently, this section gives a crude overview of most relevant knowledge on laser-ion acceleration in this intensity and target thickness regime. For a complete study of this topic, it is recommended to consult Gibbon [63].

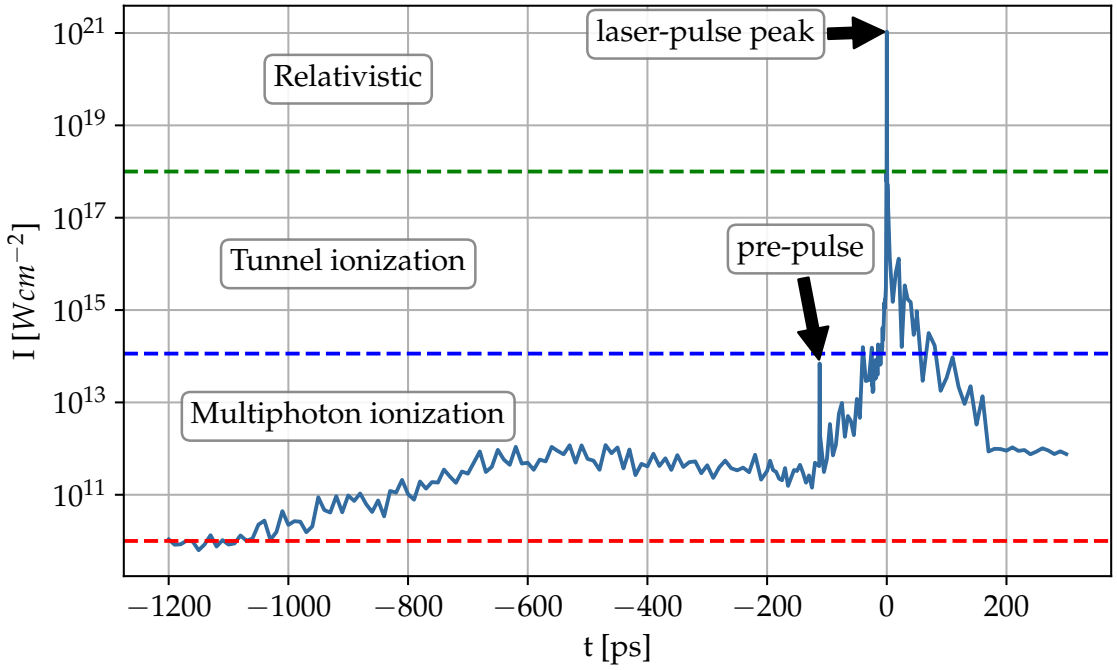

Figure 3.1: ATLAS temporal intensity ('temporal contrast') scaled to $I_L = 1.07 \cdot 10^{21}$ W cm^{-2}. Multiphoton ionization (MPI) sets in at $I_L > 10^{10}$ W cm^{-2}, tunnel ionization at $I_L > 10^{14}$ W cm^{-2}. Electrons become relativistic at $I_L > 10^{18}$ W cm^{-2}.

Consider for the sake of the argument the electron in the ground state of a hydrogen atom. The electron is bound to the proton by an electric field of approximately 0.5 TV m^{-1}. An incident laser pulse provides an electromagnetic field that is superimposed to the atomic field. At laser intensities $I_a > 3.5 \times 10^{16}$ W cm^{-2} the laser field strength is higher then the field of the bound hydrogen electron. A laser peak intensity of $I_L = 1.1 \cdot 10^{21}$ W cm^{-2} (to which the auto correlation trace of the ATLAS pulse in figure 3.1 was scaled) has a field strength of 89.8 TV m^{-1}, which dramatically exceeds the intra-atomic field. The laser field will cause atomic electrons to leave their binding potential and result in ionization of the atom. This is a strongly simplified picture and often referred to as barrier suppression ionization. It is sufficient to understand that with the intensities at play, the laser will interact with a plasma, and in particular with the electrons. Unless one is interested in understanding the ionization dynamics in detail (which can be important for estimating the expansion of the plasma due to pre-pulses), it is sufficient for our purposes.

Acceleration

A typical ATLAS 3000 laser pulse used for laser-driven ion acceleration has a temporal full-width-half-maximum (FWHM) of 25 to 32 fs, but is far from perfectly Gaussian. A typical temporal evolution of a laser pulse over 2 ns is recorded by high dynamic range (third order) auto-correlation, as exemplary is shown in figure 3.1. Imperfections in the generation of such pulses lead to a ns-long pre-pedestal and a ps-long steep increase just before the peak intensity is reached at $t = 0$. Sometimes a copy of the main pulse can appear ps before the laser pulse peak is reached. This is called a pre-pulse, one is visible in our measurement at t = -112 ps. In our case the pedestal has an intensity of 10^{12} W cm^{-2}, which is already sufficient for triggering substantial multiphoton ionization (MPI) events [64].

The short pre-pulse has an intensity of $7 \cdot 10^{13}$ W cm^{-2} and is sufficiently intense for tunneling ionization or even barrier suppression [65], both processes that ionize the target ps before the laser pulse peak interacts with the target. 10s of ps before the laser pulse reaches its maximum, the intensity rises above ionization levels. Target foils with thicknesses ranging from few nano- to micro-meters, are hence transformed into a plasma long before the laser pulse peak and the generated plasma will expand, either due to fs pre-pulses [66], due to the ns-long pedestal [67] or due to the latest rising edge, typically due to a combination of all. In experiments it is ensured that the plasma remains dense enough for ion acceleration by choosing appropriate minimal target thickness, or employing methods for pre-pulse suppression, such as plasma-mirrors [68] [69] or second harmonic generation [70].

Laser-plasma interaction We must now understand how the plasma can absorb incident laser light. This absorption is important, as it determines the energy transfer from the electromagnetic wave to electrons. For this, we have to consider the effect of the electron density n_e on laser pulse propagation in the plasma. The laser wavelength shall be λ, speed of light in vacuum c. Laser propagation in the plasma is possible as long as λ is larger than the plasma wavelength. From this condition we derive the critical electron density $n_c = (\pi\gamma m_e c^2)/(\lambda^2 e^2)$, with e the elementary charge, $\gamma = 1/\sqrt{1-(v_{el}/c)^2}$ with v_{el} electron velocity and m_e electron mass [71]. The majority of laser ion acceleration is performed with over-critical ($n_e > n_c$) or (relativistically) near-critical ($n_e \approx n_c$) electron density, because there the absorption into electrons is very high [72].

At low intensity $10^{12} - 10^{17}$ W cm^{-2}, the absorption is dominated by inverse

bremsstrahlung, where incident photons are absorbed by free electrons or resonant absorption. In the latter an electromagnetic wave obliquely incident on a plasma, polarized in the plane of incidence, is absorbed resonantly into an electron plasma wave [73]. At higher intensities and very sharp gradients vacuum heating or Brunel absorption is important. In this process, electrons are dragged out of the plasma into the vacuum by the laser field, upon which they are accelerated and pushed back into the overdense plasma [74]. Gentle gradients lead to effective $j \times B$ heating where the oscillatory component of the laser-light pressure becomes important [75]. Via these processes a substantial fraction of laser pulse energy is absorbed into electrons, which move ballistically or even collectively, but are not driven by the laser fields. These electrons are called 'thermal' or 'hot'.

On the other hand, one can recall that motion of a single electron is governed by the Lorentz force $\overrightarrow{F_L} = e \cdot (\vec{E} + \vec{v} \times \vec{B})$. For light intensities $> 1.037 \cdot 10^{18}$ $[\mu m/\lambda_L]^2$ $W\,cm^{-2}$ a significant number of electrons is accelerated to relativistic speeds within a few laser cycles [76]. Then, $\left|\vec{v} \times \vec{B}\right| > \left|\vec{E}\right|$, and the electrons are primarily pushed forward along laser propagation direction. Let us consider that the laser can act on a bunch of electrons in the same way. The much more inert ions hardly respond and charge-separation fields are forming between displaced electrons and the ions. These ions provide a counter force to the light pressure $(\vec{v} \times \vec{B})$ and in turn are accelerated. This later process is the basic idea of light-sail acceleration, where electrons are the 'sail' and ions the 'freight' [77]. Keep in mind that there are two populations of electrons, which are not easily distinguishable. One is the 'hot' electron population, and the other is 'coherently driven by the laser'.

Based on these considerations, one can distinguish two major cases for laser-driven ion acceleration, depending on target thickness: The most investigated and studied case for laser-driven ion acceleration is laser-plasma interaction with targets of $>$ µm thickness. The interaction of the laser pulse with the plasma in this case generates a dense hot electron stream that spreads through the target and eventually reaches the rear side. When this electron cloud exits into the vacuum, a very strong sheath electrostatic field at the target surface is established. Some electrons escape this globally binding field, but the majority of electrons remains macroscopically bound. They bounce back into the target and spread transversely. Ions are then accelerated by this sheath field that points predominantly normal to the target rear side. In this process, protons are accelerated from the target rear (non-irradiated) surface [78]. This acceleration mechanism is referred to as Target-Normal Sheath Acceleration (TNSA).

It yields a very broad exponentially decaying energy spectrum, with a characteristic maximum ion energy E_{max}.

When pre-pulses of the laser are suppressed, nm thin targets can remain overdense up until the main pulse interaction. Then, the laser can indeed act on a large portion of the electrons within the focal volume and a highly efficient acceleration mechanism can take over, in particular when generation of 'hot' electrons is suppressed. Ions can then be dragged along and accelerated more efficiently. This process is referred to as 'laser-piston' or 'Radiation-Pressure-Acceleration' (RPA) regime [79], which has the advantage of a reduced divergence angle that is constant over the spectrum [80].

There are also descriptions of acceleration mechanisms that operate between these two extremes. In the Break-Out-Afterburner (BOA) regime, the interaction of a laser with peak intensity of $10^{21}\mathrm{W\,cm^{-2}}$ with 30 nm foils, for example, can first initiate TNSA. At an intermediate stage, when the plasma becomes (relativistically) underdense, the laser-electron energy transfer increases and allows to heat all electrons of the interaction regions effectively. This allows strong acceleration fields, which result in significantly higher maximum ion energies then expected from pure TNSA [81].

For laser-driven ion acceleration at intensities of $10^{20}\ \mathrm{W\,cm^{-2}}$ from 100s of nm thick foils we expect a dominance of TNSA, while relativistic transparency can already play a role.

In view of the complexity of the processes, there is no exact estimate of the expected energies. However, there are theoretical models that calculate a maximum kinetic proton energy, based on laser and target parameters, for example [82] [83] [84]. Additionally, studies have investigated a magnitude of results and tried to find empirical models based on experimental data [84] [85] [86]. A conclusive description of the expected differential energy spectrum, however, is not available yet.

It is therefore instructive to review such spectra obtained from experiments with a wide variety of parameters [88] [87]. Regardless of the specific acceleration mechanisms at play, progress was driven by technological improvements in targets and laser pulse quality. Figure 3.2 shows such spectra over a range of laser pulse energy. Glass laser systems typically have temporal FWHM pulse widths $> 500\,\mathrm{fs}$, whereas Titanium:Sapphire laser systems have pulse widths of tens of fs. It is evident that higher laser energy leads to the observation of higher kinetic ion energies. For applications, the number of particles accelerated to a certain energy is equally, if not more important. This number increases as well with higher laser pulse energies.

Next we explain a typical diagnostic approach that is based on magnetic spectrom-

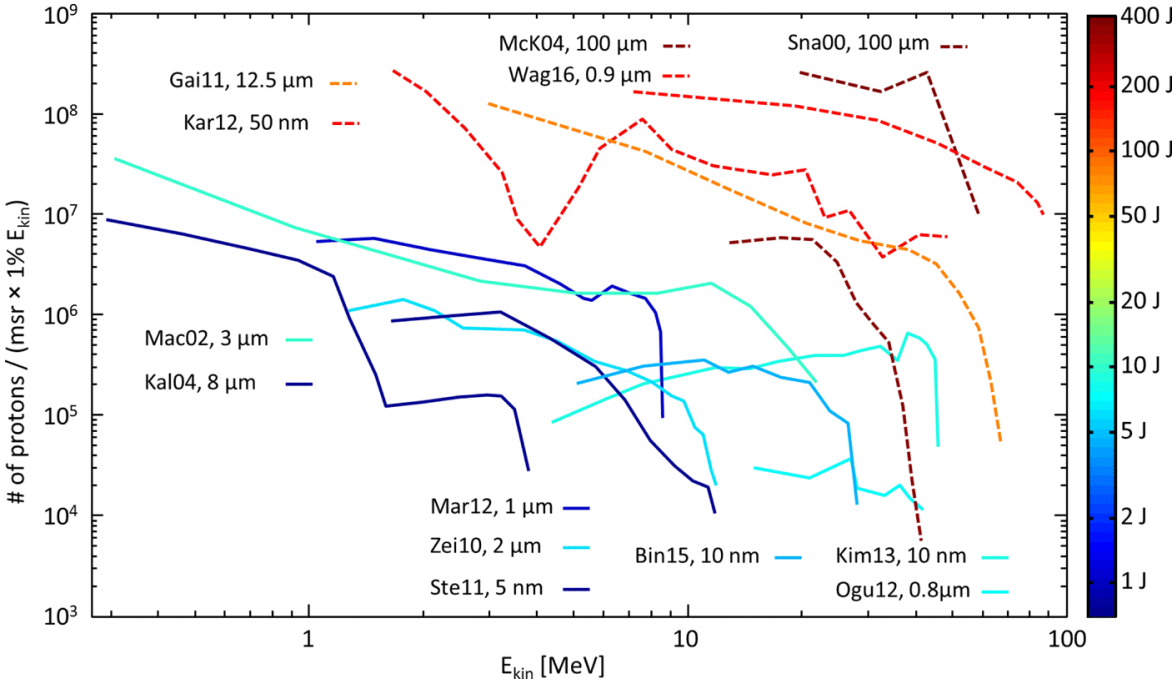

Figure 3.2: Differential proton kinetic energy spectra from Glass (dashed) and Titantium:Sapphire (solid) laser systems. Laser energy on target is represented by the color bar, target thickness is noted in the plot. Figure from [87].

eters for sampling a small portion of the ion bunch emitted from the plasma. This simple approach is widely used and delivers fast insight. Quantitative analysis, however, requires typically cumbersome calibration procedure. Although rather simple, it is important to understand the concept of spectrometry as a basis of the new QIS method that will be presented in chapter 4 and circumvents these problems.

3.2 Deflection by a Wide-gap Magnetic Dipole

Moving charged particles are deflected by magnetic fields. The acceleration perpendicular to the propagation of particles is proportional to the charge-to-mass ratio and momentum. This section contains a calculation of the spatial kinetic energy dispersion of a particle bunch propagating through a spatially inhomogeneous magnetic field. Figure 3.3 shows a typical experimental setting of a particle spectrometer that is strictly correct only for homogeneous fields. The magnetic field is inhomogeneous along the propagation direction z, but this has little influence on our argumentation, because the actual displacement within the magnet is small. It is also inhomogeneous in direction x, that is along the entrance slit. In the following, the main component of the mag-

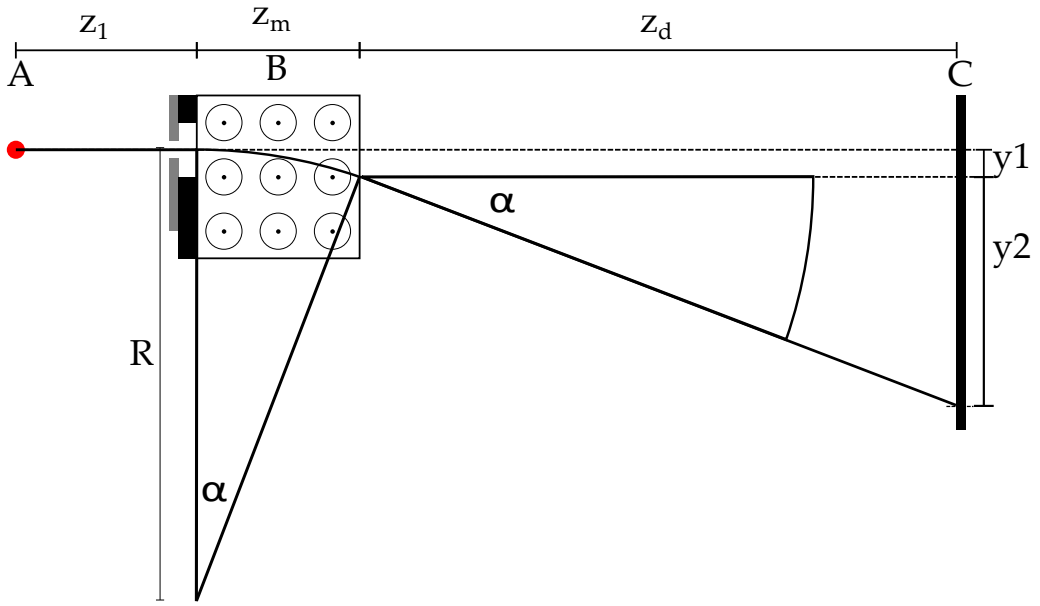

Figure 3.3: Schematic of dipole deflection. Particles from the point source A propagate through a slit and enter the dipole field B. After deflection they drift towards detector C. The trajectory is shown for a positively charged particle with defined kinetic energy.

netic field $B_x(x)$ represents an z-averaged value that obeys $B_x(x) = \int B_x(x,z)dz/z_m$. Particles are propagating in positive z-direction, and magnetic field lines are parallel to the x-axis (and the entrance slit), facing towards the reader. We will derive the amount of deflection in the y-axis y_d and the x-axis x_d at the detector plane for particle kinetic energy $E_{kin} = (\gamma - 1)m_0c^2$. With the detectors spatial resolution, we can then relate spatial positions to particle energy $x_d(E)$ and $y_d(E)$.

The magnetic field is inhomogeneous along x because in typical setups of wide-angle spectrometers (WASP) [22] the gap width is of the same order as the length of the magnetic field. An approximation for this functional behaviour has been studied in the Bachelor's thesis of P. Kühnemann [89]. It was found that the following approximation can be made for the magnetic dipole field:

$$B_x(x) = a(x-d)^4 + b(x-d)^2 + c \tag{3.1}$$

Second, the y-deflection of the magnet relative to straight propagation of particles along the z-axis can be calculated as follows:

$$y_d = y_1 + y_2 \tag{3.2}$$

y_1 is the offset after propagating through the magnet. The magnetic field lines are perpendicular to the ion-bunch propagation axis, and its deflection can be calculated with the Lamor radius

$$R = \frac{mv_z(E_{kin})}{qB_x} = \frac{\beta_z \gamma m_0 c}{qB_x} \tag{3.3}$$

The angle α is given by the Lamor radius and length of dipole via $sin(\alpha) = \frac{z_m}{R}$ and results in $y_1 = R(1 - \sqrt{1 - sin^2\alpha})$ and $y_2 = z_d * tan(\alpha)$. Hence

$$y_d = R\left(1 - \sqrt{1 - (\frac{z_m}{R})^2}\right) + \frac{z_d z_m}{R\sqrt{1 - (\frac{z_m}{R})^2}} \tag{3.4}$$

The setup of this thesis allows to consider $\frac{z_m}{R} << 1$. Thus, we can approximate

$$y_d \approx \frac{(\frac{z_m}{2} + z_d) z_m}{R} \tag{3.5}$$

Then we get

$$y_d = \frac{(\frac{z_m}{2} + z_d) \cdot z_m q B_x}{\gamma \beta m_0 c} \tag{3.6}$$

With $\zeta = (\frac{z_m}{2} + z_d) z_m q/(m_0 c)$ and m_0 the particle mass, q the particle charge, c speed of light in vacuum, we rearrange for the normalized particle momentum $\gamma\beta$

$$\gamma\beta(x, y_d) = \frac{B_x(x)}{y_d} \cdot \frac{(\frac{z_m}{2} + z_d) \cdot z_m q}{m_0 c} =: \frac{B_x(x)}{y_d} \cdot \zeta \tag{3.7}$$

Then, with $E_{kin} = m_0 c^2(\gamma - 1)$ we obtain

$$y_d(E_{kin}, x) = \frac{E_r B_x \zeta}{\sqrt{E_{kin}^2 + 2E_r E_{kin}}} \tag{3.8}$$

In the following we will drop the index $_d$, and refer to this deflection as y instead of y_d.

3.3 Wide Angle SPectrometer (WASP)

The Wide-Angle Spectrometer (WASP) is the main ion-diagnostic in CALA LION, and the ion data of this thesis have been recorded with this setup. The ion beam cone from the laser-target interaction, the target chamber centre (TCC), is passing through

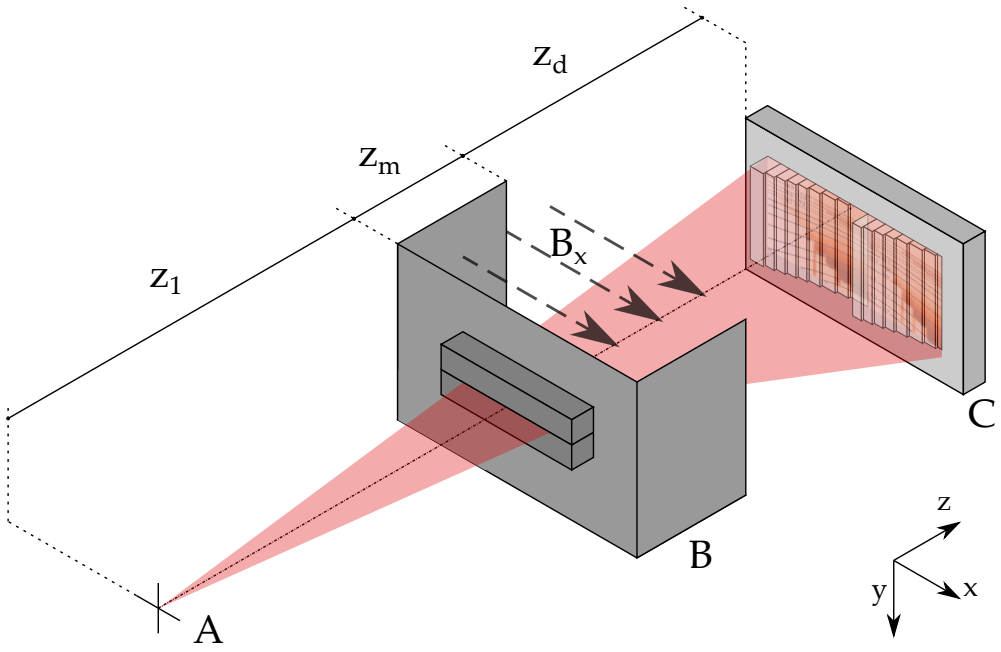

Figure 3.4: Schematic dipole and wide-angle spectrometer picture. A is the ion source. B is the dipole magnet with slit aperture. C is the detector covered by the aluminum phantom 'PABLONE'.

a $w = 200\,\mu m$ slit aperture made of 3 mm thick aluminum. The slit is 5 cm wide and parallel to the x-axis. This aperture is right at the entrance of a dipole magnet with a 10 cm wide gap at $z_1 = 83\,cm$ distance from TCC. The magnetic field is $z_m = 10\,cm$ long. Afterwards, the ions drift $z_d = 68\,cm$ towards the detector housing, which is covered with an aluminum phantom (PABLONE) and contains the Radeye1 detector.

The RadEye1 is a complementary metal-oxide-semiconductor (CMOS). A detailed description of the setup and operation including the software called 'CamOuflage' has been done by W. Draxinger [90]. S. Reinhard successfully demonstrated the use of this detector for detection of laser-driven protons and found that the detector is single-proton sensitive, responds linearly to particle number and has no noticeable cross talk between pixels [91] [92]. Since then the detector has been continuously used for laser-driven ion as well as electron detection [93] [94]. The basic function of the silicon detector is relevant for the newly introduced QIS method and will therefore be captured in more detail in section 3.5.

A single RadEye1 element has the size of 5 x 2.5 cm with 1024 x 512 pixels, where each pixel is 48 x 48 μm^2. The pixels are read out in Analog to Digital Units (ADU) and have a dynamic range of 12 bit, thus ranging from 0 to 4095 ADU. Up to four

elements can be controlled by a single read-out unit. We positioned these elements side by side, yielding a total active area of 5 x 10 cm with 1024 x 2048 pixels. A $\approx 2\,\mu m$ thick silicon oxide protective layer is covering the active $\approx 2\,\mu m$ thick silicon layer. These thicknesses have been provided by the manufacturer in private communication and are not exact or published. Further specifications and measurements are available in the data sheet [95]. The operation details and improvements to the software and readout are described in appendix A.1.

Using a magnet with a wide aperture allows to sample a larger solid angle of the emitted ions in a single shot [22]. We use the large irradiated surface on the detector to calibrate the magnetic deflection for our evaluation, which is particularly important because the wide gap requires to consider an inhomogeneous magnetic field for particle deflection.

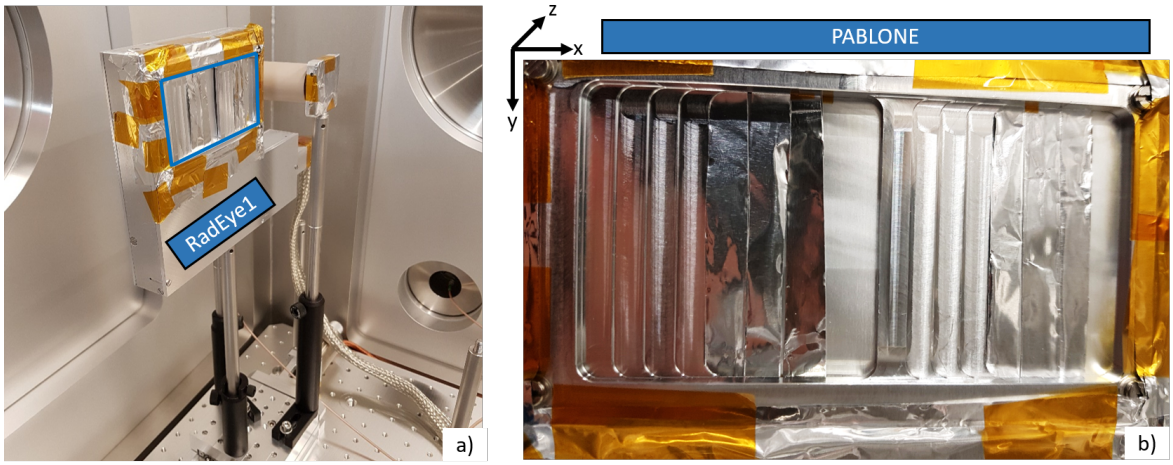

Figure 3.5: RadEye1 and PABLONE image

The aluminum phantom, named 'PABLONE', consists of adjacent vertical aluminum stripes, that cover the complete detector active area. An image of the current iteration is shown in figure 3.5 b). The thicknesses of all stripes are known. In the detector coordinate frame, the thickest stripe, 4112 µm thickness, is at x = 0. Propagating towards positive x-direction, we find 8 stripes which are decreasing in thickness along increasing x position. The thinnest stripe is 112 µm thick. Adjacent to those, the same 8 thicknesses appear in the same decreasing order again. Thus two stripes of the same thickness are spaced apart. In total, 17 stripes cover the detector. PABLONE is positioned directly in front of detector C in figure 3.4.

The aluminum thicknesses have been chosen such, that their respective proton cut-off energies are dispersed approximately equidistant on the detector surface. Table 3.1

xCenter	Aluminum [µm]	$Ecut_{proton}$ [MeV]	$Ecut_{carbon}$ [MeV/u]	Overlapping elements
1080	112	3.67	6.7	yes
2015	112	3.67	6.7	
920	142	4.22	7.8	
1911	142	4.22	7.8	
751	202	5.2	9.6	
1790	202	5.2	9.6	
634	292	6.5	12.0	
1650	292	6.5	12.0	
516	512	8.9	16.5	yes
1530	512	8.9	16.5	yes
410	892	12.3	22.7	
1440	892	12.3	22.7	
310	1472	16.3	30.0	
1321	1472	16.3	30.0	
190	2202	20.5	37.7	
1220	2202	20.5	37.7	
90	4112	29.1	53.4	

Table 3.1: List of detector aluminum phantom stripes, their positions, their thicknesses and respective proton and carbon cut-off energies. Three stripes overlap two detectors.

is listing the used aluminum thicknesses with their respective cut-off energies, as well as 'xCenter', which is the x-Axis coordinate in detector pixels, and used to name the evaluated area of the detector.

3.4 Differential Energy Spectrum

The slit in front of the magnet truncates the emitted ion 'spray' into a fan-beam. We aim at determining the differential energy spectrum in a small solid angle $d\Omega$ around the target normal direction.

The differential energy distribution, that is the number of ions per energy interval and solid angle as function of energy for one selected angle to target normal, typically close to 0°, is

$$\frac{dN}{dE_{kin}}(E_{kin})\frac{1}{\Delta\Omega} = \frac{dN}{dy}(E_{kin})\frac{dy}{dE_{kin}}(E_{kin})\frac{1}{\Delta\Omega} \tag{3.9}$$

and with equation (3.8)

$$\frac{dy(E_{kin},x)}{dE_{kin}} = -\frac{E_r B_x \zeta (2E_{kin}+2E_r)}{2(E_{kin}^2+2E_r E_{kin})^{3/2}} \tag{3.10}$$

Note that $\left|\frac{dy(E_{kin},x)}{dE_{kin}}\right|$ decreases with increasing E_{kin}. For a detector with a fixed spatial resolution this translates to decreasing energy resolution for faster particles. Now consider the setup in figure 3.4. The cone emitted from the target (A) is truncated by the slit. The remaining 'fan'-beam is dispersed in the magnetic field (B) before hitting the detector (C). We consider the dimensions x and y separately. The slit width w defines the extent in y-dimension. The pixel size x_{size} of the detector defines the solid angle in the x-dimension. The projection of w onto detector (C) is:

$$y_{size} = w(1+\frac{z_d+z_m}{z_1}) \tag{3.11}$$

Therefore, the solid angle is

$$\Delta\Omega = \frac{x_{size}\cdot y_{size}}{(z_1+z_d+z_m)^2} \tag{3.12}$$

The term $\frac{dN}{dy}$ equals the number of particles dN that impact the detector in a region $y(E_{kin}) \pm dy/2$. dy is associated with the projected y_{size} and restricts also the energy resolution.

dN is the particle number within the evaluated detector segment. It can be obtained when the response of the detector to the particle energy loss is known.

3.5 Silicon Particle Detectors

If n- and p-type semiconductors are joined, electrons will diffuse from n to p until an equilibrium state establishes. This results in an intrinsic potential difference at their border V_{bi}. Charge carriers are drawn from this 'junction' region, which significantly increases electrical resistance. This effect can be increased by applying a potential, called reverse bias V_b, with positive polarity on the n-side and negative on the p-side. Such a 'pn-junction' can be used as a silicon particle detector [96]. A particle passing through the active layer deposits an energy Δ inside the junction. This creates electron-hole pairs if Δ is larger than the Ionization energy E_i (3.6 eV for silicon). The potential of the pn-region then separates these pairs, resulting in a current. Integrating

this current over time yields the charge Q_s

$$Q_s = \frac{E}{E_i} e \tag{3.13}$$

Thermal excitations can promote electrons across the band gap, therefore the junction is not a perfect insulator, and allows some 'dark current' to flow even without ionization events. This reverse bias current depends on the energy required to cross the band gap E_g (1.12 eV for silicon), and on temperature T:

$$I_R \propto T^2 exp(-\frac{E_g}{2k_b T}) \tag{3.14}$$

with Boltzmann constant k_b. To reduce this background contribution it is favorable to cool the detector.

The integrated current (charge) is first amplified by a pre-amplifier, digitized by an analog-to-digital converter and stored by a computer. The resulting values are refered to as Analog to Digital Units (ADU). The RadEye1 detector used for this work has shown to have a linear response, thus ADU are proportional to energy deposited in the active layer [91].

Irradiation of the detector can damage the pn-junction and degrade its performance. This is called radiation damage. Displacement of electron-hole concentrations result in higher dark current for damaged pixels. Dark images start to have visible 'imprints' in areas that have been irradiated regularly. The data discussed in this work has been recorded with previously unused detector elements, and radiation damage has not been observed.

In order to reduce high leakage currents at the device edges, which would lower the devices performance, guard ring structures surround each pixel. They isolate the junction from the edges and define an electrical device boundary. They also introduce dead detector areas which can not be used for particle detection. The presented method does not take these restraints into consideration, and rather assumes the complete pixel to be sensitive.

3.6 Energy-loss of Charged Particles in Matter

3.6.1 Average and most probable energy loss

The description in these sections follows closely the work "Passage of particles through matter" by Groom et al. [97] from which relevant informations for this thesis have been extracted. This includes considering the relevant parameter range, which allows some simplifications.

As fast charged particles traverse through matter, they will interact with this 'target' material predominantly via electronic interaction mediated by the Coulomb force. The collisional energy loss divides into two contributions: The dominating "soft" collisions with energy transfers from zero to an intermediate energy W_0 and "hard" collisions with energy transfers from W_0 to the maximum W_{max} [98]. For point-like particles with mass $M >> m_e$

$$W_{max} = \frac{2m_e c^2 \beta^2 \gamma^2}{1 + 2\gamma m_e/M + (m_e/M)^2} \tag{3.15}$$

$M = 938.265\,\mathrm{MeV/c^2}$ is the rest mass of a proton, and $m_e = 511.004\,\mathrm{keV/c^2}$ the rest mass of an electron. The contribution of $(\frac{m_e}{M})^2$ is negligible and was dropped for the evaluation calculations to stay coherent with [99]. These electronic interactions occur in single collisions, with energy losses W leading to ionization and atomic or collective excitation. The few collisions that take place in thin absorbers will show a large variance, as discussed later in this section. Particles with an initial kinetic energy of E_0 passing through a target lose the energy $\Delta = E_0 - E_1$. E_1 is the remaining kinetic energy of the particle when exiting the material. Below the cut-off energy $Ecut$ the particle's kinetic energy will be insufficient to leave the target material and it is stopped within. Based on the assumption of interactions with free electrons, Bethe has derived a differential energy loss based on a first-order Born approximation. At $\beta\gamma < 0.1$ the projectile speed is comparable to those of bound electrons, and requires a more refined treatment. Radiative effects become relevant at $\beta\gamma \approx 1000$. Within these limits, the mean rate of energy loss $\left\langle \frac{dE}{dz} \right\rangle$ is given by the Bethe-Bloch equation [97]

$$\left\langle \frac{-dE}{dz} \right\rangle = K z_e^2 \frac{Z}{A} \frac{1}{\beta^2} \left[\frac{1}{2} ln \frac{2m_e c^2 \beta^2 \gamma^2 W_{max}}{I^2} - \beta^2 - \frac{\delta(\beta\gamma)}{2} \right] \tag{3.16}$$

In this definition, it is the mass stopping power in units of $\mathrm{MeV\,cm^2\,g^{-1}}$. Z is the atomic number and A the atomic mass number of the target. Projectile charge in units of elementary charge e is given by z_e. Constants have been summarized by

$K = 4\pi N_A r_e^2 m_e c^2 \approx 0.307\,\mathrm{MeV\,cm^2\,mol^{-1}}$, where N_A is Avogradro's number and r_e the classical electron radius. For silicon the mean excitation energy is $I = 173\,\mathrm{eV}$ [97], and density $\rho = 2.329\,\mathrm{g\,cm^{-3}}$ [100]. $\beta = \frac{v}{c}$ and $\gamma = (1-\beta^2)^{-\frac{1}{2}}$ are velocity and relativistic gamma-factor of the incident particle. Density correction δ is negligible for the relevant protons with energy $E_0 < 100\,\mathrm{MeV}$.

3.6.2 Ionization Energy Loss of Fast Particles in Thin Layers

The energy loss probability for layers of material with moderate thickness with respect to the range of incident particles is adequately described by the highly skewed Landau-Vavilov distributions. Landau has first undertaken the derivation of the energy loss distribution for electrons in thin layers of matter [101]. The resulting function is highly skewed, such that the most probable energy loss Δ_p is significantly smaller than the average energy loss ΔE obtained from Bethe-Bloch. This shift is due to the weight of rare events in which a large energy transfer can happen.

For his derivation, Landau considered fast particles with an incident energy E_0 traversing a thin layer of matter such that the total energy loss $\Delta = E_0 - E << E_0$. The unknown distribution function $f(\Delta z, \Delta)$ shall then be the normalized probability that a particle with initial energy E_0 loses an amount of energy $\Delta < W < \Delta + d\Delta$ while traversing a layer Δz. The total energy loss Δ shall be small compared to the initial energy E_0, such that the probability of energy loss per unit length may be considered independent of the final energy E_1.

Landau introduced the scaling variable:

$$\xi = \frac{K}{2}\frac{z_e^2 Z}{A\beta^2}\tau \tag{3.17}$$

with $\tau = \rho\Delta z$ as the absorber thickness in $\mathrm{g\,cm^{-2}}$ [102].

Vavilov has extended the approach for heavier particles, such as protons [103]. Based on Landaus work, he introduced $\kappa = \frac{\xi}{W_{max}}$ (referred to as Vavilov parameter), which is the ratio of the energy loss scaling variable to the maximum possible energy transfer in a single collision. For $\kappa < 0.01$ the energy loss distribution function approaches the one derived by Landau, the Landau distribution. For $\kappa > 10$ it approaches a Gaussian shape. Vavilovs result describes the distribution shapes of energy loss in between these extreme cases. We refer to these functions as Landau-Vavilov distributions.

κ for the relevant range for this thesis is shown in figure 3.6. These curves are

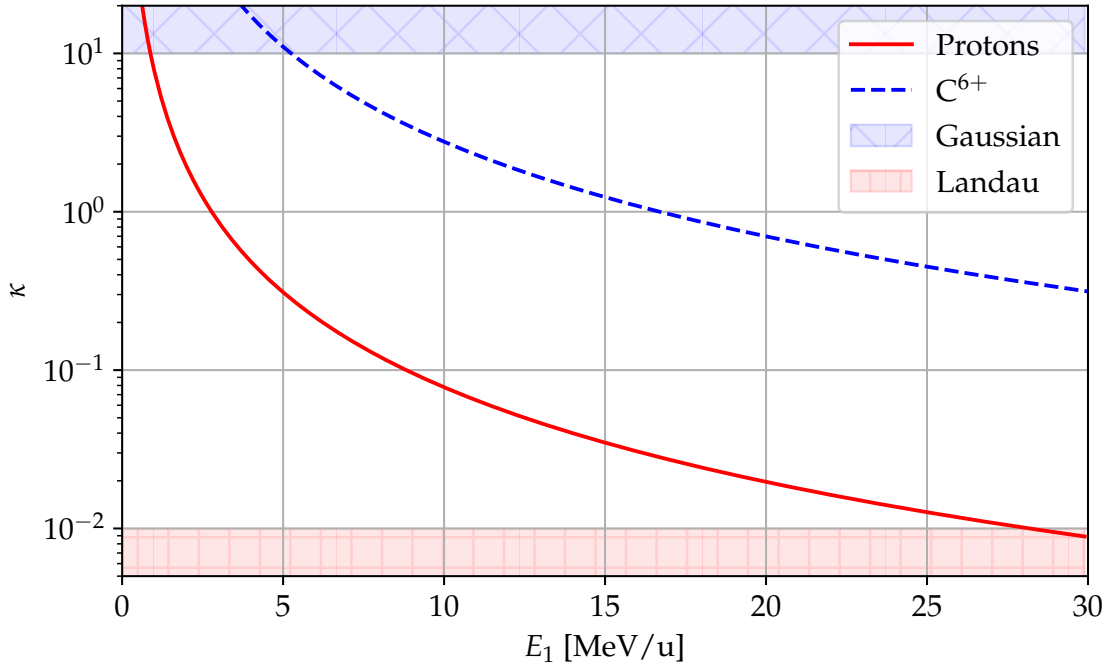

Figure 3.6: κ versus kinetic energy E_1, with which the particles enter a 2 µm thick silicon layer. For κ>10 a Gaussian approximation and for κ<0.01 a Landau distribution may be used to model the energy loss distribution.

calculated for energy loss in 2 µm thick silicon, which represents the detector active layer thickness to the best of our knowledge, for incident kinetic energies E_1 for protons (H^+) and carbon ions (C^{6+}). Protons with E_1 in the range from 1 to 28 MeV and carbon ions with E_1>5.3 MeV/u are within $0.01 < \kappa < 10$. Thus, for our region of interest, we expect an energy loss given by Landau-Vavilov distributions.

The ROOT library [104] offers a fast computational implementation of these distribution functions. Vavilov distributions are available as `VavilovFast` [105], which is implemented as described by Rotondi [99]. Input parameters are β^2 of the incident particle, κ as described above and the Landau variable λ which is related to energy-loss Δ as given by Rotondi:

$$\lambda = \frac{\Delta}{\xi} - 1 + C_{EM} - \beta^2 + ln\kappa \tag{3.18}$$

where $C_{EM} \approx 0.5772$ is the Euler-Mascheroni constant.

Energy loss distributions calculated with ROOT are shown in figure 3.7 for protons with kinetic energies E_1 of 6, 7 and 15 MeV as an example. The change of the distribution function shape is significant.

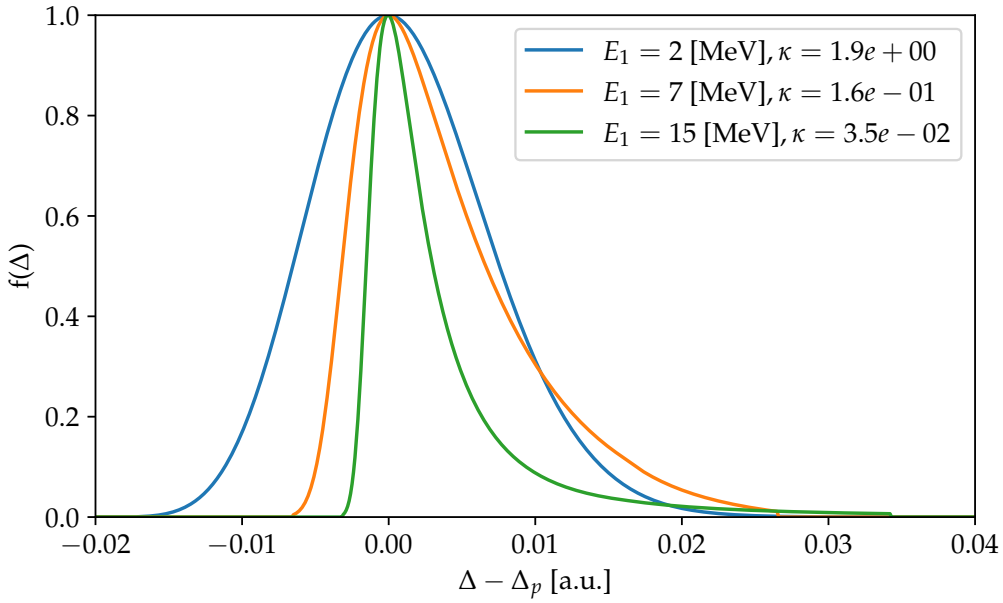

Figure 3.7: Exemplary normalized Landau-Vavilov distributions, centered at the most probable energy loss Δ_p. They correspond to the expected energy-loss distribution of protons inside a 2 µm thick silicon layer.

The most probable energy loss Δ_p is [106]:

$$\Delta_p = \xi \left[ln \frac{2m_e c^2 \beta^2 \gamma^2}{I} + ln \frac{\xi}{I} + 0.200 - \beta^2 - \delta(\beta\gamma) \right] \tag{3.19}$$

This equation appears similar to the energy loss by Bethe eq. (3.16) multiplied by thickness Δz (ξ is an energy and contains the same pre-factors as in the Bethe-Bloch equation). The dependence on material thickness Δz is different, however.

This introduces a discrepancy in the deposited energy Δ, which can be calculated with both equations. Figure 3.8 shows the energy loss for protons with incident kinetic energy E_1 in a 2 µm thick silicon layer and has been calculated with equations (3.16) and (3.19). Within the relevant E_1 range, the 'Evaluation Range', their penetration depth is larger than the silicon layer thickness, so that $E_1 > \Delta$. In this figure, the mass stopping power given by Bethe and the tabulated data have been scaled with silicon material parameters $\rho = 2.329\,\mathrm{g\,cm^{-3}}$ [100] and $\Delta z = 2\,\mu\mathrm{m}$ to compare with the most probable energy loss given by Δ_p. This includes the assumption that dE/dz does not vary significantly inside a 2 µm thick layer. The Bethe mean energy loss is in good agreement with stopping power data from SRIM [107], but differs from the

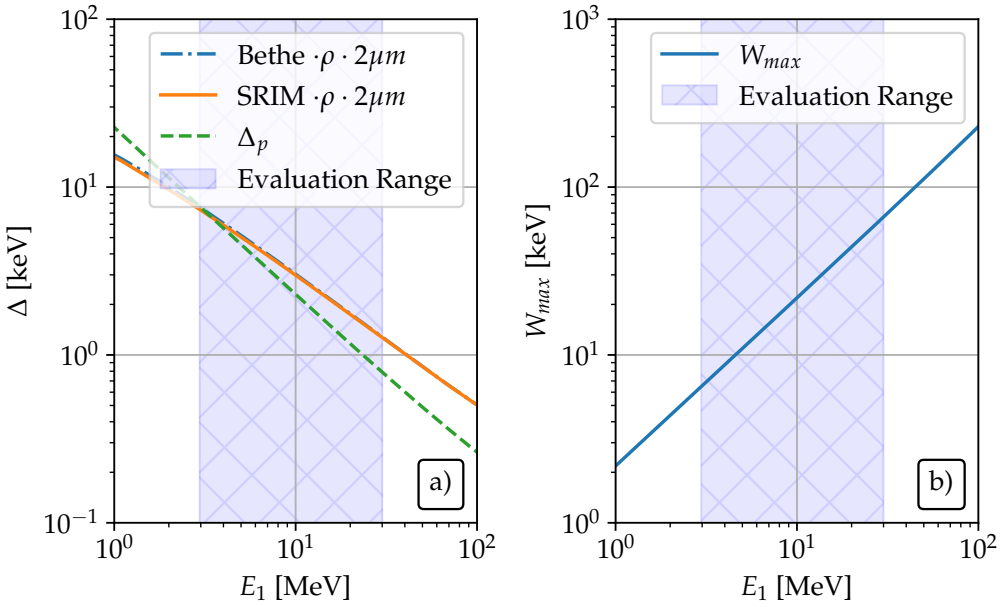

Figure 3.8: a) Energy loss Δ in silicon. 'Bethe' is calculated via equation (3.16) and agrees well with SRIM stopping power tables. The most probable energy loss Δ_p has been calculated as in equation (3.19). b) W_{max} versus incident energy on detector E_1.

most probable energy loss Δ_p. This is important to note, and due to events in which incident particles lose considerable energy. These rare but important contributions shift the energy loss towards higher values. The discrepancy increases towards larger E_1.

The lower boundary of the evaluation range is given by the lowest evaluated energies $E_{min}(202\mu m) = 2.96\,\text{MeV}$, $E_{min}(292\mu m) = 3.15\,\text{MeV}$, which correspond to $\beta\gamma \approx 0.08$. The upper boundary of the evaluation range is $\approx 30\,\text{MeV}$ and $\beta\gamma \approx 0.25$.

In section 3.4 we derived that for a detector with finite spatial resolution, the energy resolution decreases towards higher energies. We can still select areas with similar energy loss in these cases, as $d\Delta_p/dE_{kin}$ and $d\kappa/dE_{kin}$ are decreasing towards higher E_{kin} as well. Therefore, we can treat small enough detector segments as areas which have been irradiated with a proton bunch, of which all particles have the same energy loss distribution. This availability of sub-samples of a larger section is key to the statistical evaluation of the detector signals in the context of QIS (chapter 4).

3.7 Statistical Analysis

The detector used for this thesis is sensitive to energy loss by single protons [91]. It has N_{total} = 1024 x 2048 pixels which are read out simultaneously. The detector can be divided into areas much larger than the single pixel size and still cover very similar kinetic energy given by the dispersion of the magnetic field (section 3.2). These macro-regions (or macro-pixels) will be referred to as mono-energetic regions. They typically contain $n = 549$ pixels, which is an a priori number for now. The mono-energetic feature is important because Δ_p and the shape of the energy loss distribution $f(\Delta)$ vary with incident E_1.

The energy loss distribution of the incident protons determines the energy loss of every single proton passing through the detector, as explained in the last section. We can examine all energy loss events by generating a histogram of all pixel values inside a mono-energetic area. As such, the histogram will also follow the energy loss distribution $f(\Delta)$. For a single proton, we expect a Landau-Vavilov distribution. Additionally, there is a significant chance for multiple protons passing through a single pixel and the consequences of these multiple hits have to be considered. Also, real world detectors have background distributions, which have an impact on signal shape.

We present these three contributions separately and explain how they contribute to the complete raw data histogram. We refer to the raw data histogram as 'histogram', which is considering measured data only. The expected distribution shape will be called Signal Distribution Function (SDF) and is a continuous function, a model of our data.

We will start with the probability distribution of multiple hits per pixel. Then, we take the knowledge of the single proton energy loss distribution and explain its impact on the signal. We describe how background contributions change this shape. Finally, we derive the complete description of the detector histogram, the SDF, and explain how it is used to determine particle numbers in specific mono-energetic regions.

3.7.1 Signal Distribution Function

Binomial Distribution We shall derive the probability of k protons passing through a single pixel: In a single read-out, we have N protons, which can pass through n pixels. There is an equal chance for a single incident proton to hit any of these n pixels, because the detector opening angle for a single mono-energetic area is small. Thus the probability p to hit a pixel is distributed uniformly $p = 1/n$. For this situation, the

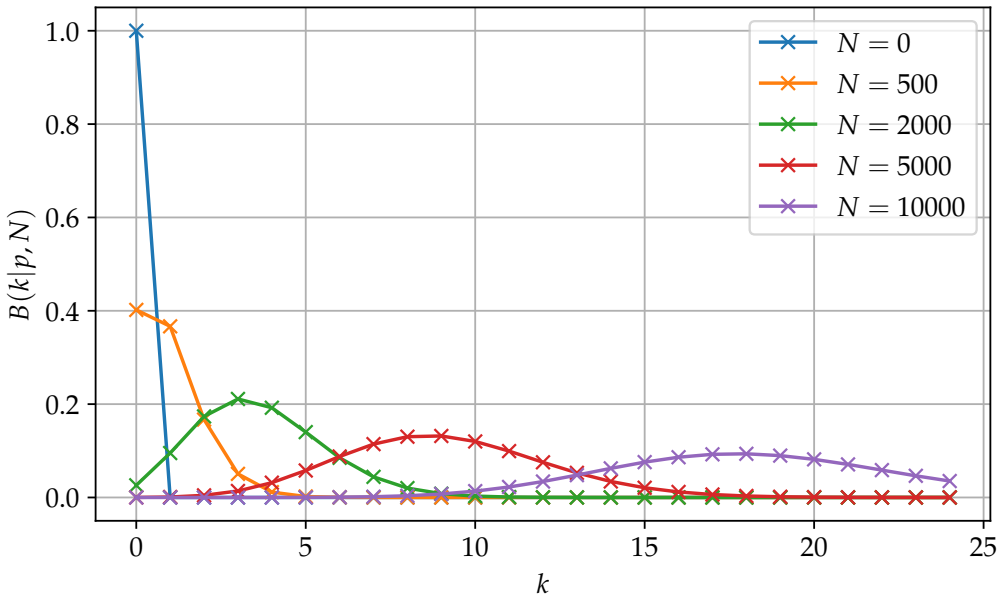

Figure 3.9: The Binomial distribution $B(k|p, N)$ represents the probability of k proton hit events in a single pixel. The area of evaluation contains $n = 549$ pixels. Different lines correspond to the increasing number of incident protons N, which also increases the probability for multiple proton hit events.

binomial distribution applies:

$$B(k|p, N) = \binom{N}{k} p^k (1-p)^{N-k} \tag{3.20}$$

$B(k|p, N)$ is the probability to get k successes with N trials. In our case that is the probability of events, where pixels have been hit by k protons, given that we know that our analyzed area consists of n pixels and was irradiated by N protons. Thus, $B(k|p, N)$ is the probability of multiple protons hitting a single pixel (the chance for a 'k proton hit') inside our mono-energetic area. Example distributions for this thesis' parameters are plotted in figure 3.9.

Zero protons hitting the detector result in a zero probability of detecting $k > 0$ hits per pixel. This is an important case because then only background signals would be measured. $N = 500$ protons already have a significant contribution not only of single, but also double proton hits, and at $N = 5000$ protons the chance of finding any pixel without proton signal $B(0|p, N)$ is approaching 0.

Multiple proton hits are therefore not only non-negligible, and have to be taken in consideration, but offer a new interpretation for the understanding of energy loss

data obtained from a single mono-energetic region. Consider each of the N protons contributing a constant value to the signal (and no other contribution such as background would be present), then the binomial distribution would be identical to the SDF. Therefore, the binomial distribution can be understood as an envelope of the SDF on large scale.

Ion Signal In section 3.6.2 we have learned that the energy loss (for our case) is governed by Landau-Vavilov distributions $f(\Delta)$. For mono-energetic areas every incident proton is governed by the same $f(\Delta)$. The shape of this distribution becomes apparent only if single proton hit events dominate and no background is present. Because we assume that proton hits are uncorrelated, the energy loss of two protons will be a convolution of its Landau-Vavilov distribution $f(\Delta)$ with itself. For this we introduce the notation $g_k(\Delta)$ with k noting the number of protons

$$g_2(\Delta) = f(\Delta) * f(\Delta) \tag{3.21}$$

Additional protons passing through this pixel are uncorrelated as well, and their energy loss is calculated by convoluting the $k-1$ distribution with an additional proton hit:

$$g_k(\Delta, k) = g_{k-1}(\Delta) * f(\Delta) \tag{3.22}$$

Unless noted otherwise, g_k is normalized to its peak height. The Landau-Vavilov $f(\Delta)$ functions have been obtained from ROOT, as explained in the last section.

Background Our statistical treatment of data enables direct consideration of the background distribution. From data we know that histograms of pure background can be modeled by a Landau distribution, convoluted with a Gaussian, which will be refered to as 'Langau'. We used the **pylandau** package [108] to calculate these functions, and will refer to the background distributions as $bg(\Delta)$. For all simulations a background with the following values of the Langau distribution has been assumed: mpv = 65, η = 3.7 and σ = 3.6. Background is always present, and considered uncorrelated with protons passing through the detector. Therefore, the measured energy loss distribution of single proton events is

$$g_1(\Delta) = f(\Delta) * bg(\Delta) \tag{3.23}$$

A k proton event is then

$$g_k(\Delta) = \begin{cases} bg(\Delta) & \text{if k=0} \\ g_{k-1}(\Delta) * f(\Delta) & \text{if k>0} \end{cases} \tag{3.24}$$

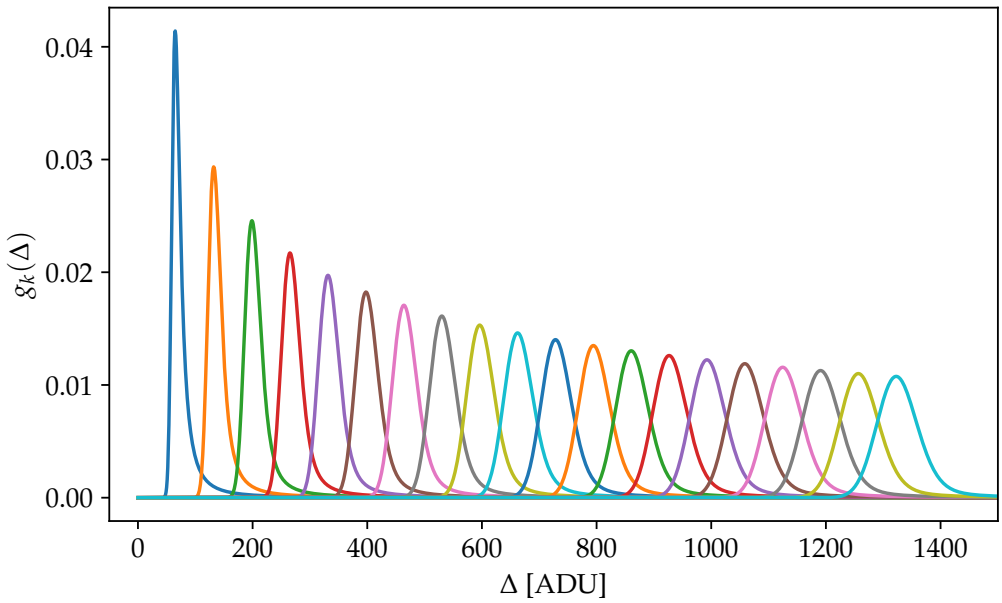

Figure 3.10: g_k for k = 0 ... 19, calculated for protons with an artificial most probable energy loss $\Delta_p = 160$ ADU. Each g_k is normalized to its integral.

Examples are shown in figure 3.10. As one might expect, the most probable energy loss shifts to higher values with increasing k, and the asymmetry of the convolution functions leads to a small shift of the peak. The distributions become broader and more symmetric towards higher k.

Background, Signal and Binomial Distribution Be reminded that the probability of k proton hits is binomially distributed. The complete SDF versus energy loss Δ for N protons distributed in a specific mono-energetic area is:

$$SDF(N, \Delta) = \sum_{k=0}^{\infty} B(k|p, N) \cdot g_k(\Delta) \tag{3.25}$$

In summary, if we know the background distribution $bg(\Delta)$ and the distribution function of single proton energy loss $f(\Delta)$, which peaks at the most probable energy loss $\Delta_p(E_1)$, the only unkown parameter in our mono-energetic region (corresponding to energy E_1) is the number of protons $N(E_1)$. This important result is the key to the

QIS approach.

Fit-Method We have implemented equation (3.25) into a python code: Using python's integrated 1-D curve fitting (scipy.optimize), N is varied until the SDF approaches our histogram most closely. It has been found that adding an additional free parameter to scale the complete function yields a better overlap between normalized data and a SDF. As such, we have

$$SDF_{scale}(A, N, \Delta) = A \cdot SDF(N, \Delta) \tag{3.26}$$

Sum-Method refers to the typical approach, which is used to extract particle numbers from detector signals. There, the background value bg is obtained by averaging over a background image or region. This background value is subtracted from the pixel values pv_i and all values within the evaluation region are summed to yield $PV_{total} = \sum_{i=1}^{n} pv_i - bg$. The sum is then divided by the most probable energy loss of the particle at this energy in units of pixel values Δ_{pv} and the result is the number of protons

$$N_{sum} = PV_{total}/\Delta_{pv} \tag{3.27}$$

Both of these methods require the knowledge of the energy dependent most probable energy loss $\Delta_p(E_1)$. For the sum method, this must be determined in a calibration. We will show in chapter 4, that the statistical evaluation QIS can directly yield this calibration factor by simply treating it as an additional fit parameter.

3.7.2 Fit Performance with Simulated SDF

We have generated artificial SDFs for a range of proton numbers N and artificial most probable energy loss Δ_p and evaluated them with the Fit-Method. The particle number obtained with the Fit-Method N_{fit} is compared to the number of protons of the simulation N_{sim}.

The histogram data is generated with the following method: First, the background is simulated by drawing as many as simulated pixels (n) values from a typical beam-induced background distribution $bg(\Delta)$ which peaks at pixel values of around 65, and storing these into an array where each element represents a simulated pixel. Then, the energy loss of each proton is simulated by obtaining N_{sim} energy losses weighted by $f(\Delta)$. In the next step, each energy loss value is added to a randomly chosen pixel. The histogram of this array is then our artificial SDF. Exemplary histogram

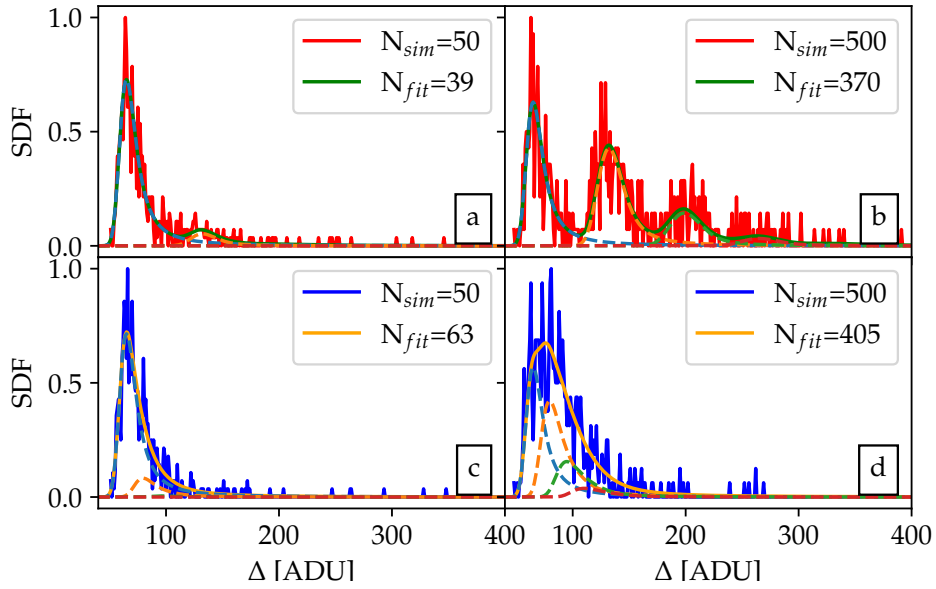

Figure 3.11: Exemplary simulated SDF. Solid lines represent simulated data and the functions obtained with the Fit-Method. Dashed lines indicate the first contributions from g_k, $k \in [0, 1, 2, 3]$ Insets a) and b) correspond to $\Delta_p = 64$ ADU ($E_1 \approx 2\,\mathrm{MeV}$ proton kinetic energy), and c) and d) to $\Delta_p = 11$ ADU ($E_1 \approx 13\,\mathrm{MeV}$ proton kinetic energy). $N_{sim} = 50$ in a) and c), $N_{sim} = 500$ for b) and d). $n = 549$ pixels have been simulated.

data generated from such simulation are shown in figure 3.11. Each simulation is fitted with equation (3.26). The plot insets note the number of N_{sim} and N_{fit}. We chose $\Delta_p = 64$ ADU which is, as we will see later, representative for $E_1 = 2\,\mathrm{MeV}$ protons passing through the sensitive layer of the detector for figure 3.11 a) and b). a) shows a large contribution of background at $\Delta \approx 65$ ADU and a small hump at ≈ 110 ADU. This signature is due to the $N_{sim} = 50$ protons. The histogram data is then evaluated with the Fit-Method, and the green line represents the best fit. It follows the envelope of the data quite well. This fit corresponds to $N_{fit} = 39$ which is smaller than N_{sim}. In b) we have a more distinct peak structure. The first peak is due to background, and the additional peaks are the proton signature. In this example the $k = 1, 2, 3$ proton hits (per pixel) are visible. Their probability is decreasing towards higher k, as expected from the binomial distribution $B(k|p, N)$. The distance between subsequent peaks equals the most probable energy loss values Δ_p. Figures c) and d) are signals expected from 13 MeV protons ($\Delta_p = 11$ ADU), which deposit less energy in the detector. Their signal signature appears to merge with the background contribution,

especially in c), where only 50 protons have been simulated. The Fit-Method, however, can still produce a best fit, the orange line, which approximates the data well, and can retrieve N_{fit}, this time larger than N_{sim}. To investigate the performance further, we have performed a number of simulations within the range of proton numbers and energies (with respective Δ_p values) relevant for this work.

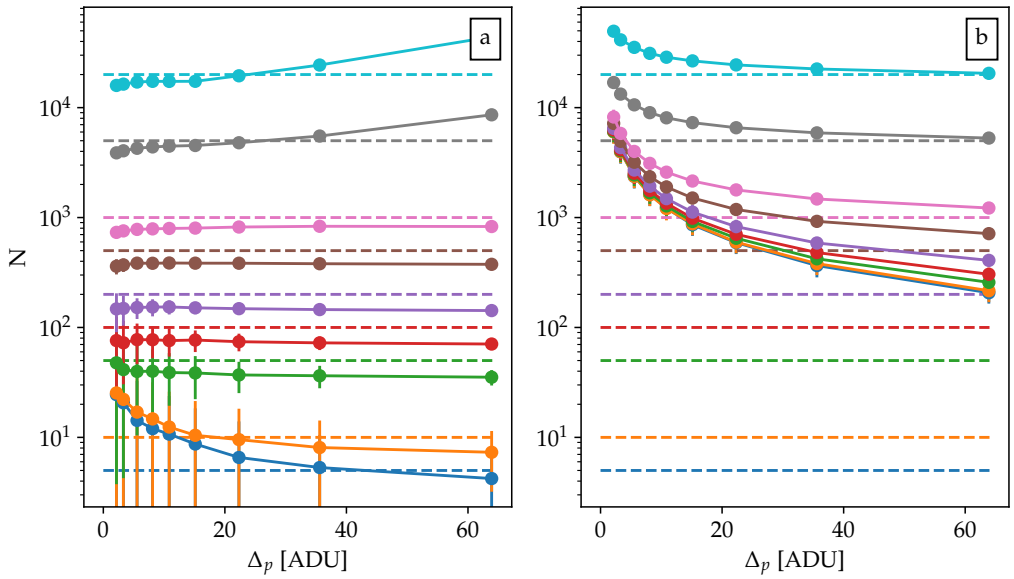

Figure 3.12: Method performance tested on simulated histograms for $n = 549$ pixels. Δ_p, the most probable energy deposition of a single proton in the detector, has been chosen to resemble kinetic proton energies from 2 to 29 MeV. Dashed lines indicate N_{sim}, ranging from 5 to 20000 protons. The solid lines with the same color are values obtained with either method, N_{fit} in a), and N_{sum} in b). For them, each data point represents an average value, obtained from 1000 simulations of the same parameters N_{sim} and Δ_p. Each simulation generated a histogram, with the method explained above, which has then been evaluated with the Fit- and Sum-Method, respectively.

The performance of applying the Fit- and Sum-Methods to simulated histograms of an $n = 549$ pixel mono-energetic area is plotted in figure 3.12. Over the complete Δ_p range (resembling expected values for proton E_1 between 2 and 29 MeV) N_{fit} can reproduce N_{sim} reasonably well and is typically underestimating the particle number.

At lower proton numbers $N_{sim} < 50$ N_{fit} starts to differ significantly and the error bars increase. This indicates that the histogram does not contain sufficient samples to represent the SDF well enough, and the fit fails. This is expected because the statistical treatment requires a sufficiently large number of trials (protons) to resemble the continuous distribution functions.

Between a most likely single proton energy loss of $10 < \Delta_p < 80$ ADU, the ratio between estimated and simulated particle number is nearly constant. For $N_{sim} > 50$, N_{fit} agrees with N_{sim} within a factor of 2. At large particle numbers N_{sim} >1000 and energy loss $\Delta_p > 40$ ADU N_{fit} is overestimating the number of protons. This may be due to the broadening of g_k towards higher k values. If this method is to be translated to other sizes of mono-energetic areas, it is interesting to compare the number of pixels n with N_{sim}. In the presented configuration, the Fit-Method appears to work best for $0.1 \cdot n < N_{sim} < 2 \cdot n$.

N_{sum} is performing well for high energy deposition Δ_p>40 ADU at large particle numbers $N_{sim} > 1000$. This has several reasons. The broadening of g_k with increasing k, shown in figure 3.10, yields more symmetrical distributions. With more symmetry, the difference between average and most probable energy loss value becomes less relevant. Therefore, the proton number can be estimated more accurately by this method. High particle numbers also increase statistics, which also increases accuracy for calculating the mean only. Further, in this method the weight of the background contribution is reduced towards higher energy loss values. However, the Sum-Method overestimates particle numbers at $N_{sim} < 1000$, that is $N_{sim} \approx 2n$, especially for low values of Δ_p, which correspond to higher E_1. This divergence is due to the background contribution, and the highly skewed energy loss distributions $f(\Delta)$. Single events with large energy deposition Δ have a large impact on the pixel sum.

From this result we come to the conclusion that the Fit-Method is a valid approach to the particle number evaluation for our setup, in particular when the resultant proton numbers are between $0.1 \cdot n$ and $2 \cdot n$. It reproduces the incident particle numbers more accurately over a wider range than the Sum-Method, and in particular in regions where the Sum-Method fails.

Chapter 4

Quantitative Ion Spectrometry (QIS)

The goal of QIS is the evaluation and conversion of the ion signal on the detector into an ion kinetic energy distribution, the spectrum. Consider the WASP setup picture in figure 3.4. In the detector x-y plane, consider the x-dimension as an angular distribution (and for now homogeneous). The y-dimension is governed by magnetic deflection, hence energy selection. Deflection depends on the kinetic energy E_0 of the particle. With the energy selection, we define macro-pixels with incident energy E_0 which have been irradiated by an unknown number of protons N. We obtain histograms of all pixel values in these macro pixels $f(ADU)$.

For calibration, we extend SDF by an additional fit parameter mpv_{ADU}, the most probable energy loss for a single proton. We calibrate only with histograms showing a distinct peak structure, allowing to check mpv_{ADU} with visual inspection. From these we obtain our detector calibration. For particle number evaluation, we generate SDF as in section 3.7.1 to $f(ADU)$, using mpv_{ADU}.

In this chapter, we first map an incident kinetic energy E_0 to every detector pixel. With this map, we can select our macro-pixels and obtain raw data histograms. We will then explain how we calibrated the detector quantitatively for protons, and for carbons. We then discuss our choice of background distribution and our investigations into its behavior. Finally, we present how to use the QIS method to obtain particle numbers for differential energy spectra. We will use E_0 to denote the initial kinetic energy of the particle, which governs the dipole dispersion, and $E_1 < E_0$ as the kinetic energy after passing through the aluminum phantom PABLONE, with which the particles enter the active layer of the detector.

4.1 Energy Map on Detector

Measuring or simulating a magnetic field distribution and then tracking particles is often done to calibrate magnetic spectrometers. The tracking requires precise knowledge of the magnetic field and the distances of objects in the setup. This process yields a map of kinetic energy in the detector plane $E_{kin}(x, y)$ and requires simulation knowledge, time and appropriate software, most importantly through tedious measurements (or simulations) of the magnetic field distribution. An example of using this approach is described by Lindner for protons [93] and electrons [94].

Here we present a method that does not rely on any additional information. It is solely based on fitting an analytical magnetic field model to support points provided by the raw data image. The routine is completely implemented in `python`.

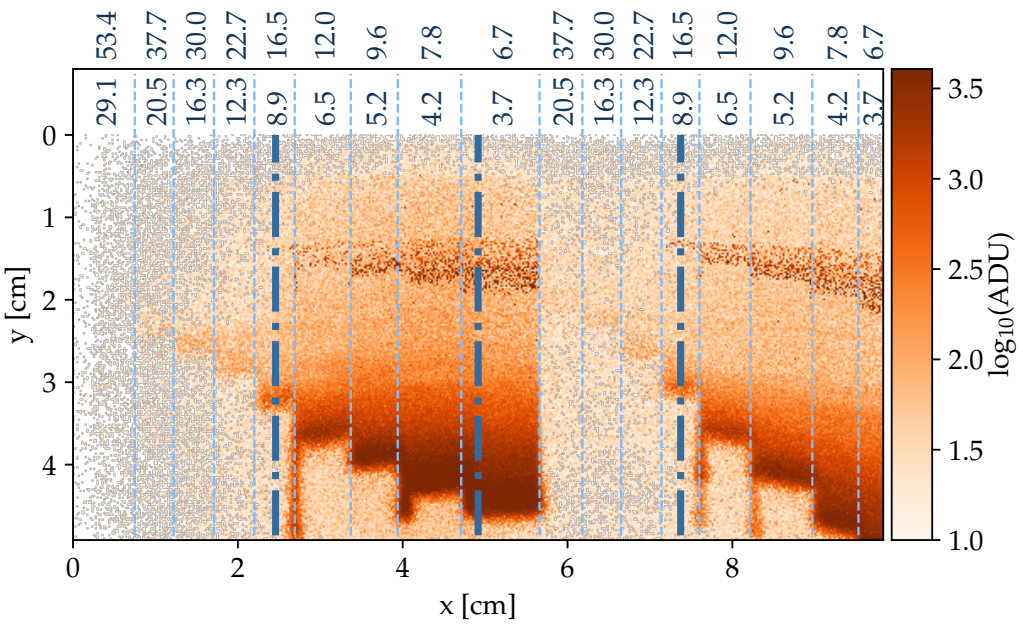

Figure 4.1: Typical image from the RadEye1 detector after subtraction of a non-irradiated image. The dash-dotted lines indicate the borders between the four detector elements. Dashed lines correspond to the borders between different aluminum thicknesses in front of the detector. The corresponding proton cut-off energies E_{co} in MeV are noted below and carbon cut-off energies in MeV/u above the upper canvas frame line. 20% c is $E_{kin} \approx 20\,\mathrm{MeV/u}$.

Visual inspection of raw-image A typical raw image from the detector in a WASP setup is shown in figure 4.1. Four sets of step-like features are visible. The steps at y-axis > 1.8 cm fit the expected deflection of protons within the expected energy range,

whereas the steps at y-axis < 1.8 cm can be attributed to fully ionized carbon ions (C^{6+}). The step feature is the result from the particles passing through PABLONE. The first of its two identical sets of aluminum stripes is visible in this image between 0.7 and 5.6 cm, the second set between 5.6 and 10 cm. An additional thicker stripe is located between 0 and 0.7 cm. Ion signal can only be present at an x-position, if $E_0 > E_{co}$, with E_{co} being the cut-off energy of the respective aluminum thickness. (A lower limit of E_{max} can be estimated qualitatively by visual inspection of the raw-data: In figure 4.1, protons with kinetic energies with $E_{max} > 20$ MeV and carbon ions ($C6^+$) with kinetic energies $E_{max} > 16.5\,\mathrm{MeV/u}$ are visible.)

Signal edge detection For a given x-coordinate, we can scan along the y-axis and determine the largest y-coordinate y with signal. We have implemented a signal edge detection routine that returns the largest y pixel coordinate containing signal for a given x pixel coordinate (typically xCenters). The edge detection routine will first apply a median filter to the image with a bin size of six pixels. It will then cut-out a five pixel wide vertical area centered around xCenter. These are averaged along the x-axis. Figure 4.2 shows such arrays for three different xCenters. The average and standard deviation of pixel values without signal at xCenter are calculated from pixels y = 0 to 50 (where we do not expect any signal). We define this average plus six times standard deviation as threshold (factor six has been identified as best match from visual inspection of many samples). The algorithm then identifies the largest y-coordinate where the pixel value is larger than the threshold. Examples of the obtained y-coordinates are plotted as vertical dash-dotted lines in figure 4.2.

Thus, we have found a coordinate with known kinetic energy $E_{co}(x, y)$, and can repeat this edge detection for additional xCenters. Note that the edge-detection routine requires raw data with sufficiently good ion performance, such that the signal edges for the selected xCenters are clearly detectable by the algorithm.

Fit to dipole dispersion model In our implemented code, we fit our dipole dispersion model in units of the normalized relativistic momentum, as these values are close to 1, compared to particle kinetic energies in J. We calculate the normalized relativistic momentum

$$\gamma\beta_{co}(x, y) = \sqrt{(\frac{E_{co}}{m_0 c^2} + 1)^2 - 1} \tag{4.1}$$

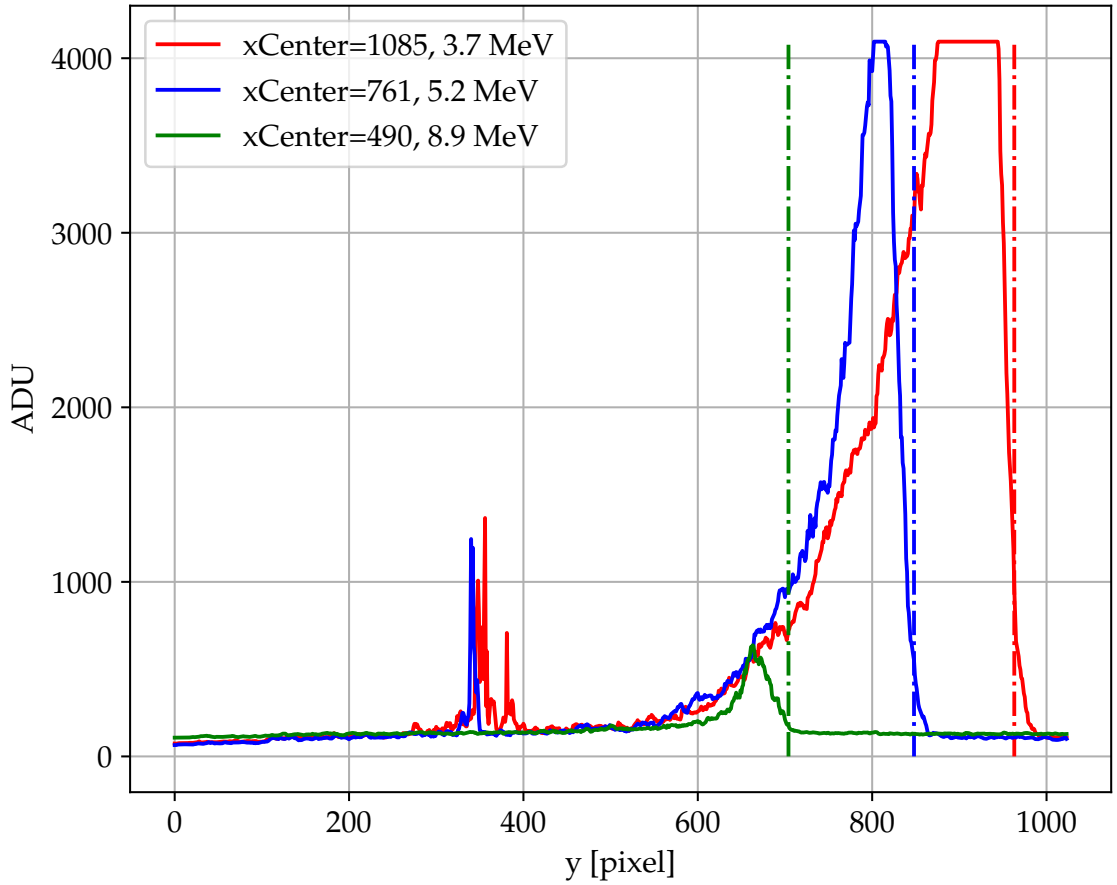

Figure 4.2: Solid lines as used in the signal edge detection algorithm for three different xCenters. Dash-dotted vertical lines are the largest y-coordinates with values over threshold, the detected signal edge.

and use our $\gamma\beta_{co}(x, y)$ as support points to fit the modeled dipole dispersion from equation (3.7):

$$\gamma\beta(x, y) = \frac{B_x(x)}{y + e} \cdot \zeta \tag{4.2}$$

The new fit parameter e in the equation allows for shifts in the setup along the y-axis. This function contains four more fit parameters in B_x (introduced in section 3.2). As we have five fit parameters we require at least five support points, which are best distributed as far as possible on the detector surface (example values for the fit parameters for the setup in CALA LION are noted in appendix B.4). With the determination of the fit parameters, this equation maps normalized momentum to each detector pixel. After the fit, we calculate the related kinetic energy for each pixel, and thus obtain a map of kinetic energy $E_0(x, y)$.

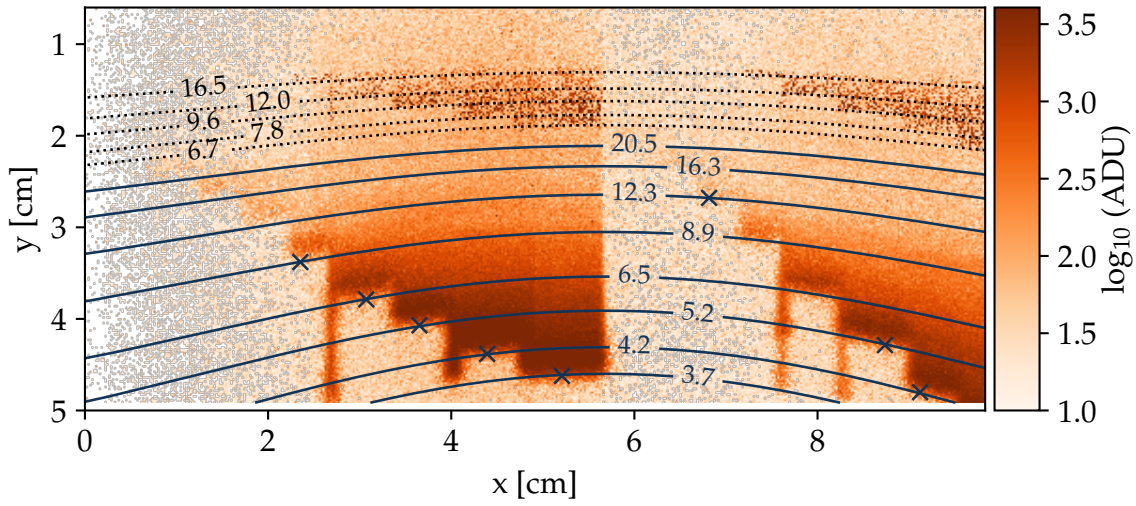

Figure 4.3: Equi-energy lines on a raw detector image. The 'x' mark support points, obtained by the edge detection method. Solid lines correspond to protons with kinetic energy E_{co}, dotted lines to carbon ions (C^6+) E_{co}. Each line has a number which corresponds to the kinetic energy E_0 in MeV/u.

By visual inspection of the fitted parameters, via the equi-energy lines, we have found that more than five support points which are distributed on the detector's active area result in best performance. The support points obtained for this work are marked as 'x' in figure 4.3. We have calculated equi-lines (figure 4.3 solid lines) corresponding to protons with kinetic energy E_{co} for each aluminum stripe of PABLONE. The lines show very good agreement of the fit to experimental data. We use the same dispersion model fit parameters that we have obtained from protons to calculate equi-energy lines for C^6+ ions (figure 4.3 dotted lines). They too show very good agreement between fitted data and E_{co} (for carbon).

Energy resolution The slit aperture in front of the dipole magnet has a width of 200 µm. The fan ion-beam emitted from the (almost) point-sized laser-driven source projects this width onto the detector. In section 3.4 we have introduced this projection. For CALA LION (distances noted in B.4) it is $y_{size} = 9$ pixel. Energies which end up closer than y_{size} to each other can not be resolved. This corresponds to an energy range, or energy bin. The smallest possible energy bins are calculated by dividing $E_0(x, y)$ along y-axis into 9 pixel segements. These have an upper E_{0up} and lower E_{0lo} kinetic energy boundary. We will refer to these bins by their center energy $E_0 = (E_{0up} + E_{0lo})/2$.

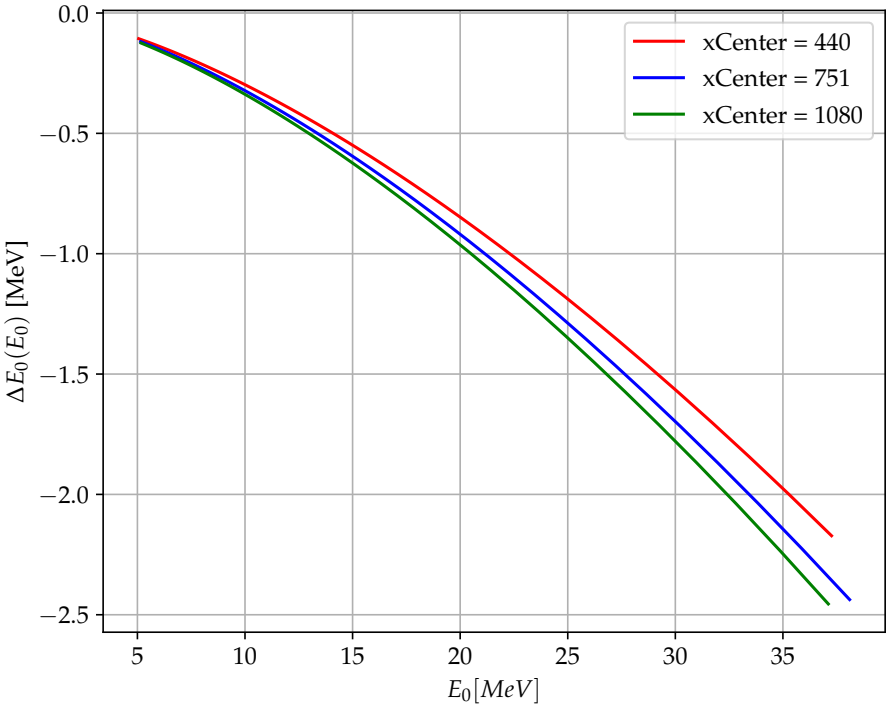

Figure 4.4: Detector energy resolution $\Delta E_0(E_0)$. The resolution changes along the x-axis due to the inhomogeneous dipole field.

Figure 4.4 shows the resulting energy bin size between two adjacent energy bins E_{01} and E_{02}, where we define $E_{02} > E_{01}$, and $\Delta E_0(E_0) = E_{01} - E_{02}$. The spacing between adjacent energy bins increases towards higher energies due to the decreasing dispersion by the dipole. ΔE_0 depends slightly on the x position, as the dipole field strength increases towards the edges.

Raw data histograms Macro-pixels or areas of mono-energetic irradiation are obtained by selecting $y_{size} = 9$ pixels along y-dimension (smallest energy bin), and thickness of an aluminum strip, typically $x_{size} = 61$ pixel along x-dimension. The boundaries of these areas follow the curvature of equi-energy lines, but do not subdivide pixels. These areas contain $9 \cdot 61 = 549$ pixels. We convert all pixel values into a histogram. These are our histograms of areas with mono-energetic irradiation at center kinetic energy E_0 and center x-coordinate xCenter. Figure 4.5a shows an example for protons with a kinetic energy of $E_0 = 9.1\,\text{MeV}$. The data exhibits distinct, equi-distant peaks. The peak at 65 ADU is mainly due to pixels which have not been hit by protons ($k = 0$). The peak at 100 ADU is due to the most probable energy loss of a single proton

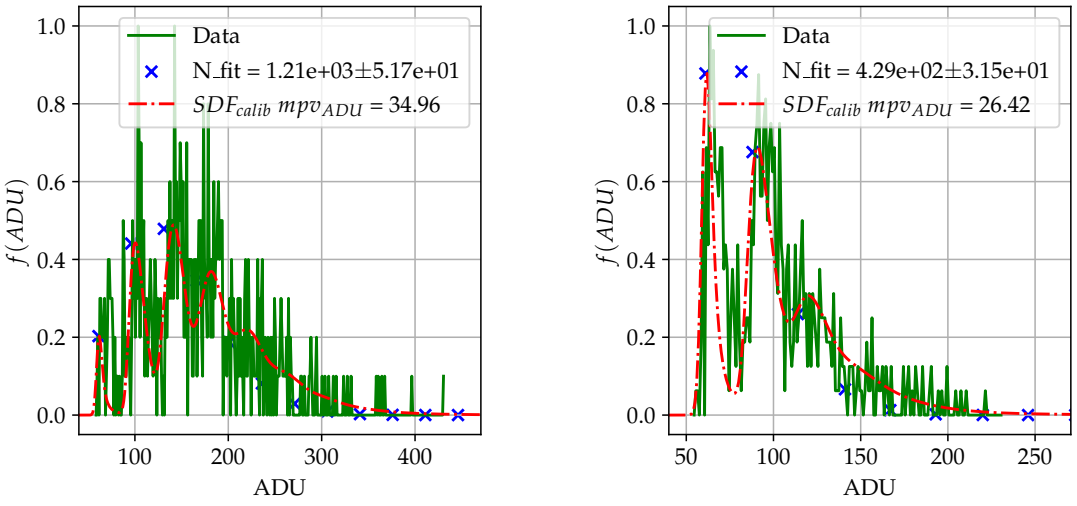

(a) $E_0 = 9.1\,\mathrm{MeV}$ (b) $E_0 = 10.3\,\mathrm{MeV}$

Figure 4.5: Histograms of areas with mono-energetic irradiation at xCenter=634. Green solid lines are data, normalized to peak. Dash-dotted lines are SDF_{calib} with respective mpv_{ADU} fitted to the data. Blue 'x' follow the binomial distributionwith fitted particle number N_{fit} for $n = 549$ pixels, and are spaced apart by $k \cdot mpv_{ADU}$.

hit ($k = 1$). The two and three proton hit contribution peaks are not spaced exactly at $k \cdot mpv_{ADU}$ and have a broader peak, $k > 4$ proton hits do not show clear peaks anymore. This is due to the increasing number of convolutions as defined in equation (3.24).

4.2 Calibration

For detector calibration we have to consider E_1, the kinetic energy of the particle as it enters the detector. The calibration routine pre-selects histograms to only those whose peaks can be identified by eye (to allow visual inspection of the fit later), such as the examples in figure 4.5. For the algorithm we make the following modifications to the SDF introduced in section 3.7.1. We shift the theoretically obtained energy loss distribution functions $f(\Delta)$ to have their most probable value at 0. We refer to the resulting convolutions as g'_k. We introduce the most probable background in detector units ADU as bg_{ADU}, and the most probable energy loss for a proton with kinetic energy E_1 in detector units ADU as mpv_{ADU}. The peaks in the histogram must then be at $\mathrm{ADU}(k) = bg_{ADU} + k \cdot mpv_{ADU}$ and the complete SDF used for calibration is

then:

$$SDF_{calib}(N, mpv_{ADU}, A, ADU) = A \cdot \sum_{k=0}^{\infty} B(k|p, N) \cdot g'_k(ADU + k \cdot mpv_{ADU}) \quad (4.3)$$

A is scaling the function to work best with data normalized to peak values.

Figure 4.5a shows the fit of SDF_{calib} (dash-dotted line) to histogram data (solid line) for $E_0 = 9.1\,\mathrm{MeV}$, yielding $mpv_{ADU} = 34.96$. Figure 4.5b, $E_0 = 10.3\,\mathrm{MeV}$, yields $mpv_{ADU} = 26.42$. We can see that the faster particles deposit less energy in the detector.

4.2.1 Proton Calibration

We have run the calibration routine over energy bins along four xCenters. The resulting mpv_{ADU} are plotted as blue 'x' in figure 4.6. The configurations will be referred to by their figure 4.6 inset names a), b), c) and d). Insets a) and c) are on detector element 2, insets b) and d) are on detector element 4. 292 µm thick aluminum is covering a) and b), 202 µm thick aluminum is covering c) and d).

Calibration with power law The range R_0 of protons impinging on the detector with a kinetic energy E_1 (in units of MeV) can be calculated using the continuously slowing down approximation (CSDA)[109]:

$$R_0 = \phi \cdot E_1^p \quad (4.4)$$

R_0 is in units of m, ϕ in $\mathrm{m\,MeV^{-}}^p$ and p is unitless. ϕ and p are material and ion-species dependent constants.

Consider a single 'representative' material (in our case the silicon layer of the detector) with ϕ and p. Then the energy as a function of depth z in the material is

$$E(E_1, z) = (\frac{\phi E_1^p - z}{\phi})^{1/p} \quad (4.5)$$

where E_1 is the representative particle energy for the mono energetic region after passage through the aluminum phantom. Then the energy loss in the active layer (with thickness d) Δ is:

$$\Delta(E_1, d) = E_1 - E(E_1, d) = E_1 - (\frac{\phi E_1^p - d}{\phi})^{1/p} \quad (4.6)$$

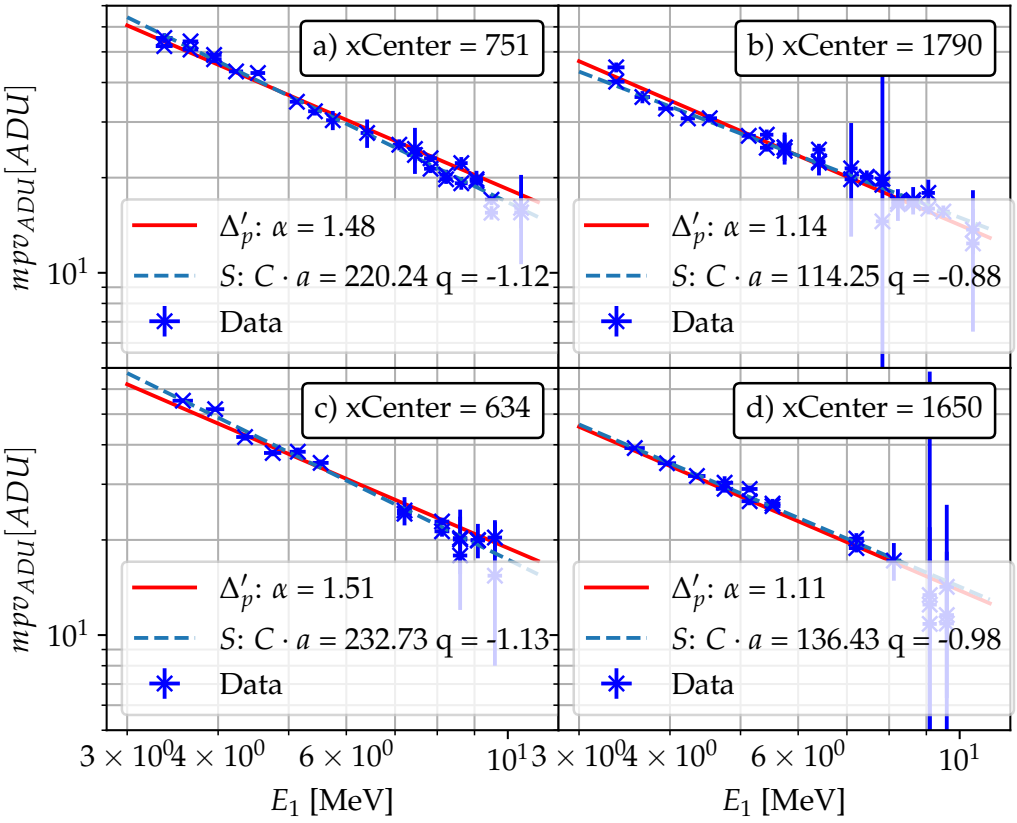

Figure 4.6: Detector calibration data from protons. Insets a) and b) are behind 202 µm, c) and d) behind 292 µm aluminum. Insets a) and c) correspond to a detector element on the left side, b) and d) to an element on the right side of the raw image (figure 4.1). Blue crosses are data from raw histograms. Red lines are $\Delta'_p = \alpha \cdot \Delta_p(Si, 2\,\mu m)$. α is the detector calibration in ADU/keV. The dashed blue line is the power law fit. Table 4.1 summarizes the fit parameters.

For small $d << \phi \cdot E_1^p$ a Taylor expansion to first order yields

$$\Delta(E_1, d) \approx \frac{d}{p\phi} \frac{E_1}{E_1^p} = \frac{d}{p\phi} E_1^{1-p} \tag{4.7}$$

which is a power law. The signal S is proportional to the energy loss and hence

$$S(E_1) = C \cdot a \cdot E_1^q \tag{4.8}$$

where $a = \frac{d}{p\phi}$ in units of MeV^p, $q = 1 - p$, and C is a proportionality constant in units of ADU/MeV. We see that a contains the detector thickness d and material and

particle specific constants p and ϕ, but we do not require distinct knowledge about these values to count particles. We fit this power law to our data. These fits are dashed lines in figure 4.6. The fit parameters are listed in table 4.1.

This is an important and interesting result. First, it shows that the analysis method yields a physically valid and reasonable result, because $\Delta_p(E_1)$ as fit parameter in the fit-method results in the expected power law (which can be noted also in figure 3.8). Second, the detector is now calibrated. Note that this procedure does not require knowledge of detector thickness d nor its exact material parameters p and ϕ. There is even no need to know the proportionality constant C separately. The considerable difference of $C \cdot a$ and q between detector elements underlines the importance to calibrate each detector element individually. Different aluminum thicknesses do not influence the calibration factors within error margins, because it depends solely on the number of charge pairs that are generated.

xCenter	Inset	Detector element	$C \cdot a$ [ADU/MeV^q]	q	α [ADU/keV]
751	a)	2	220.24 ± 9.84	-1.12 ± 0.03	1.48 ± 0.02
1790	b)	4	114.25 ± 4.62	-0.88 ± 0.02	1.14 ± 0.01
634	c)	2	232.73 ± 12.49	-1.13 ± 0.03	1.51 ± 0.03
1650	d)	4	136.43 ± 6.42	-0.98 ± 0.03	1.11 ± 0.02

Table 4.1: Proton calibration values for evaluated xCenters. Noted are fit errors of the respective fit parameter. Inset refers to figure 4.6.

Fit to Δ_p It is, however, still interesting to compare our calibration result with the MeV to ADU calibration measurement of S. Reinhardt [91]. There, it was assumed that $d = 2\,\mu\text{m}$ and the calibration factor was found to be 1.09 ± 0.12 ADU/keV. With equation (3.19) we introduce the calibration scaling factor:

$$\alpha = \frac{\Delta_p'}{\Delta_p}(Si, 2\mu m) \tag{4.9}$$

α for all insets in figure 4.6 are listed in table 4.1. From the difference between the α we obtained, we argue that the value obtained by Reinhardt [91] (who was using another detector element) is within expected fluctuations for the different detector elements. This shows that our result lies within the margins of the earlier calibration measurement and if calibration is required, it must be performed for each element individually.

4.2.2 Carbon Calibration

With the same argumentation we made for protons so far, we can extend our calibration to carbon ions as well. We use the carbon C^{6+} ion signal present in our data set, which is for example visible in figure 4.1. We calculated κ for our signal energy range to be in the Landau-Vavilov region (see figure 3.6). We use the extension of the energy map on our detector to C^{6+} to select areas of mono-energetic irradiation, as we did for protons.

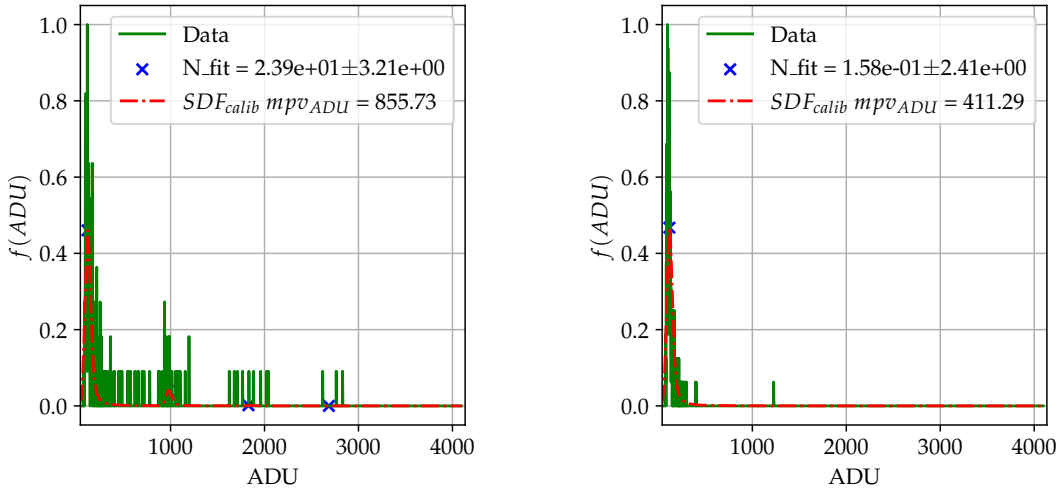

(a) $E_0 = 15.5\,\mathrm{MeV/u}$ (b) $E_0 = 26.7\,\mathrm{MeV/u}$

Figure 4.7: Carbon raw data histograms at xCenter=920. Inset a) does have prominent peaked energy loss, whereas the histogram in inset b) is background only.

Two example histograms of areas of mono-energetic irradiation for C^{6+} are presented in figure 4.7. Figure 4.7 a) is showing significantly larger energy loss per carbon ion compared to protons. Also, the statistics are significantly lower. However, a grouped structure is visible, peaks are $k = 1, 2, 3$ ion hits, respectively. We can estimate by eye that already the $k = 5$ peak, 5 carbon ions hitting a single pixel, would be expected at 4279 ADU and thus saturate the detector. Figure 4.7 b) is an example of a histogram of an area where no ion signal is present. We conclude three things from these examples. First, with lower statistics mpv_{ADU} is retrieved with reduced accuracy from a single histogram. Second, the low fluence will make it harder to retrieve actual particle numbers from a histogram. And third, the energy loss per particle is large compared to the extend of the background distribution. Thus, although this calibration suffers from inaccuracies, the differentiation between signal and no-signal in a histogram can be detected clearly. We are thus confident that our determination

yields the correct values of E_{max} for C^{6+}.

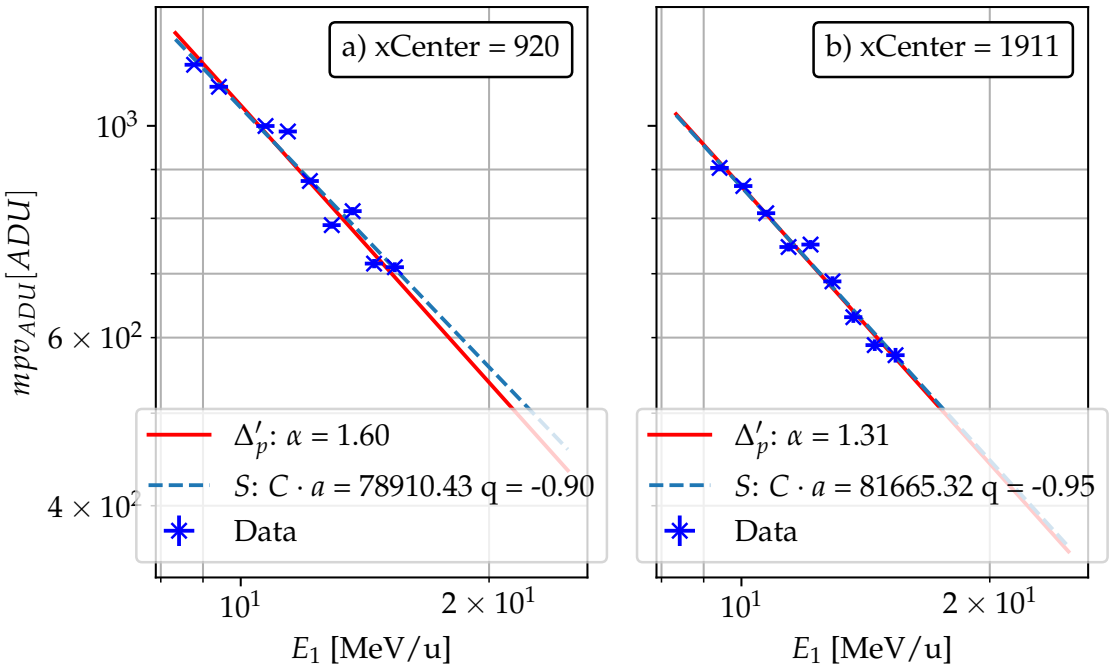

Figure 4.8: Detector calibration data for C^{6+}. Figures a) and b) are behind 142 µm aluminum, but on different detector elements. Blue crosses are data from raw histograms. Red lines are $\Delta'_p = \alpha \cdot \Delta_p(Si, 2\,\mu m)$. α is the detector calibration in ADU/keV. The dashed blue line is the power law fit. Table 4.2 summarizes the fit parameters.

xCenter	Inset	Detector element	$C \cdot a$ [ADU/MeV^q]	q	α [ADU/keV]
920	a)	2	78910.43 ± 25589.35	-0.90 ± 0.07	1.60 ± 0.02
1911	b)	4	81665.32 ± 19484.88	-0.95 ± 0.05	1.31 ± 0.01

Table 4.2: Overview of the calibration values for carbons. Noted are fit errors of the respective fit parameter. Inset refers to figure 4.8.

We fit SDF_{calib} functions to suitable histograms in our C^{6+} data set. The resulting data is shown in figure 4.8. Inset a) is data at xCenter = 920 pixel, b) is data at xCenter = 1911 pixel. These are two different RadEye1 detector elements, both covered by 142 µm thick aluminum. The 'x' are mpv_{ADU} at respective values of E_1. Their error bars are the mpv_{ADU} value errors from the fit routine.

We treat these points like we did for protons. From the power law fit (see table 4.2 for fit parameters), we clearly see the impact of the different particle species on $C \cdot a$ and q. However, by obtaining these, our detector is calibrated for carbon ions as well.

The fit of Δ'_p yields the values of α in table 4.2. These are not the same values within our error margins as for protons, but still very close. We again see the need to calibrate every detector element separately. Note that for carbons and for protons α of detector element 4 is smaller than for element 2.

The discrepancy of α values for protons and carbon ions may be reduced by assuming a different detector thickness. It is also possible that the energy map $E_{kin}(x, y)$ is not positioned correctly for carbons. Visual confirmation of the equi-energy lines for carbon does appear correct, however, carbons are dispersed significantly less then protons due to their larger mass. Small spatial inaccuracies in the energy grid, may result in an inaccurate relationship between E_1 and energy loss.

4.3 Background

The fit-method does not contain any prior subtraction of a background value or image - background is part of the SDF. Note that up to this point we have just defined a background distribution. In this section we will explain how we obtain it. We have found two main contributions to background, which can be obtained independently:

Empty shot contribution There is signal present even if the detector is being read-out without prior irradiation (by firing the laser without a target in place). This signal is also refered to as 'dark current' (see section 3.5). Data recorded under this condition is named 'empty shot'. The dark current contribution is always present, and thus leads to a fixed offset in the signal. Histograms of three areas (on the same detector element) of an empty shot are shown in figure 4.9 b). They all follow the same gaussian distribution with $mpv_{bg} = 58.7\,\mathrm{ADU}$ and $\sigma = 1.8$.

We have further plotted all empty shot acquisitions, which are made just before the signal data in SCR read-out mode, to show the temporal evolution of dark current (for SCR mode) over a complete beamtime in figure 4.10. This proves that empty-shot background is indeed stable.

On-beam contribution We have a complex background contribution that is only present with a laser-irradiated target, but is not due to the protons. This contribution is referred to as 'on-beam' or 'beam-induced' background. Example histograms, obtained from non-empty shots, are shown in figure 4.9 c). Only the 4 to 4.8 MeV and 100 to 400 MeV ranges overlap, and the 23 to 25 MeV region has a larger mpv_{bg} value,

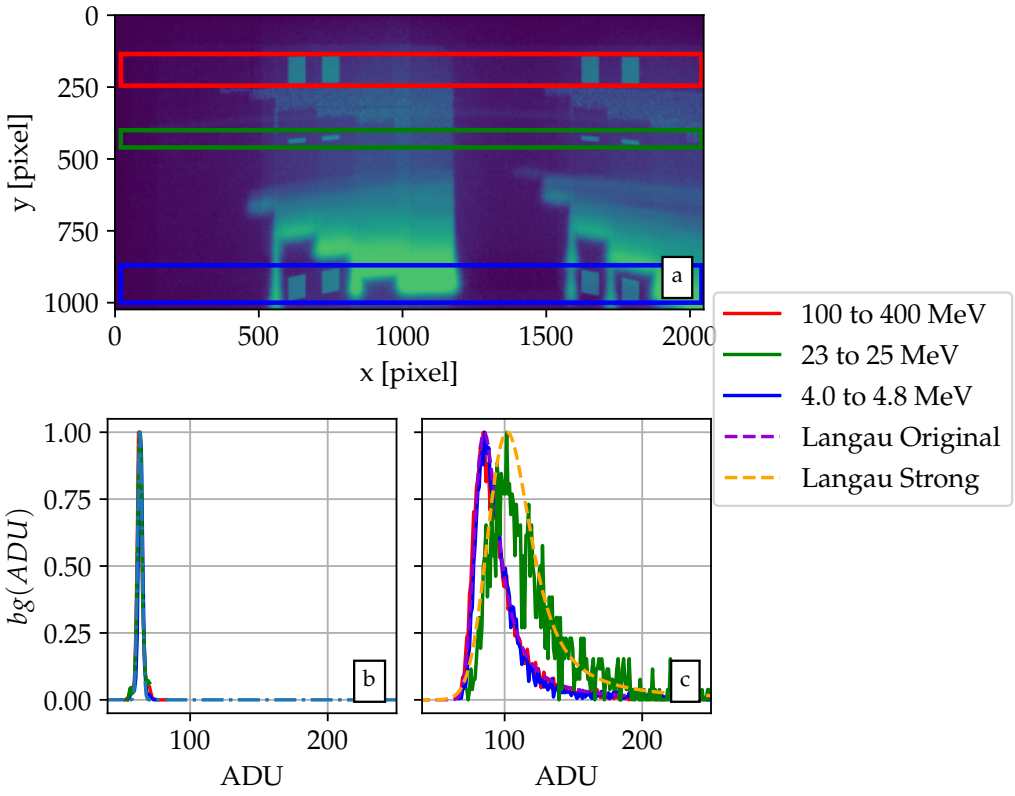

Figure 4.9: Background distributions at xCenter=1790. Solid lines are raw data histograms from regions where no proton signal is expected. An area above the signal corresponds to protons with kinetic energies between 100 and 400 MeV, an area below to 4-4.8MeV. a) is showing data from an empty shot where no laser-plasma interaction happened. b) is showing an empty shot readout at the same regions as c), which is showing the beam-induced background for a shot with good ion signal. The original idea of taking background is displayed by the 4-4.8 and 100-400 MeV signal, which is fitted by Langau Original. If the background is evaluated from the 23-25 MeV region, it is designated as 'Strong' background, which even may already include higher energetic proton signals.

and its distribution is broader. All distributions have an asymmetric shape, with a tail towards larger ADU values. mpv_{bg} is larger than for the empty shot histograms. A proton kinetic energy of at least 5.2 MeV is required to penetrate through 202 µm aluminum, and we expect less then 100 MeV from our laser-driven source. Originally we intended to use these regions on the detector as background, therefore we chose the 4 to 4.8 MeV and 100 to 400 MeV regions to be representative for the background. We refer to background obtained from these regions as 'original background'. As these two distributions are very similar, we concluded that background for the region in

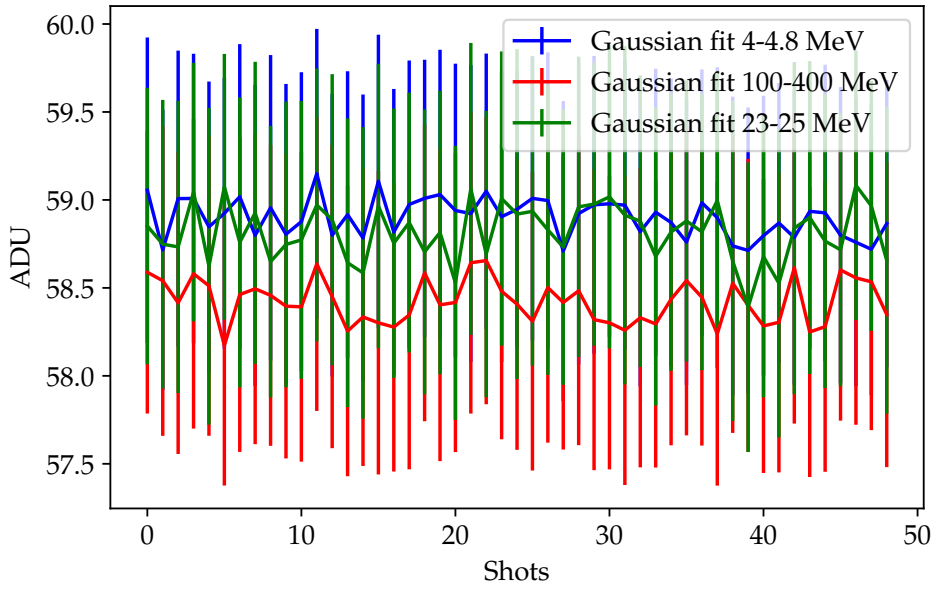

Figure 4.10: Temporal background evolution at xCenter = 634. Data points are values of mpv_{bg} of the Gaussian fit and error bars are determined by the corresponding σ. The data was evaluated for all background images recorded right before an actual shot image, therefore the first data points are at the beginning and the last ones from the end of the experiment. Histograms of the regions shown in figure 4.9 are fitted with a Gaussian.

between, the signal region, is similar as well. We have found by visual inspection that the shape of this background distribution matches a Landau distribution convoluted with a Gaussian distribution (we refer to this convolution as 'Langau', we have calculated these distributions using the `pylandau` package[108]). For the presented example fitting a Langau distribution yields $mpv_{ADU} = 85.1\,\text{ADU}$, $\eta = 4.7$ and $\sigma = 3.9$.

For reasons that will become clear at the end of this chapter, we have chosen a second region much closer to the expection proton signal, 23 to 25 MeV, as 'strong background' region. This shape, also shown in figure 4.9 c), has been fitted by a Langau distribution as well with the following fit values $mpv_{ADU} = 101.8\,\text{ADU}$, $\eta = 6.0$ and $\sigma = 10.6$. On-beam background increases for decreasing aluminum thickness, as shown exemplary in figure 4.11.

Therefore, background must be obtained for each aluminum thickness separately. And, due to the different response of each element, for each element as well. We have found that the on-beam background shape changes in between shots, but for the original backgrounds, mpv_{ADU} and shape are always very similar for both regions, whereas

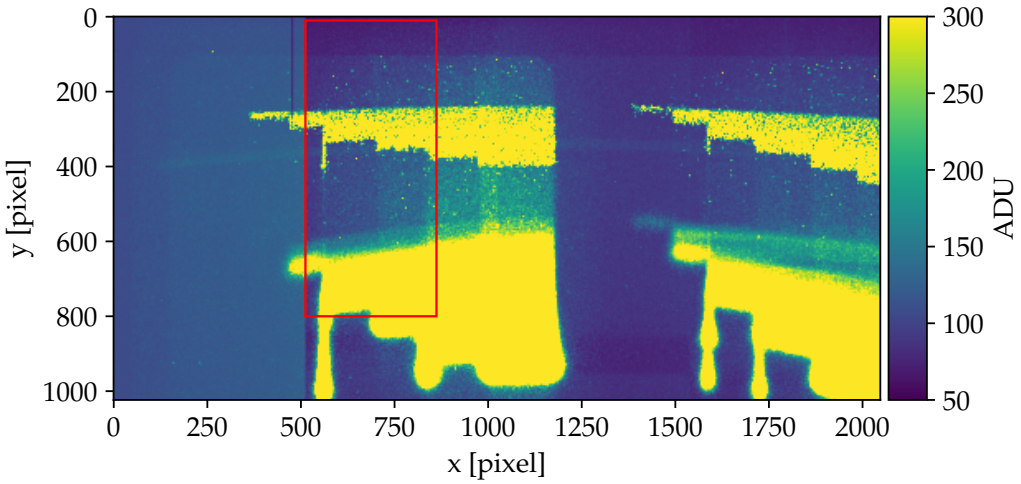

Figure 4.11: Radeye raw data with a reduced colormap to emphasize exemplary background. The detector housing is covering the active surface from y=0 to y=125. The signal at 125<y<250 is background, which is increasing from left to right. In between 400<y<500 the background is higher. Aluminum thickness is decreasing from 4.1 mm at x=0 to 112 µm at x≈1100, and similar for the right half of the detector. The borders of the four different detector modules are visible due to their different dark currents, especially from the far left one to the second at x=512.

strong background is always broader and has a larger mpv_{ADU}. Shots with similar ion performance have comparable background distributions. For larger maximum kinetic energies, the on-beam background distribution tends to be broader and centered around a higher ADU value. In the case of lower E_{max} and lower signal on the detector in general, it is narrower and closer to the empty-shot contribution.

The Langau fitted to on-beam background is $bg(ADU)$ in the SDF.

Slit up-down study A test has been carried out to study if the on-beam background changes with entrance slit aperture position (it is in front of the dipole magnet, see setup figure 3.4). The slit has been motorized with a linear stage to control its position along the chamber's y-axis (which is the height dimension). Visual comparison of consecutive shots with increasing slit position, see figure 4.12, gives inconclusive results. Of course the ion signal shifts as expected for this setup for a point-like source, but no obvious change of the background contribution was observed when moving the slit.

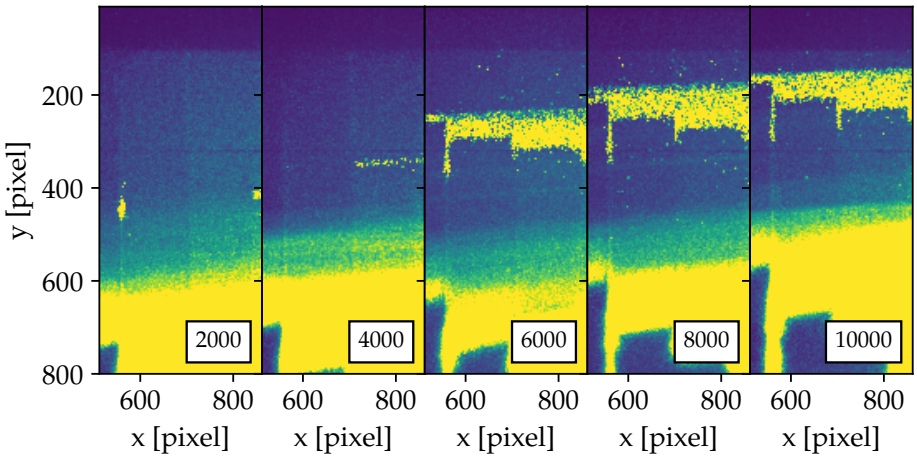

Figure 4.12: Raw data of slit up-down study. The insets are showing the area marked in red from figure 4.11. Each inset is corresponding to a shot with a different slit position. The inset number is referring to its linear stage motor position, which is the slit height. 4000 has been the standard value. The signal strength varies over the different shots, but its signature does move upwards whereas no change beyond expected shot-to-shot fluctuations in the background is obvious.

The shot-to-shot fluctuations may very well explain the small difference in background strength for the different images.

Thus, we conclude that the on-beam background is not originating from charged particles travelling from the source through the dipole field onto the detector. X-rays from the target are also unlikely, because they would not be deflected in the magnetic field and one would observe a projection of the slit onto the detector. However, electrons emitted from the laser-plasma interaction are large in number and are distributed over a broad energy range extending well above MeV. These electrons enter the dipole field through the slit and are deflected upwards. For energies $< 0.5\,\mathrm{MeV}$ they can even turn by 180° in the 0.2 T field of this magnet [94]. Then they hit the dipole iron yoke, or the inside of the slit. These impacts can generate bremsstrahlung that might be sufficiently energetic to penetrate the aluminum phantom in front of the detector. A more detailed study would be most interesting.

Electron hole pairs With equation (3.13) we can calculate the number of electron-hole pairs per ADU for $\alpha = 1.5\,\mathrm{ADU/keV}$ to be $n_{pairs} = \frac{E}{E_i} = \frac{10^3 eV}{1.5 \cdot 3.6 eV\,ADU} \approx 185\,/\mathrm{ADU}$, for $\alpha = 1.1\,\mathrm{ADU/keV}$: $n_{pairs} \approx 253\,/\mathrm{ADU}$. With this we can calculate the number of dark current electron-hole pairs per second: The empty shot mean dark current of the left detector element in figure 4.9 is 58.7 ADU, obtained from a constant read out at 0.5 Hz. This yields ≈ 21700 pairs at 185 /ADU. The empty shot mean dark current for the right detector relement is 63.3 ADU which results in ≈ 32000 pairs at 253 /ADU flowing per second. This is much larger than the 4000 electrons per second obtained at room temperature [95]. Figure 6 in [95] provides the dark current as a function of temperature and 30000 electrons per second correspond to 45 ℃. However, this value should be seen with caution, as this paper does not report on differences between detector elements, but the order of magnitude might remain the same. However, cooling the detector elements may reduce the dark current significantly, and has helped with CCD cameras in vacuum [60].

4.4 SDF for Particle Number Retrieval

For particle number retrieval, we modify SDF_{calib} slightly to include our calibration. mpv_{ADU} has been determined in section 4.2. Thus we only have two remaining fit parameters, particle number N and function height scaling A:

$$SDF_{eval}(N, A, ADU) = A \cdot \sum_{k=0}^{\infty} B(k|p, N) \cdot g'_k(ADU + k \cdot mpv_{ADU}) \tag{4.10}$$

The particle number retrieval routine then follows these steps for a selected xCenter: We first retrieve on-beam background distributions $bg(ADU)$. We obtain raw data histograms of all areas of mono-energetic irradiation for our evaluation kinetic energy range. For protons, this is $6 < E_0 < 30$ MeV, for carbon ions $10 < E_0 < 30$ MeV/u. These each span a kinetic energy range of $E_{0range} = E_{0up} - E_{0lo}$.

Then we fit SDF_{eval} functions to each histogram, which yields the fitted particle number for this histogram N_{fit}.

With these, we can obtain the differential energy spectrum (see section 3.4). $N_{fit} = dN$ and $E_{0range} = dE_{kin}$. The solid angle $\Delta\Omega$ is calculated from the respective projections onto the detector $y_{size} = 9$ pixel, $x_{size} = 62$ pixel (the width of an aluminum phantom stripe). For our data, $z_1 = 83\,\mathrm{cm}$, $z_m = 12\,\mathrm{cm}$ and $z_d = 68.2\,\mathrm{cm}$. With this, we can generate a differential energy spectrum for a single shot for each calibrated

xCenter position on the detector.

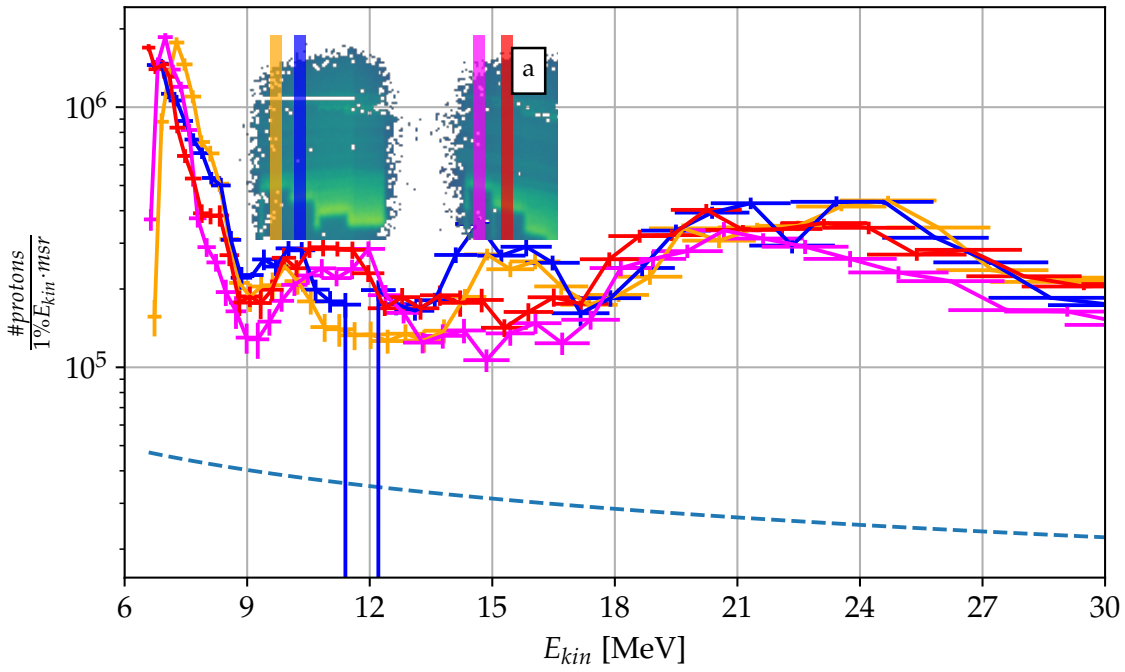

Figure 4.13: Proton differential energy spectrum obtained from shot 103, using 'Original Background'. The dashed line corresponds to 50 protons, the noise threshold. Raw data (inset a) is indicating an $E_{max} \approx < 12\,\text{MeV}$. The 4 solid lines are spectra evaluated at the marked areas of the same color in inset a). The evaluation claims $E_{max} > 30\,\text{MeV}$.

Figure 4.13 is an example differential energy spectrum obtained from the above described procedure, where we have used the 'Original Background'. Proton numbers have been evaluated in four different regions on the detector. Two of them are behind 202 µm, the other two behind 292 µm thick aluminum, and each thickness is represented on both evaluated detector elements. 'xCenter' is their respective pixel x-coordinate for reference. From the investigation with artificial histograms in section 3.7.2 we have deduced that the QIS method requires at least 50 protons per mono-energetic region. The raw data inset, figure 4.13 a), shows data from the detector, from which a proton $E_{max} = 8.9\,\text{MeV}$ can be infered by visual inspection.

In contrast, the evaluated spectra with the QIS method, however, do extend up to the last evaluated energy bin at 30 MeV with significant particle numbers. Also, we have never observed energies above 23 MeV, even when employing alternate methods and focusing with permanent quadrupole doublets and RCF film stacks. We therefore

conclude that the background approach described so far is not including all contributions and has to be refined. The raw data in figure 4.13 a) also indicates that there may be more background in the center region of the detector. We have therefore decided to change the region where the background is obtained to an area much closer to, and maybe even overlapping the expected signal area, namely the 23-25 MeV proton region, which we have already introduced as 'strong background'. This is not a perfect solution as it relies on visually choosing the maximum proton energy from the raw signal. On the other hand, most (if not all) other methods determine the maximum energy just in this way.

The strong background has been used as $bg(ADU)$ for the following evaluations. Compared to the original approach, the evaluated spectra then drop into the noise floor approximately at energies that are in agreement with the visual inspection of the data. The proton numbers obtained with this background approach are likely underestimating the actual numbers.

Chapter 5

Ion Beams at CALA LION

In this chapter, we use the QIS method to quantifiy the ion beam performance of the laser-driven ion source. We show exemplary data of distinct experimental results in more detail, and present an application. Particle energies in this chapter are kinetic energies E_0 unless noted otherwise.

5.1 Source Monitoring

We have evaluated 42 shots from a beamtime at CALA LION on 12th of May 2021. The setup of this study is shown in figure 5.1. On this day, the following laser parameters were available: Laser-pulse energy (on target) up to $E_L = 9.9\,\mathrm{J}$, laser-pulse width (measured with FROG) $\tau_L = 32\,\mathrm{fs}$ (laser contrast measured prior to this campaign is shown in figure 3.1). The focal spot had been optimized with DM3, the focal spot diameter was $d_{FHWM} = 4.9\,\mu\mathrm{m}$. The laser-peak intensity has been $I_L = 1 \cdot 10^{21}$ $\mathrm{W\,cm^{-2}}$ (calculation see C). We prepared 10 target holders with 400 nm and 9 holders with 600 nm thick plastic (Formvar) foils. We have recorded images of backscattered (Screen 1) and transmitted light (Screen 2). The WASP was set up with the following

xCenter [px]	θ [°]	Color	Ion
634	-0.90	orange	H^+
751	-0.70	blue	H^+
920	-0.42	gray	C^{6+}
1650	0.81	magenta	H^+
1790	1.05	red	H^+
1991	1.39	black	C^{6+}

Table 5.1: List of detector evaluation stripes' angles to target normal.

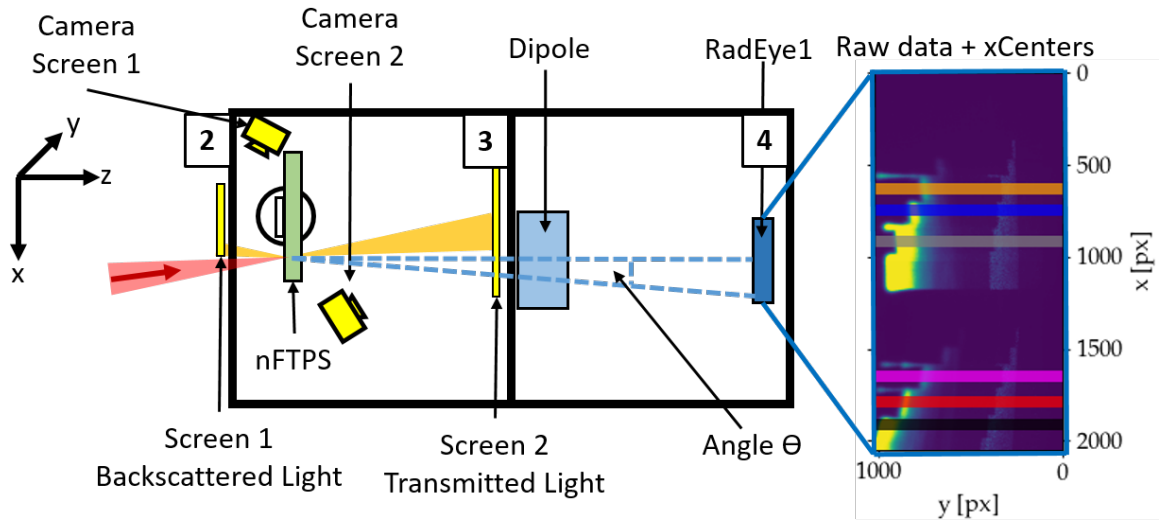

Figure 5.1: Source monitoring study with WASP. An incident laser (red) accelerates ions from targets in the nFTPS. From the laser-plasma interaction, light is backscattered onto 'Screen 1' and transmitted on 'Screen 2', which are monitored by cameras. Accelerated ions drift through the WASP and hit the RadEye1 detector. The RadEye1 raw image shows the position of evaluated stripes at respective xCenters, which are color-coded throughout the following figures. The angle between xCenter and target normal θ is in the x-z plane.

distances $z_1 = 85\,\text{cm}$, $z_m = 10\,\text{cm}$ and $z_d = 68.2\,\text{cm}$ (see figure 3.4). We have used a fresh set of RadEye1 detector elements, and operated the system in SCR mode (see Appendix A.1). The detector elements had been covered by the aluminum phantom PABLONE (as described in table 3.1).

We have analyzed ion spectra at six different x-positions on the detector. Four xCenters have been evaluated for protons within an angle to target normal ranging from θ =-0.90° to +1.05°. Two xCenters have been evaluated for C^{6+} within an angle to target normal ranging from θ =-0.42° to +1.39°. We have color coded the evaluation angles in the following plots, table 5.1 summarizes this coding. For each stripe (angle), we can extract the maximum energy E_{max} and particle number per energy and cone angle.

In figure 5.2 proton numbers per $1\%E_{kin}$ and msr are plotted for energies of 12 MeV (circle), 15 MeV (triangle) and 18 MeV (square) for 27 shots. A carbon ion signal has not been present on all shots of this series, therefore we only discuss proton kinetic energies and related particle numbers in the following. Dark green lines are per shot averages over all solid angles for 12 MeV (solid line, circles), 15 MeV (dash-dotted line, triangles) and 18 (MeV dotted line, square). The 27 shots are all from 12th of

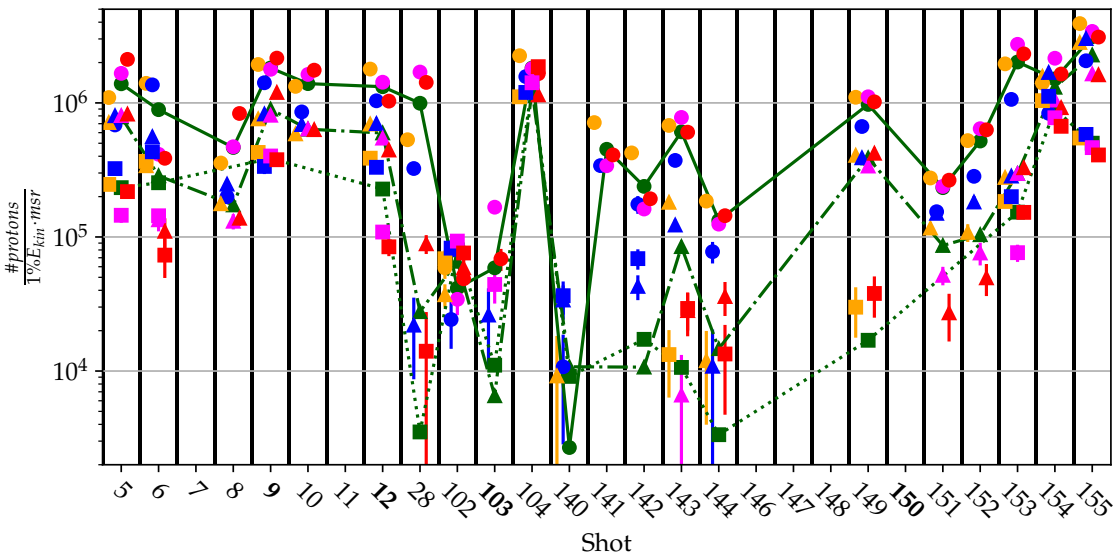

Figure 5.2: Proton source monitoring at three energies for 27 shots. $E_L = 9.9\,\mathrm{J}$, plastic targets with 400 or 600 nm thickness. Proton number is given at four different xCenters (colors) for 12 MeV (circle), 15 MeV (triangle) and 18 MeV (square). Green lines represent angle-averaged values for 12 MeV (dotted), 15 MeV (dash-dotted) and 18 MeV (solid). Figure 5.3 shows spectra of bold shot numbers in more detail. Data from 12th of May 2021.

May 2021 and all shots had $E_L = 9.9\,\mathrm{J}$ on target. Plastic targets with 400 or 600 nm thickness have been used.

Let us take a closer look at particle numbers for shot 9 and 149 which are exemplary for the angular particle number fluctuation: For shot 9 the particle number at 12 MeV (circles) vary between $1.4 \cdot 10^6 \frac{\#protons}{1\%E_{kin}\cdot msr}$ (blue) and $2.1 \cdot 10^6 \frac{\#protons}{1\%E_{kin}\cdot msr}$ (red), thus, by a factor of 1.5. The particle number at 15 MeV (triangles) is lower and has a similar variety over angle, ranging from $7.5 \cdot 10^5 \frac{\#protons}{1\%E_{kin}\cdot msr}$ (orange) to $1.2 \cdot 10^6 \frac{\#protons}{1\%E_{kin}\cdot msr}$ (red), variation is within a factor of 1.6 and at 18 MeV (squares) numbers vary between $3.4 \cdot 10^5 \frac{\#protons}{1\%E_{kin}\cdot msr}$ (blue) and $4.2 \cdot 10^5 \frac{\#protons}{1\%E_{kin}\cdot msr}$ (orange), this yields a factor of 1.2. For shot 149 the particle number at 12 MeV (circles) is between $6.7 \cdot 10^5 \frac{\#protons}{1\%E_{kin}\cdot msr}$ (blue) and $1.1 \cdot 10^6 \frac{\#protons}{1\%E_{kin}\cdot msr}$ (magenta). The particle number at 15 MeV (triangles) is lower, ranging from $3.4 \cdot 10^5 \frac{\#protons}{1\%E_{kin}\cdot msr}$ (magenta) to $4.2 \cdot 10^5 \frac{\#protons}{1\%E_{kin}\cdot msr}$ (red). At 18 MeV (squares) the number ranges from 0 (blue, magenta) to $3.8 \cdot 10^5 \frac{\#protons}{1\%E_{kin}\cdot msr}$ (red). Thus, if particles have been detected, the angular particle number fluctuation is a factor of ≈ 2.

Shot 9 is an example for low, and shot 149 for large angular distribution. To guide

the eye over several shots, the mean over all evaluated angles has been calculated for each shot and plotted for the three chosen energy values (12, 15, 18 MeV) as dark-green lines in figure 5.2. In the following, we investigate the minimum and maximum particle numbers of this 'angular mean' for the presented shots. For shots 7, 11, 146, 147, 148 and 150 $E_{max} < 12$ MeV, therefore their particle number is zero. In the following we want to consider only shots with $E_{max} > 12$ MeV. Among these selected shots, the proton numbers vary between $3.3 \cdot 10^3$ and $10^7 \frac{\#protons}{1\% E_{kin} \cdot msr}$.

This shows that if we exclude all shots with $E_{max} < 12$ MeV we still have particle number deviations in the range of three orders of magnitude for the investigated energies 12, 15 and 18 MeV, but for most shots, the numbers are smaller the higher the evaluated energy, i.e. the spectrum monotonically decreases.

This is observed for most of the presented shots and is expected from our laser-driven source. An exception is shot 104, which exhibits a very flat spectrum from 12 to 18 MeV, or shot 103, where the particle number at 12 MeV is lower than at 15 MeV.

Finally, consider the occurence of particles at a certain angle for the example energies 12, 15 or 18 MeV. In figure 5.2 we find 21 shots with $E_{max} > 12$ MeV, and we have evaluated 4 angles per shot, thus a total of 84 evaluated angles. $E_{max} > 12$ MeV has been detected on 79 of these, $E_{max} > 15$ MeV on 69 angles and $E_{max} > 18$ MeV on 45 angles. This shows qualitatively that the reliability of the proton yield increases with decreasing energy demand.

Example proton spectra

Figure 5.3 shows four exemplary shots of this beamtime. The figure contains differential energy spectra for protons and carbon ions for the evaluated energy range from 6 to 30 MeV/u. We used the QIS-Method for particle number evaluation. For protons, we employed the 'strong background' and therefore signals are expected to dip into noise at E_0 >23 MeV. The method still yields outliers in the energy range beyond 23 MeV, which we do not consider as signal. For carbon ions we used the 'original background'. Two laser-plasma light diagnostics are shown for each shot as well. Screen 1 represents light that has been reflected from the target surface, Screen 2 contains light that has been transmitted through the laser-plasma interaction. For a perfect reflection at the target surface we expect a vertical beam diameter of 5 cm at Screen 1, for a perfect transmission we expect a beam diameter of 13 cm at Screen 2. Note that the carbon ion signal at $E_0 < 11$ MeV/u is often saturated. Saturated regions have not been evaluated, and thus do not appear as data points in these plots. If we

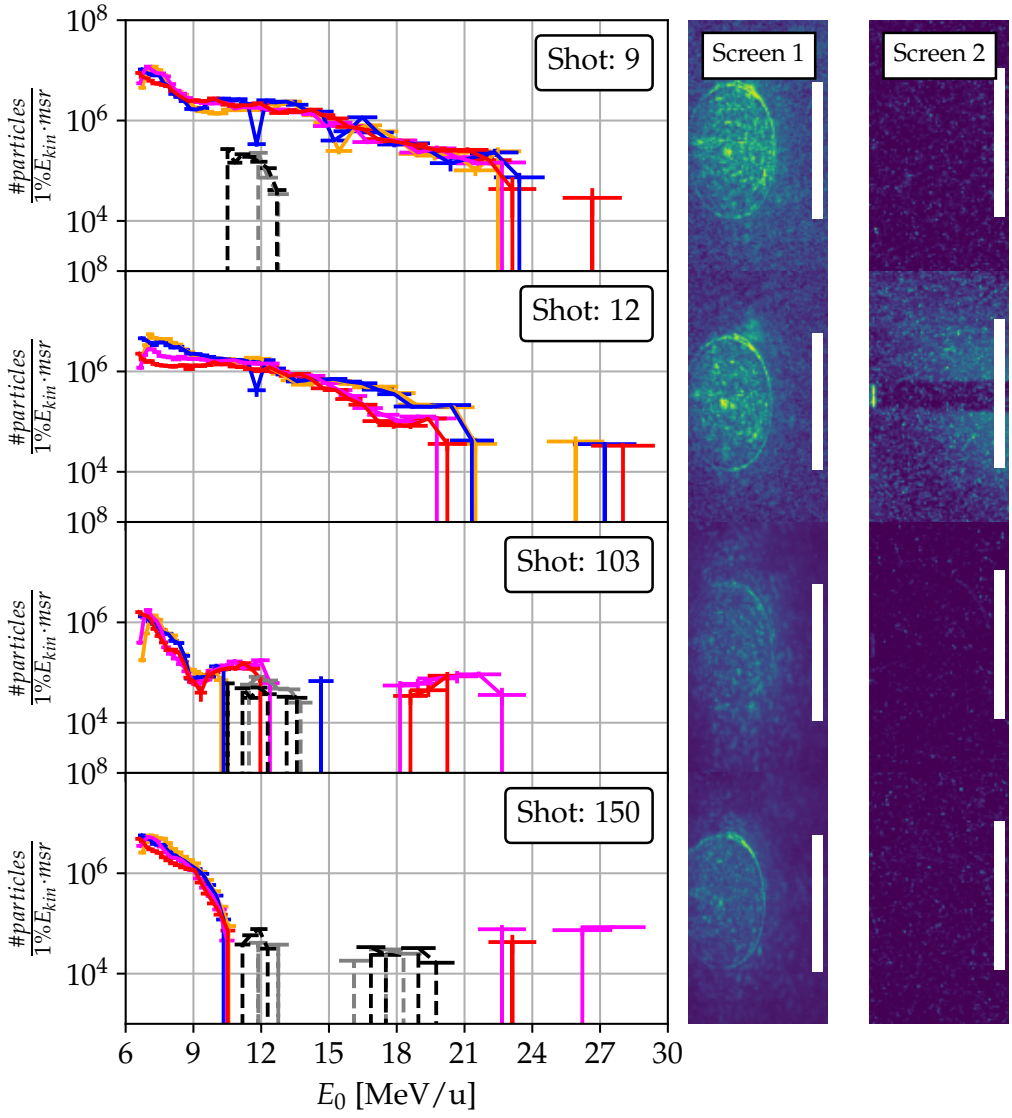

Figure 5.3: Proton and carbon spectra from 12th of May 2021. Note: Saturated carbon signal areas (typically at $E_0 < 11$ MeV/u) do not appear in this plot. Screen 1 shows reflected, Screen 2 transmitted light. The white bars show the expected vertical beam diameter for perfect reflection (Screen 1, 5 cm) or transmission (Screen 2, 13 cm).

talk about particle numbers in the following, we will drop units of $\frac{\#particles}{1\%E_{kin}\cdot msr}$, for the sake of simplified reading.

Shot 9 The proton spectrum decays exponentially from $8 \cdot 10^6$ particles at 7 MeV to its $E_{max} = 23$ MeV. At 11.5 MeV blue detects only $3.6 \cdot 10^5$ particles, whereas the other three evaluation stripes detect $2 \cdot 1e6$ particles. A similar deviation happens at 15.5 MeV of lowest $2.4 \cdot 10^5$ particles (orange) compared to $1.1 \cdot 10^6$ particles (red). Within these deviations, this spectrum is independent of angle. The carbon spectrum decays exponentially as well, from $2.2 \cdot 10^5$ at 10 MeV/u to its $E_{max} = 12.8$ MeV/u. However, except for these outliers at specific proton energies, particle numbers are within a factor of two constant. We refer to this again as constant over solid angle. The reflected light on Screen 1 shows a distinct ring structure with a bright spot in the center. Screen 2 shows no visible transmitted light.

Shot 12 For protons, the particle number at 7 MeV ranges from $1.5 \cdot 10^5$ to $5 \cdot 10^5$. At 10 MeV the particle number difference is smaller than a factor of two. From 14 MeV towards larger E_0, orange and blue ($\theta < 0$) and red and magenta ($\theta > 0$) differ, for example between 10^5 and $4 \cdot 10^5$ at 17 MeV. For this shot E_{max} has angular dependence, as $E_{max} = 20$ MeV for $\theta > 0$ and $E_{max} = 21.5$ MeV at $\theta < 0$. This shot shows also no carbon signal. On Screen 1 we see a distinct ring structure with a bright spot in the center. Screen 2 shows transmitted light, but with no distinct profile.

Shot 103 The proton spectra from this shot are exponentially decaying from 10^6 particles at 7 MeV, to $5.8 \cdot 10^5$ particles at 9.5 MeV, followed by a plateau at $1.2 \cdot 10^5$ particles up to $E_0 = 10.5$ MeV for $\theta < 0$. In the blue spectrum ($\theta = -0.7°$), we observe a single data point at $E_{max} = 14.6$ MeV. For $\theta > 0$, $E_{max} = 23$ MeV with no signal between 12.7 and 18.5 MeV is visible. The carbon spectrum exhibits a slight drop from 10.6 MeV/u and $6.5 \cdot 10^4$ particles to $E_{max} = 13.7$ MeV/u and $2.3 \cdot 10^4$ particles. In Screen 1 the outer ring feature that was visible in shot 9 and 12 is barely visible and there is no bright spot in the center. Screen 2 shows no visible transmission.

Shot 150 The proton spectra are similar over solid angle and decay from $4 \cdot 10^6$ particles at 7 MeV to $E_{max} = 10.4$ MeV. Carbons are detected between 11.6 and 12.2 MeV/u, and between 16 and 19 MeV/u. Screen 1 shows a sharp outer ring structure, and a small and bright central dot. Screen 2 shows no visible transmission.

Discussion These examples show that the particle numbers deviated along the measured angle at all energies. There is a trend that for protons with $E_0 < 10$ MeV the spectra are more uniform than at larger kinetic energies, and are within one order of

magnitude at 7 MeV. Carbon ion numbers are within a factor of 3 over the evaluated kinetic energy range. E_{max} strongly depends on the solid angle. Interpreting the images of Screen 1 and Screen 2 is difficult. The presence or absence of features in Screen 1, such as the bright center spot and its relation to ion spectra is interesting and might give further insights in future studies.

5.2 Proton Focus

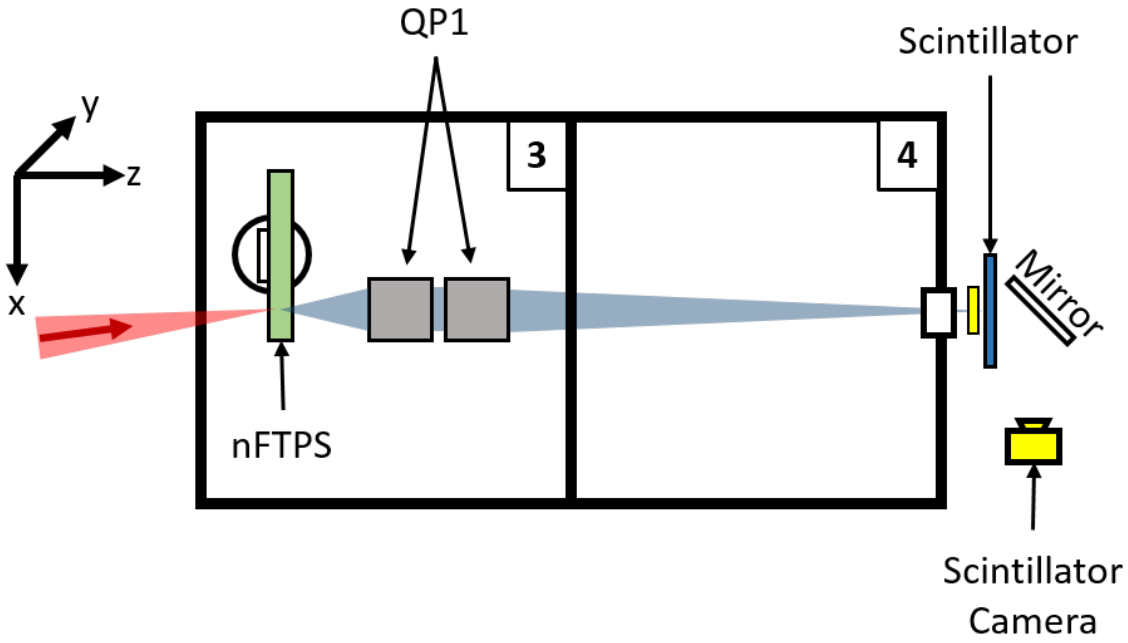

Figure 5.4: Setup quadrupole focus.

The permanent quadrupole (QP) doublet in CALA LION has been investigated in great detail in the work of Rösch [62]. Figure 5.4 shows the setup used to record proton foci. The quadrupole doublet has been positioned to focus a design energy, in our case 12 MeV, to a spot on a scintillator 1.8 m downstream of the source. Protons leave the vacuum chamber through a 50 µm thick Kapton window. An additional 12 µm thick aluminum foil blocks stray laser light leaking through the Kapton window and is taped to the vacuum exit window. A camera is monitoring the scintillator via a 45° mirror. Additional information can be found in [62].

Figure 5.5 shows scintillator images of 12 consecutive shots from 22nd of October 2021. The design energy has been $E_0 = 12$ MeV, which is the lowest due to physical

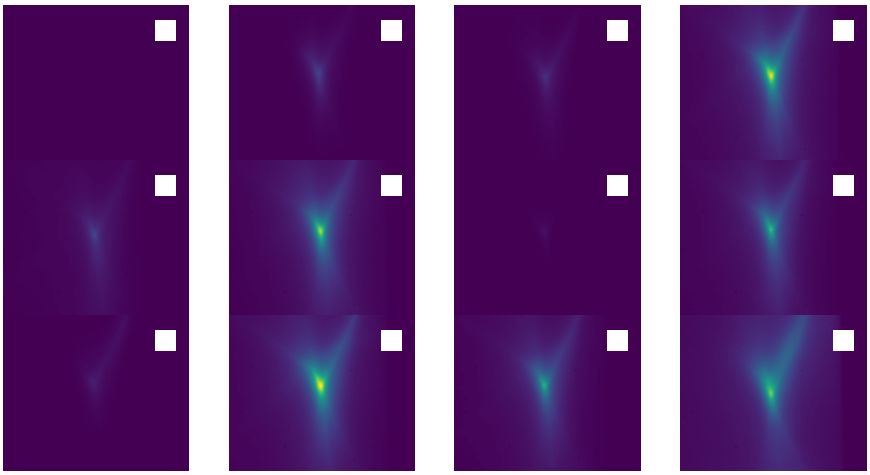

Figure 5.5: Scintillator images of 12 consecutive proton foci. Design energy has been $E_0 = 12\,\mathrm{MeV}$. The white square has 1 mm side length.

constraints of the setup. The scintillation is dependent on the number of incident protons. The impact of the shot-to-shot fluctuations from the source is clearly visible. The sum over all pixels, after a background image has been subtracted, will be our 'brightness'. The darkest image has a brightness of $1.7 \cdot 10^8$, and the brightest image of $1.6 \cdot 10^9$, which is one order of magnitude difference. This fluctuation is likely related to the yield fluctuation reported in figure 5.1.

Although the QP focus shape in figure 5.5 does not change notably, there are fluctuations in the brightness distribution, thus proton number distribution, of the foci. The QP have an opening angle of $\pm 0.86°$ in the x-z plane, which is comparable to our WASP opening angle θ that ranges from $-0.9°$ to $1.05°$. We have discussed in the previous section that the WASP measurements indicate increasing angular particle number spread with larger kinetic energy. Thus we know that the QP proton focus shape will fluctuate more towards increasing design energies.

Chapter 6

Summary, Perspectives, Closing Remarks

6.1 Summary

This work documents the establishment of the laser-driven ion source at the Centre for Advanced Laser Applications, in particular the technological challenges that were successively tackled.

The integration of a composite water-concrete beamdump eliminated the necessity of personal dosimeters for laboratory personnel, and was an important step towards the acceleration operation permit for LION. The laser upgrade to ATLAS 3000 contained two major improvements. Adding additional amplifier stages increased maximum laser-pulse energy and replacing the REGEN amplifier stage eliminated two pre-pulses that have been detrimental to laser-driven ion acceleration. The LBD hard- and software has been tested and improved to transport laser pulses to the EBL with a user friendly interface. The LBD contains a large aperture deformable mirror which is used to optimize the laser focus in the experiment. Thorough tests at the ZS ensured that it was working properly before first accelerator operation.

The LION EBL vacuum chamber setup currently uses an OAP with focal length of 1.5 m and produces a very good laser focus that enabled first ion acceleration experiments, with proton kinetic energies of up to 23 MeV. The automation of the nFTPS has been significantly increased with new control software which includes a better TANGO system integration. The redesign with a plastic wheel and magnetic mounting of target holders with increased hole size has increased usability and reduced target collateral damage. Light transmitted (A.2) through the laser-plasma and light

reflected (A.3) has been monitored with a screen and camera each. This allowed to have two permanently installed non-invasive diagnostics that can yield complementary information on the laser-plasma interaction in the future. The permanent quadrupole doublet for transporting proton bunches to the application platform on air has been integrated and yielded first results. A wide-angle-spectrometer allowed to analyze ion spectra over a spatial angle $\approx \pm 1^\circ$ degree in the x-z plane. The aluminum phantom PABLONE enables now inferring the maximum proton energy and the presence of carbon ions by visual inspection of raw data directly after the shot. A model of magnetic dipole dispersion has been derived, and fitted to support points on a raw data image, creating an energy map on the detector without the need of exact knowledge of the magnetic field distribution and particle tracking.

It was demonstrated that histograms of signal values in areas of mono-energetic irradiation can be used to calibrate the detector for protons and carbon ions without requiring prior knowledge of the detector thickness or detector response (a similar approach can also be used to calibrate microchannel plate detectors to gold ions [110]). Based on the most-probable energy loss theory, we have derived a response factor for two separate detector elements with two particle species and found between 1.11 and 1.60 ADU/keV, in good agreement with the previously obtained calibration factor 1.09 ADU/keV. We have also found that calibration is required for each element separately.

The theory of energy loss distributions in thin layers provides the basics for the signal distribution function and is convoluted with a binomial distribution to account for multiple hits per pixel. This SDF models our histograms well, and is fitted with only two fit parameters: a height scale and particle number. A study with simulated raw data yielded that this method works best if the particle number is between one tenth and ten times the number of pixels in the evaluated macro pixel. We have explained two separate sources of background and how we treat those during evaluation. This novel evaluation method yields the quantitative ion spectra (QIS).

For a data set of 42 shots, we have extracted particle numbers at three different kinetic energies and four solid angles for protons. The particle numbers are fluctuating, but the general trend is that particle numbers at lower energies are larger and fluctuate less. However, we identified significant fluctuations in particle number and maximum energies over small angles. These observations are described on the basis of the proton and carbon spectra obtained in four exemplary shots. The angular fluctuations likely impact the QP proton focal shape (see 5.2).

6.2 Perspectives

The general setup in CALA can be further improved. The ZS, for example, should receive a separate mode for laser-diode beam alignment. Current operation modes allow laser light to propagate from the ATLAS hall to the EBL only under the consideration of radiation generation, thus having several requirements on the state of the LBD, vacuum system and EBL sensors. Diode operation does not pose any risk of radiation, thus these restrictions are unnecessary. An adapted mode would increase user-friendliness for diode operation. Fluctuations in the ATLAS pulse energy, compression, wavefront and contrast have direct impact on laser-driven ion acceleration. The ATLAS pulse energy can be increased further, but this is currently not considered useful due to the limiting temporal contrast. The next urgent improvement concerns identification of the 112 ps pre- and 118 ps post-pulses as well as the suppression of the coherent pedestal that starts $\approx$ 50-100 ps before the peak.

The LION operation can also be improved further. The 50 cm focal length copper OAP, provided it can yield a similar quality as the 150 cm glass OAP, allows for a reduction of the focal spot diameter by a factor of three and an increase of peak intensity by a factor of 9. This is expected to yield considerably higher proton and carbon energies, given the temporal contrast can be restricted further. Continuous and stable data acquisition of incoming and backscatter diagnostics monitoring the EBL would be desirable to further investigate the reason of the shot-to-shot fluctuations.

The WASP currently covers a rather small angular range (up to $\pm$ 1.75°). Extending this range would benefit studying the angular variation of the emission characteristics in more detail.

The RadEye1 detector element's dark current, which is currently around 58 ADU, can be significantly reduced by cooling, thus potentially increasing the dynamic range. This would likely increase the sensitivity at higher proton energies. The production of RadEye1 detectors has ended, and CM49 has been introduced as its successor. It consists only of a single detector element, which covers the same 10 x 5 cm^2 as four RadEye1 elements. However, the connector system has changed, and the read-out electronic has to be close to the detector element, thus in vacuum, suffering from high risk of radiation damage. First studies using CM49 have been promising. Its suitability to detect protons has been demonstrated at conventional accelerators [111], and the detector element as well as read-out electronics have been shown to be vacuum compatible. A qualitative study showed that it can work close to a laser-driven source too, but CM49 has not been used as the main ion diagnostic in a laser-driven ion

experiment so far.

We have introduced QIS and SDF for ion detection, and have demonstrated this method for light ions. With the same considerations, QIS can be used for other ion species as well. For heavier ions, a clearer signal to noise distinction can be made. Most interesting would be a consideration of SDF of other particles, such as electrons.

On-beam background in the detector signal has been observed in this thesis, and should be investigated further. If the suppression renders impossible, an advanced model could aim at modeling the on-beam background with a background SDF (likely based on X-rays).

6.3 Closing Remarks

The general laser-driven ion acceleration performance presented in this work can be put in perspective to results obtained in other laboratories. With almost 10 J laser energy on target, the maximum proton energies of just above 20 MeV have remained low. This translates to only $2\,\mathrm{MeV\,J^{-1}}$, whereas an empirical study comparing published acceleration results found that the maximum proton energy scales with $8.6\,\mathrm{MeV\,J^{-1}}$ [112, 64]. As we are limited by contrast and did not focus to the smallest possible spot yet, it is likely that we have not exploited the full potential yet.

Interestingly, we observe significant carbon acceleration to likewise significant kinetic energies, that is up to 20 MeV/u. Such co-emission has been recently reported in [113], where maximum carbon kinetic energies of 33 MeV/u and proton energies of 18 MeV were observed simultaneously with 6 J of laser energy on target, but from much thinner foils (15 nm) and by the aid of a plasma mirror-enhanced temporal contrast from circularly polarized laser pulses.

Another worthwhile comparison can be drawn to results at GIST in Korea, where ion acceleration with contrast enhancement has been studied with laser energies up to 9.2 J [114]. There, maximum proton energies reached 22 MeV, carbon energies reached 15 MeV/u from 20 nm thick targets, and up to 57 MeV proton and 48 MeV/u maximum carbon energies from an advanced target design.

In conclusion, the loose focusing in LION might limit the achievable maximum energy. But this pragmatic choice simplified day to day operation and resulted in relatively predictable performance. This provided the basis for first dedicated developments towards proton bunch transport, as mentioned in section 5.2 and detailed in the thesis work of Rösch [62], and related iono-acoustic measurements in water as

currently pursued in a thesis work [115].

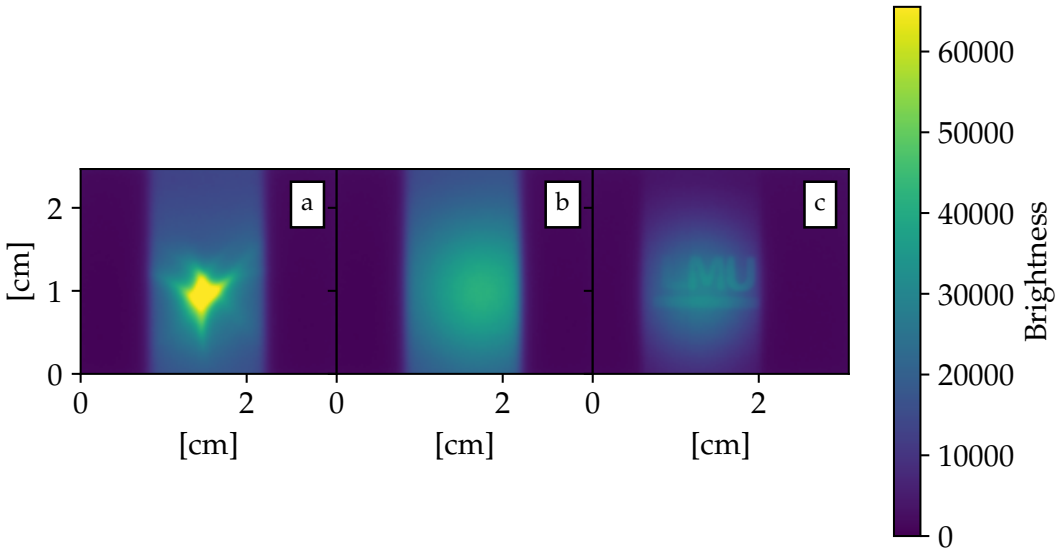

Figure 6.1: Scintillator images of a 12 MeV proton beam. Proton phantom provided by M. Würl. a) is showing the raw 12 MeV proton focus, b) is with a 12 µm scatter foil in the beam at about 80 cm distance from TCC. c) is a shot with an LMU logo shaped phantom inserted in the scattered beam right in front of the scintilliator.

As a glimpse into the near term potential of the setup, we have transformed the proton bunch transport line into a proton radiography setup by inserting a scatter foil shortly behind the quadrupole magnets. Consequently, the proton spot on the scintillator with no scatter foil in the beam (figure 6.1 a) smears out over $\approx$ 2 cm (figure 6.1 b), and an object (here the LMU logo 3d printed out of AR-M2 [116]) can be radiographed with a single proton bunch (figure 6.1 c). Establishing this status quo has been an educative adventure, and is now ready for exploitation.

Appendix A

LION diagnostics

A.0.1 Radiography with Ion Beamline

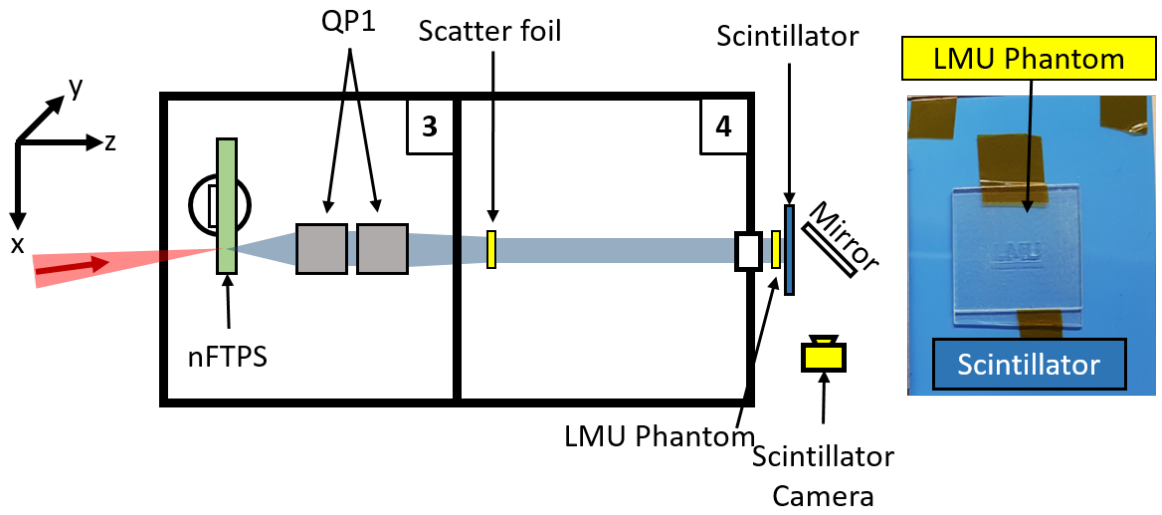

Figure A.1: Schematic radiography setup. The height of the letters is 3.7 mm. The width of the bar is 10 mm, bar height is 1.4 mm.

The proton focusing setup can be easily changed into a radiography setup by inserting a scatter foil shortly after the quadrupoles, as shown in figures A.1 and A.2.

To demonstrate this, we employed an "LMU" phantom. The phantom had been 3d-printed with the material AR-M2, which allows layer thicknesses of 15 µm by radpidobject [116]. M. Würl calculated the water-equivalent-thickness to be WET = 1.096 mm. The complete phantom was 1 mm thick and could be penetrated by proton kinetic energies larger than 9 MeV. The depths of the grooves were L: 40 µm, M: 80 µm,

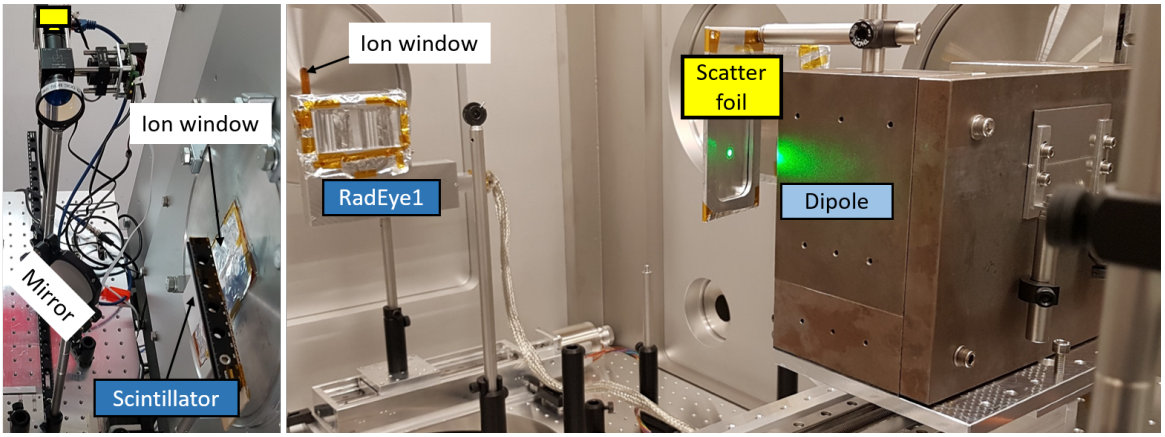

Figure A.2: Picture of radiography setup. After the ion beam has been focused by the QP, it propagates through the scatter foil next to the dipole magnet (at the position marked by the green alignment laser). It then propagates through the ion window, where it hits the LMU phantom and the scintillator. Note that the RadEye1 detector is on a motorized stage, and has been moved away from the beam path for the radiography.

U: 120 µm and the bar beneath: 60 µm. The shape is clearly recognized in the raw scintillator images, shown in figure 6.1.

A.1 RadEye1 Details

Signal strength per pixel is digitized with 12 bit resolution in Analog to Digital Units (ADU). RadEye1 has two available trigger inputs, of which either can be programmed to initiate a read out cycle. An initiated read-out process retrieves the pixel values in a row-sequential format. The read-out mode used in this work drains the accumulated charge from the pixel. However, it has been found that a single read out does not drain saturated pixels completely. This is visible as signal in a following read out. This effect can not be used to increase the dynamic range for proton detection with a following read-out, and stacking like HDR focus images [117]. Saturated pixels return to their typical dark current value after two to three consecutive read outs. A single read-out completes in 375 ms. An alternative rapid-read out mode, designated 'clear', only reads the first six pixels of every row and is completed within 12.5 ms. It is advertised to be suitable for rapid dark current reset prior to image aquisition.

Five clears followed by an image acquisition (and storage) read-out has been the typical operation during experiments. Its performance of background suppression was unsatisfiying for the method presented in this thesis. It appeared that even repeating 'clear' several times in a row is not sufficient if the detector has not been read out within the last $\approx$ five minutes, which can happen regularly during an experiment. Therefore, a new read out cycle called Synchronized-Continous Readout mode (SCR) has been implemented for operation at the 1 Hz ATLAS3000 laser system: On the first trigger input a continuous 1 Hz pulse from the laser hall is initiating two read-outs spaced 500 ms apart. The actual trigger pulse indicating a laser-plasma interaction is sent to the second input, and initiates the saving routine. It saves the exposure containing the laser-plasma interaction (signal image), as well as the empty exposure right before (dark image). The dark image can also be used to monitor pixel deterioration induced by radiation damage during the experiment. The presented data has been obtained with a fresh set of detector elements on the 12th of May 2021. Note that they had no previous exposure to radiation.

A.2 Cut-off Energy versus Transmitted Light

On the 12th of May 2021 we have varied the laser-energy on target by pumping AMP1 with two to four GAIA lasers. We have shot 400 nm and 600 nm thick Formvar plastic foils, and recorded the transmitted light. Figure A.3 shows recorded during this study. The cut-off energies vary for each shot between the four evaluated cut-off stripes. On

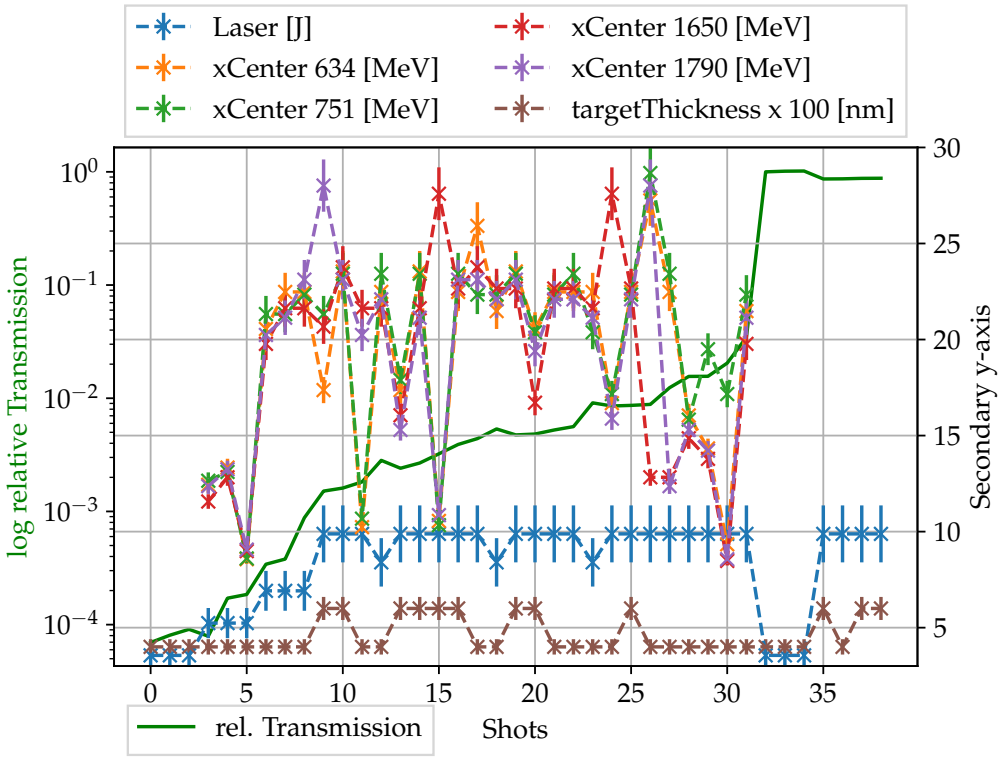

Figure A.3: Transmitted light relative to the incident laser energy in solid green on the logarithmic left y-axis. X-axis represents different shots, sorted for increasing light transmission. On the right linear y-axis target thickness in 100 nm, laser-energy on target in J and cut-off energies for four aluminum stripes in MeV.

the far left, where the relative transmission is around 10^{-4} the proton performance suffers, and on the far right, where transmission is above 10^{-1} no proton signal has been detected. If transmission is between these values, acceleration of protons to energies above 15 MeV is routinely achievable, although not stable. The influence of a target thickness between 400 nm and 600 nm is not observed. The laser-energy has been above 5 J for the better performing shots.

A.3 Back-scattered Light

The back-scattered light diagnostic is of major interest, because it is non-invasive to the ion-bunch and it is placed on the laser-irradiated side of the target. As such it is still functional, even if an application or, as in our case, the first quadrupole magnet is too close to the target that light can not reach the transmitted light diagnostic, as

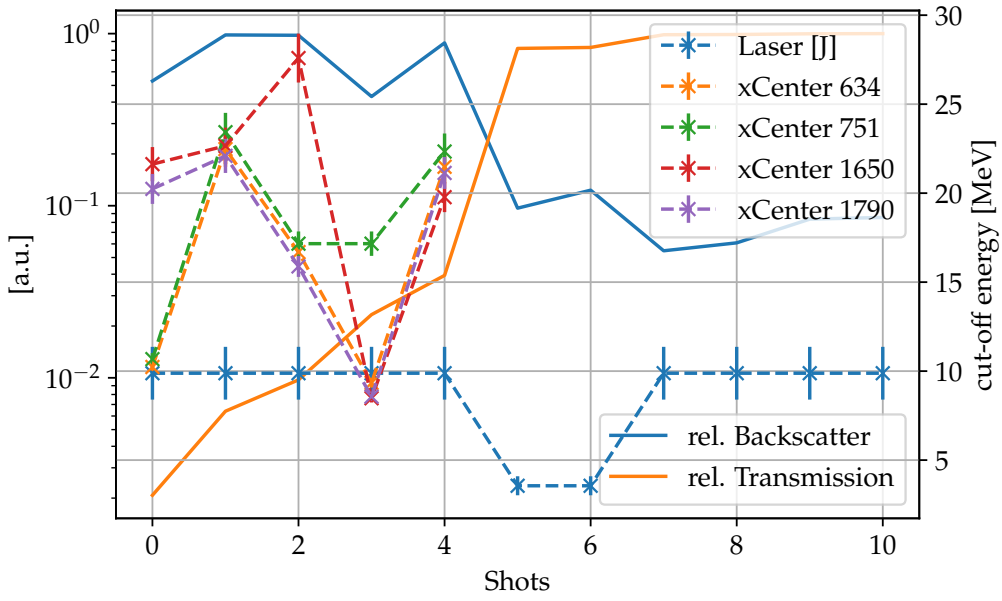

Figure A.4: Transmitted light relative to the few non-saturated backscattered light images. Shots=5 represents shot number 140 and shots=0 represents shot number 103. Data from 20210512.

it is blocked by the first quadrupole. The scatter screen has been placed where the direct target surface reflection of the laser is expected. Example raw data images are shown as insets b) of the spectra presented in the last sections. For the evaluated beamtime the filter setting in front of this diagnostic was too low, and most of the retrieved images are saturated in the region of interest. Summing over the area of interest was therefore only meaningful for the handful of shots which have not been saturated. These have been plotted together with transmission and p^+ cut-off data in figure A.4. With increasing transmitted light the back-scattered light decreases, and at the cross-over point ion-acceleration is reduced below detection level as well. Comments on the shape of the images per shot have been presented in the section containing the strong background spectrum evaluations.

Appendix B

Operating the recording and evaluation software

B.1 Data recording

It is important to use the synchronized continuous read-out mode compatible CamouFlage software:

"project/cala_lion/Software/Radeye/StoreOnTango/
CamCouflage_20210426_2109_VersionWithNoClearsFlexible2ndreadout.exe"

Set all four detector elements to record. Set 2nd Readout start to 705 ms. Press Apply. If the ATLAS oscillator is running, the synchronized 1 Hz trigger will already update the preview section of the software every 500 ms.

Choose the target directory, typically "project/cala_lion/Experiments/beamtimedate/RadeyeIon Check "Automatic Timestamp from Tango Server" to automatically receive the correct shot number from the tango system. Press "Record Images".

Two images will be stored per shot event, which is a trigger signal on input2. First, an empty image, which is read-out 500 ms before the also recorded shot image. Both will have the same shot, but different incremental number.

B.2 How to use pyRadeyePabloneEvaluation

The complete program is available on the LMU physik gitlab repository:

"https://gitlab.physik.uni-muenchen.de/cala/lion/pyradeyepabloneevaluation"

Clone the currently most advanced branch (pxCountBranch2). It has been developed using `Anaconda Spyder`. Users may use this program for evaluating their data.

makePablone.py This is the most fundamental program. All imporant parameters such as beamtime date, setup distances or x-coordinates of the aluminum stripes are set here. Example values are presented in B.4. It contains the code to generate the $E_{kin}(x, y)$ map (`arrEgrid`) on the detector, and creates three nice plots for visual confirmation of its performance. This program is imported and run in many of the following routines.

zTest20210514_evalSaveHistogramsOfInterestingAreas.py Extracts histograms of mono-energetic incident from raw data based on `arrEgrid` and stores them as .npy files.

fitToHistograms.py Fits SDF to .npy histograms. These are the initial fits for calibration of the detectors. This calibration has been done per alu-cutoff per detector element. However, this thesis indicates that it may be enough to do this calibration per detector element. The fitted data is stored as .npy.

makePlotEnergyCalibrations.py Plots the calibration data based on fitToHistrograms.py and their fit with the simple power law approach. Allows for visual check of the calibration performance. Plots are stored as .png and .pdf.

fitEnergyLossModel.py Works with the more advanced multi-cutoff calibration, but is deprecated to the new δ_p approach. Could be the basis of recording material dependent properties however. Interesting to look at.

evaluateRadeye_fitApproach.py Current particle evaluation routine. Incorporates loading power-law based calibration curves, they are fit during runtime. Allows for three different background regions: "StrongBackground", "OrigBackground", and "" which equals weak background. Stores data as .npy files. Can generate spectra plot per evaluated alu-stripe.

B.3 Energy Map Edge Detection

The combination of aluminum stripes and the energy dispersion by the magnet results in the steps seen in figure 4.1. For each aluminum thickness, which is available at a certain range of x-coordinates, and defined by its 'xCenter', there is a y-coordinate for which the ion signal starts to appear. This position is directly related to the cut-off

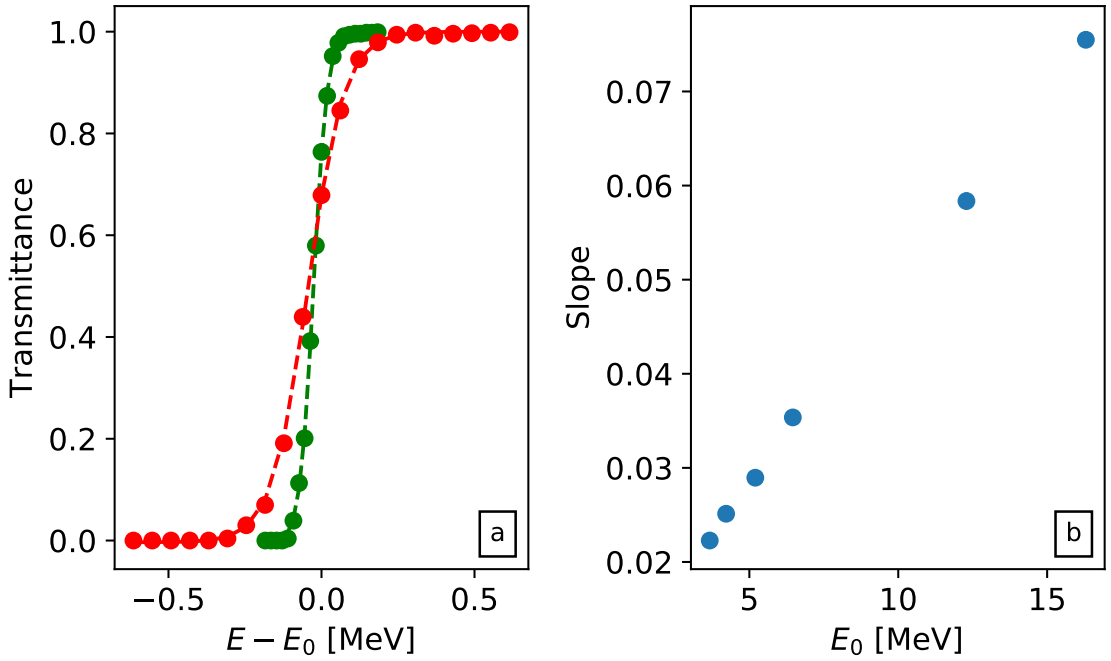

Figure B.1: TRIM simulations of the ratio of transmitted particles. Figure a) is showing simulated data (dots) and respective sigmoid fits (dashed lines) for incident protons around kinetic energies E_1. Green is showing an energy range around $E_0 = 3.7$ MeV passing through 112 µm thick aluminum. Red is showing an energy range around $E_0 = 12.3$ MeV passing through 892 µm thick aluminum. Figure b) shows the slope steepness for proton kinetic energies E_0 at their respective aluminum thickness E_{cutoff}.

energy, so we can infer $E_{kin}(x, y)$ on this coordinate. We can do this for example at all the 'x' marked positions in figure 4.3. These points are important for generating a map of $E_{kin}(x, y)$ over the complete detector, which is further discussed in section 4.1.

For a certain x-coordinate, starting from the highest y-values and sliding towards the y zero position is similar to a multi-energetic proton beam scan for an object with a fixed thickness. The ratio of transmitted particles versus incidence particles, or 'Transmittance', can be estimated via TRIM simulations, as shown in figure B.1 a). This plot shows that the slope of Transmittance is decreasing for higher energies, yielding a less defined edge, likely due to straggling effects at these borders. The effect on the presented method has not been studied in detail, as the decreasing energy dispersion of the dipole leads to a spatial compression of the higher kinetic energies. From these studies we should remember that the signal border detection is easier at lower energies, where the energetic dispersion is stronger as well. Due to the mechanism

of acceleration in this setup, there are also a lot more protons present at lower energies, which increases the signal and allows for easier edge detection.

B.4 Cala LION Fit Parameters

This section notes the used setup parameters and the parameters obtained from the magnetic field fit for future reference.

Listing B.1: Setup configuration

```
1                'beamtimeDate': '20210512',
2                'tccToMagnet': 83, #z1
3                'jochThickness': 2,
4                'lengthMagneticField': 10, #zd
5                'magnetToDetector': 68.2, #zm
6                'slitHeight': 2e-2,##units are cm!
7                'slitWidth': 5 #cm, entrance aperture of
                    dipole
8            }
```

Listing B.2: Files and arrPunkte

```
1            signalFileName = '0006
                _20210512_170140284_20210512_170143_firstRun_001363
                -A.raw'
2            signalFileName2 = '0006
                _20210512_170140284_20210512_170143_firstRun_001363
                -A.raw'
3
4            backgroundFile2 = '0006
                _20210512_170140284_20210512_170142_firstRun_001362
                -A.raw'
5            backgroundFile = '0007
                _20210512_170232492_20210512_170234_firstRun_001466
                -A.raw'
6            numRadeye=4
7            arrPunkte = np.array( #for pablone since 20210101
8            [
```

```
9           [3.67, 1085, 702],
10          [4.22, 915, 634],
11          [4.22, 1900, 1010],#new
12          [5.20, 1820, 616],
13          [5.20, 761, 548],
14          [6.46, 640, 490],
15          [8.935, 490, 397],
16          [12.29, 1420, 277],
17          ])
```

B.1 demonstrates how to use `waspConfig`. Configuration of files and of the positions of the support points `arrPunkte` in listing B.2.

These parameters make up the input. If the fit fails, parameters may have to be adjusted in the sub-routine `fit_equienergylines_sub`.

Listing B.3: Magnet model function

```
1           def magnetModel20210118(self,data, a, b, c, d, e):
2           x = data[0]
3           y = data[1]
4           return self.FixedFactor * (a * (x - d)**4 + b
5           * (x-d)**2 + c) / (y + e)
```

The function currently used for fitting is in B.3. The presented data results in the following fit parameters:

- $a = -1.66541866e-05$ T/cm^4
- $b = 1.92619591e-03$ T/cm^2
- $c = 1.62761890e-01$ T
- $d = 5.68214228e+00$ cm
- $e = -2.99049606e-01$ cm

Appendix C

Calculations

Kinetic Energy of Relativistic Particles

The relationship between kinetic energy E_{kin} and normalized momentum $\gamma\beta$, with $E_0 = m_0c^2$

$$E_{kin} = (\gamma - 1)m_0c^2 \tag{C.1}$$

$$\gamma = \frac{E_{kin}}{m_0c^2} + 1 = \frac{1}{\sqrt{1-\beta^2}} \tag{C.2}$$

$$\gamma\beta = \sqrt{\gamma^2 - 1} \tag{C.3}$$

$$\gamma\beta = \sqrt{(\frac{E_{kin}}{m_0c^2} + 1)^2 - 1} \tag{C.4}$$

Also useful $\beta(E_{kin})$

$$\beta(E_{kin}) = \sqrt{1 - \frac{E_0^2}{(E_{kin} + E_0)^2}} \tag{C.5}$$

The relativistic relationship between E_{kin} and v

$$E_{kin} = (\gamma - 1)E_0 \tag{C.6}$$

$$\gamma = \frac{E_{kin}}{E_0} + 1 \tag{C.7}$$

$$1 - \beta^2 = (\frac{1}{\frac{E_{kin}}{E_0} + 1}) \tag{C.8}$$

$$v = c\sqrt{1 - (\frac{1}{\frac{E_{kin}}{E_0} + 1})^2} \tag{C.9}$$

Laser-peak Intensity

Laser-peak intensity contains the measured quantities of laser-pulse energy E_L, laser pulse temporal full width at half maximum intensity duration τ_L and laser focus area in terms of full width at half maximum intensity diameter in x- and y-dimension d_{FWHM}. E_L contains the complete pulse energy. τ_L and d_{FWHM}, however, are Full-Width-Half-Maximum (FWHM) values. We assume a Gaussian distribution for τ_L and d_{FWHM}.

A Gaussian distribution normalized to area and centered around $x = 0$ is

$$f(x, \sigma) = \frac{1}{\sqrt{2\pi\sigma^2}} exp(-\frac{x^2}{2\sigma^2}) \tag{C.10}$$

Sigma is related to Full-Width-Half-Maximum (FWHM) with

$$\sigma = \frac{FWHM}{2\sqrt{2ln(2)}} \tag{C.11}$$

The peak of the Gaussian is then

$$f(0, FWHM) = 2\sqrt{\frac{ln(2)}{\pi}} \frac{1}{FWHM} \tag{C.12}$$

Peak-intensity is then

$$I_L = \left(2\sqrt{\frac{ln(2)}{\pi}}\right)^3 \frac{E_L}{\tau_L \cdot d_{FWHM}^2} \approx \frac{0.83 E_L}{\tau_L \cdot d_{FWHM}^2} \tag{C.13}$$

List of Abbreviations

Abbreviation	Explanation
ADU	Analog to Digital Units
ALPACA	A Laser-driven Proton-ACcelerator Applications-platform
ASE	Amplified Spontaneous Emission
ATLAS	Advanced Titanium Saphire Laser
BOA	Break-Out-Afterburner
CALA	Centre for Advanced Laser Applications
CMOS	Complementary Metal-Oxide-Semiconductor
CPA	Chirped Pulse Amplification
DM	Deformable Mirror
EBL	Experimental Beam Lines
ETTF	Electron and Thomson Test Facility
FIREFLI	Foil-electrode Ionization chambeR For Laser-driven Ions
FROG	Frequency-Resolved-Optical-Gating
HF	High Field
LAN	Local Area Network
Langau	Landau distribution convoluted with a Gaussian distribution
LBD	Laser Beamline Delivery
LEX Photonics	Laboratory of Extreme Photonics
LION	Laser-driven ION
LUX	Laser-driven Undulator X-RaySource
MAP	Munich-Centre for Advanced Photonics
MPQ	Max-Planck Institute for Quantum optics
nFTPS	nano-Foil-Target-Positioning-System
OAP	Off-Axis-Parabolic mirror
PIXE	Proton Induced X-ray Emission
PMQ	Permanent magnetic quadrupole

Abbreviation	Explanation
QIS	Quantitative Ion Spectrometry
QP	Quadrupole
RPA	Radiation-Pressure-Acceleration
SCR	Synchronized-Continuous Readout
SDF	Signal Distribution Function
SPECTRE	Source for Powerful Energetic Compact Thomson Radiation Experiments
TCC	Target-Chamber-Center
TM	Turning-Mirror
TNSA	Target-Normal Sheath Acceleration
WASP	Wide Angle SPectrometer
ZS	Zentrale Steuerung

Publications and Conference Contributions

Journal Articles

- F. H. Lindner, D. Haffa, J. Bin, F. Englbrecht, Y. Gao, J. Gebhard, **J. Hartmann**, P. Hilz, C. Kreuzer, S. Lehrack, T. M. Ostermayr, T. F. Rösch, M. Speicher, M. Würl, K. Parodi, J. Schreiber and P. G. Thirolf. Towards swift ion bunch acceleration by high-power laser pulses at the Centre for Advanced Laser Applications (CALA). *Nucl. Instrum. Methods in Phys. Res. B*, 402, 354-357, 2017.

- Y. Gao, J. Bin, D. Haffa, C. Kreuzer, **J. Hartmann**, M. Speicher, F. H. Lindner, T. M. Ostermayr, P. Hilz, Peter T. F. Rösch, S. Lehrack, F. Englbrecht, S. Seuferling, M. Gilljohann, H. Ding, W. Ma, K. Parodi and J. Schreiber. An automated, 0.5 Hz nano-foil target positioning system for intense laser plasma experiments. *High Power Laser Science and Engineering*, 5, 2017.

- **J. Hartmann**, D. Haffa, M. Speicher, J. Bin, P. Hilz, C. Kreuzer, T. Ostermayr, S. Lehrack and J. Schreiber. The spatial contrast challenge for intense laser-plasma experiments. *J. Phys.: Conf. Ser.* 1079 012003, 2018.

- M. Speicher, D. Haffa, M. A. O. Haug, J. Bin, Y. Gao, **J. Hartmann**, P. Hilz, C. Kreuzer, F. H. Lindner, T. M. Ostermayr, T. F. Rösch, R. Yang and J. Schreiber. Integrated double-plasma-mirror targets for contrast enhancement in laser ion acceleration. *J. Phys.: Conf. Ser.* 1079 012002, 2018.

- F. H. Lindner, J. H. Bin, F. Englbrecht, D. Haffa, P. R. Bolton, Y. Gao, **J. Hartmann**, P. Hilz, C. Kreuzer, T. M. Ostermayr, T. F. Rösch, M. Speicher, K. Parodi, P. G. Thirolf and J. Schreiber. A novel approach to electron data

background treatment in an online wide-angle spectrometer for laser-accelerated ion and electron bunches. *Rev. Sci. Instrum.*, 89, 1, 013301, 2018.

- P. Hilz, T. M. Ostermayr, A. Huebl, V. Bagnoud, B. Borm, M. Bussmann, M. Gallei, J. Gebhard, D. Haffa, **J. Hartmann**, T. Kluge, F. H. Lindner, P. Neumayr, C.G. Schaefer, U. Schramm, P. G. Thirolf, T. F. Rösch, F. Wagner, B. Zielbauer and J. Schreiber. Isolated proton bunch acceleration by a Petawatt laser pulse. *Nat. Commun*, 9, 423, 2018.

- D. Haffa, R. Yang, J. Bin, S. Lehrack, F.-E. Brack, H. Ding, F. S. Englbrecht, Y. Gao, J. Gebhard, M. Gilljohann, J. Gotzfried, **J. Hartmann**, S. Herr, P. Hilz, S. D. Kraft, C. Kreuzer, F. Kroll, F. H. Lindner, J. Metzkes-Ng, T. M. Ostermayr, E. Ridente, T. F. Rösch, G. Schilling, H.-P. Schlenvoigt, M. Speicher, D. Taray, M. Würl, K. Zeil, U. Schramm, S. Karsch, K. Parodi, P. R. Bolton, W. Assmann and J. Schreiber. I-BEAT: Ultrasonic method for online measurement of the energy distribution of a single ion bunch. *Scientific Reports*, 9, 6714, 2019.

- T. F. Rösch, Z. Szabo, D. Haffa, J. Bin, S. Brunner, F. S. Englbrecht, A. A. Friedl, Y. Gao, **J. Hartmann**, P. Hilz, C. Kreuzer, F. H. Lindner, T. M. Ostermayr, R. Polanek, M. Speicher, E. R. Szabo, D. Taray, T. Tőkes, M. Würl, K. Parodi, K. Hideghety and J. Schreiber. A feasibility study of zebrafish embryo irradiation with laser-accelerated protons. *Rev. Sci. Instrum.*, 91, 6, 063303, 2020.

- F. S. Englbrecht, A. Döpp, **J. Hartmann**, F. H. Lindner, M. L. Groß, H.-F. Wirth, P. G. Thirolf, S. Karsch, J. Schreiber, K. Parodi and G. Dedes. Radiation protection modelling for 2.5 Petawatt-laser production of ultrashort x-ray, proton and ion bunches: Monte Carlo model of the Munich CALA facility. *J. Radiol. Prot.*, 40 1048, 2020.

- T. M. Ostermayr, C. Kreuzer, F. S. Englbrecht, J. Gebhard, **J. Hartmann**, A. Huebl, D. Haffa, P. Hilz, K. Parodi, J. Wenz, M. E. Donovan, G. Dyer, E. Gaul, J. Gordon, M. Martinez, E. McCary, M. Spinks, G. Tiwari, B. M. Hegelich and J. Schreiber. Laser-driven x-ray and proton micro-source and application to simultaneous single-shot bi-modal radiographic imaging. *Nat. Commun.*, volume 11, 6174, 2020.

- J. J. Krauth, K. Schuhmann, M. A. Ahmed, F. D. Amaro, P. Amaro, F. Biraben, T. Chen, D. S. Covita, A. J. Dax, M. Diepold, L. M. P. Fernandes, B. Franke, S.

Galtier, A. L. Gouvea, J. Götzfried, T. Graf, T. W. Hänsch, **J. Hartmann**, M. Hildebrandt, P. Indelicato, L. Julien, K. Kirch, A. Knecht, Y. Liu, J. Machado, C. M. B. Monteiro, F. Mulhauser, B. Naar, T. Nebel, F. Nez, J. M. F. dos Santos, J. P. Santos, C. I. Szabo, D. Taqqu, J. F. C. A. Veloso, J. Vogelsang, A. Voss, B. Weichelt, R. Pohl, A. Antognini and Franz Kottmann. Measuring the α-particle charge radius with muonic helium-4 ions. *Nature*, 589(7843), 527-531, 2021.

Conference Contributions

- **Oral** Automated nano-Foil Target Positioning System. *3rd Targetry for HRR Laser-Driven Sources*, Salamanca (Spain), 2017.
- **Oral** Application and potential of laser–accelerated ion bunches. *Nuclear Photonics*, Brasov (Romania), 2018.
- **Oral, invited** Laser plasma interaction and proton diagnostics. *ELI User Workshop on Laser-Driven Acceleration and Applications*, Dolní Břežany (Czech Republic), 2019.
- **Paper + Oral** Commissioning of the laser-driven ion acceleration beamline at the Centre for Advanced Laser Applications. *Laser Acceleration of Electrons, Protons, and Ions VI (Vol. 11779, pp. 44-49). SPIE* + virtual. 2021.
- **Oral** Laser-Driven Ion Acceleration at the Centre for Advanced Laser Applications. *41st International Workshop on High-Energy-Density Physics with Intense Ion and Laser Beams*, virtual, 2021.
- **Oral** Recent updates on the nano-foil target positioning system. *TARG5 Targetry for High Repetition Rate Laser-Driven Sources Workshop*, Dresden (Germany), 2021.

Bibliography

[1] H. Geiger und E. Marsden, *The London, Edinburgh, and Dublin Philosophical Magazine and Journal of Science* **25** (1913), 604.

[2] E. Rutherford und T. Royds, *The London, Edinburgh, and Dublin Philosophical Magazine and Journal of Science* **17** (1909), 281.

[3] R. Wideröe, *Archiv für Elektrotechnik* **21** (1928), 387.

[4] S. Mathot, G. Anelli, S. Atieh, A. Bilton, B. Bulat, T. Callamand, S. Calvo, G. Favre, J.M. Geisser, A. Gerardin et al. , *Nuclear Instruments and Methods in Physics Research Section B: Beam Interactions with Materials and Atoms* **459** (2019), 153.

[5] D. Strickland und G. Mourou, *Optics communications* **55** (1985), 447.

[6] V. Veksler, *The Soviet Journal of Atomic Energy* **2** (1957), 525.

[7] T. Tajima und J.M. Dawson, *Physical Review Letters* **43** (1979), 267.

[8] A.R. Maier, N.M. Delbos, T. Eichner, L. Hübner, S. Jalas, L. Jeppe, S.W. Jolly, M. Kirchen, V. Leroux, P. Messner, M. Schnepp, M. Trunk, P.A. Walker, C. Werle und P. Winkler, *Phys. Rev. X* **10** (2020), 031039.

[9] R.A. Snavely, M.H. Key, S.P. Hatchett, T.E. Cowan, M. Roth, T.W. Phillips, M.A. Stoyer, E.A. Henry, T.C. Sangster, M.S. Singh, S.C. Wilks, A. MacKinnon, A. Offenberger, D.M. Pennington, K. Yasuike, A.B. Langdon, B.F. Lasinski, J. Johnson, M.D. Perry und E.M. Campbell, *Physical Review Letters* **85** (2000), 2945.

[10] D. Habs, P. Thirolf, M. Gross, K. Allinger, J. Bin, A. Henig, D. Kiefer, W. Ma und J. Schreiber, *Applied Physics B* **103** (2011), 471.

[11] M. Borghesi, A. Bigongiari, S. Kar, A. Macchi, L. Romagnani, P. Audebert, J. Fuchs, T. Toncian, O. Willi, S. Bulanov et al. , *Plasma Physics and Controlled Fusion* **50** (2008), 124040.

[12] C. Goyon, B.B. Pollock, D.P. Turnbull, A. Hazi, L. Divol, W.A. Farmer, D. Haberberger, J. Javedani, A.J. Johnson, A. Kemp, M.C. Levy, B. Grant Logan, D.A. Mariscal, O.L. Landen, S. Patankar, J.S. Ross, A.M. Rubenchik, G.F. Swadling, G.J. Williams, S. Fujioka, K.F.F. Law und J.D. Moody, *Phys. Rev. E* **95** (2017), 033208.

[13] J. van Tilborg, S. Steinke, C.G.R. Geddes, N.H. Matlis, B.H. Shaw, A.J. Gonsalves, J.V. Huijts, K. Nakamura, J. Daniels, C.B. Schroeder, C. Benedetti, E. Esarey, S.S. Bulanov, N.A. Bobrova, P.V. Sasorov und W.P. Leemans, *Phys. Rev. Lett.* **115** (2015), 184802.

[14] T. Nonnenmacher, T.S. Dascalu, R. Bingham, C.L. Cheung, H.T. Lau, K. Long, J. Pozimski und C. Whyte, *Applied Sciences* **11** (2021), 4357.

[15] T. Ostermayr, C. Kreuzer, F. Englbrecht, J. Gebhard, J. Hartmann, A. Huebl, D. Haffa, P. Hilz, K. Parodi, J. Wenz et al. , *Nature Communications* **11** (2020), 1.

[16] M. Barberio, S. Veltri, M. Scisciò und P. Antici, *Scientific Reports* **7** (2017), 1.

[17] M. Zimmer, S. Scheuren, A. Kleinschmidt, N. Mitura, A. Tebartz, G. Schaumann, T. Abel, T. Ebert, M. Hesse, Ş. Zähter et al. , *Nature Communications* **13** (2022), 1.

[18] L. Senje, M. Coughlan, D. Jung, M. Taylor, G. Nersisyan, D. Riley, C. Lewis, O. Lundh, C.G. Wahlström, M. Zepf et al. , *Applied Physics Letters* **110** (2017), 104102.

[19] A. Prasselsperger, M. Coughlan, N. Breslin, M. Yeung, C. Arthur, H. Donnelly, S. White, M. Afshari, M. Speicher, R. Yang et al. , *Physical Review Letters* **127** (2021), 186001.

[20] B.G. Cartwright, E. Shirk und P. Price, *Nuclear Instruments and Methods* **153** (1978), 457.

[21] S. Sakabe, T. Mochizuki, T. Yamanaka und C. Yamanaka, *Review of Scientific Instruments* **51** (1980), 1314.

[22] D. Jung, R. Hörlein, D. Gautier, S. Letzring, D. Kiefer, K. Allinger, B. Albright, R. Shah, S. Palaniyappan, L. Yin et al. , *Review of Scientific Instruments* **82** (2011), 043301.

[23] A. Yogo, T. Maeda, T. Hori, H. Sakaki, K. Ogura, M. Nishiuchi, A. Sagisaka, P. Bolton, M. Murakami, S. Kawanishi et al. , *Nuclear Instruments and Methods in Physics Research Section A: Accelerators, Spectrometers, Detectors and Associated Equipment* **653** (2011), 189.

[24] V. Scuderi, S.B. Jia, M. Carpinelli, G. Cirrone, G. Cuttone, G. Korn, T. Licciardello, M. Maggiore, D. Margarone, P. Pisciotta et al. , *Nuclear Instruments and Methods in Physics Research Section A: Accelerators, Spectrometers, Detectors and Associated Equipment* **740** (2014), 87.

[25] S. Busold, D. Schumacher, O. Deppert, C. Brabetz, S. Frydrych, F. Kroll, M. Joost, H. Al-Omari, A. Blažević, B. Zielbauer et al. , *Physical Review Special Topics-Accelerators and Beams* **16** (2013), 101302.

[26] M. Schollmeier, S. Becker, M. Geißel, K. Flippo, A. Blažević, S. Gaillard, D. Gautier, F. Grüner, K. Harres, M. Kimmel et al. , *Physical Review Letters* **101** (2008), 055004.

[27] T. Rösch: *Ein Permanentmagnet-Aufbau zur Fokussierung Laser-beschleunigter Ionen.* Munich, Ludwig-Maximilians-Universität München, Master's thesis, 11 2015.

[28] F. Kroll, F.E. Brack, C. Bernert, S. Bock, E. Bodenstein, K. Brüchner, T.E. Cowan, L. Gaus, R. Gebhardt, U. Helbig et al. , *Nature Physics* **18** (2022), 316.

[29] D. Jahn, D. Schumacher, C. Brabetz, F. Kroll, F. Brack, J. Ding, R. Leonhardt, I. Semmler, A. Blažević, U. Schramm et al. , *Physical Review Accelerators and Beams* **22** (2019), 011301.

[30] F.E. Brack, F. Kroll, L. Gaus, C. Bernert, E. Beyreuther, T.E. Cowan, L. Karsch, S. Kraft, L.A. Kunz-Schughart, E. Lessmann et al. , *Scientific Reports* **10** (2020), 1.

[31] F. Wagner, O. Deppert, C. Brabetz, P. Fiala, A. Kleinschmidt, P. Poth, V. Schanz, A. Tebartz, B. Zielbauer, M. Roth et al. , *Physical Review Letters* **116** (2016), 205002.

[32] A. Higginson, R. Gray, M. King, R. Dance, S. Williamson, N. Butler, R. Wilson, R. Capdessus, C. Armstrong, J. Green et al. , *Nature Communications* **9** (2018), 1.

[33] S.E. Combs, O. Jäkel, T. Haberer und J. Debus, *Radiotherapy and Oncology* **95** (2010), 41.

[34] D. Forschungsgemeinschaft. *Project Details EXC 158: Munich-Centre for Advanced Photonics (MAP).* `https://gepris.dfg.de/gepris/projekt/24819222`, 2021. Last visited on Mon. 15 Nov 2021.

[35] Y. Gao, J. Bin, D. Haffa, C. Kreuzer, J. Hartmann, M. Speicher, F.H. Lindner, T.M. Ostermayr, P. Hilz, T.F. Rösch, S. Lehrack, F. Englbrecht, S. Seuferling, M. Gilljohann, H. Ding, W. Ma, K. Parodi und J. Schreiber, *High Power Laser Science and Engineering* **5** (2017), e12.

[36] D. Haffa, R. Yang, J. Bin, S. Lehrack, F.E. Brack, H. Ding, F.S. Englbrecht, Y. Gao, J. Gebhard, M. Gilljohann, J. Götzfried, J. Hartmann, S. Herr, P. Hilz, S.D. Kraft, C. Kreuzer, F. Kroll, F.H. Lindner, J. Metzkes-Ng, T.M. Ostermayr, E. Ridente, T.F. Rösch, G. Schilling, H.P. Schlenvoigt, M. Speicher, D. Taray, M. Würl, K. Zeil, U. Schramm, S. Karsch, K. Parodi, P.R. Bolton, W. Assmann und J. Schreiber, *Scientific Reports* **9** (2019).

[37] T.F. Rösch, Z. Szabo, D. Haffa, J. Bin, S. Brunner, F.S. Englbrecht, A.A. Friedl, Y. Gao, J. Hartmann, P. Hilz, C. Kreuzer, F.H. Lindner, T.M. Ostermayr, R. Polanek, M. Speicher, E.R. Szabo, D. Taray, T. Tokes, M. Wurl, K. Parodi, K. Hideghety und J. Schreiber, *Review of Scientific Instruments* **91** (2020), 063303.

[38] J. Hartmann, D. Haffa, M. Speicher, J. Bin, P. Hilz, C. Kreuzer, T. Ostermayr, S. Lehrack und J. Schreiber, *Journal of Physics: Conference Series* **1079** (2018).

[39] D. Haffa, J. Bin, M. Speicher, K. Allinger, J. Hartmann, C. Kreuzer, E. Ridente, T.M. Ostermayr und J. Schreiber, *Scientific Reports* **9** (2019).

[40] M. Speicher, D. Haffa, M.A. Haug, J. Bin, Y. Gao, J. Hartmann, P. Hilz, C. Kreuzer, F.H. Lindner, T.M. Ostermayr et al. , *JPhCS* **1079** (2018), 012002.

[41] D. Haffa: *Tailored online diagnostics for a laser-driven plasma ion source prototype.* Ludwig-Maximilians-Universität München, Dissertation, 9 2019.

[42] J. Hartmann: *From a laser focus to an ion focus.* Ludwig-Maximilians-Universität München, Master's thesis, 2017.

[43] Naeser, Thorsten. *Centre for Advanced Laser Applications*, 2021. `https://www.cala-laser.de`, Last accessed on 2022-03-01.

[44] T. Böhlen, F. Cerutti, M. Chin, A. Fassò, A. Ferrari, P.G. Ortega, A. Mairani, P.R. Sala, G. Smirnov und V. Vlachoudis, *Nuclear data sheets* **120** (2014), 211.

[45] A. Ferrari, J. Ranft, P.R. Sala und A. Fassò: *FLUKA: A multi-particle transport code (Program version 2005).* Nummer CERN-2005-10. Cern, 2005.

[46] F.S. Englbrecht, A. Döpp, J. Hartmann, F.H. Lindner, M.L. Groß, H.F. Wirth, P.G. Thirolf, S. Karsch, J. Schreiber, K. Parodi et al. , *Journal of Radiological Protection* **40** (2020), 1048.

[47] Götz, Andy and Chaize, Jean-Michel. *Centre for Advanced Laser Applications*, 2015. `https://www.tango-controls.org/`, Last accessed on 2022-03-01.

[48] L. Doyle: *Implementation of an Adaptive Optics System for Focus Optimization at the Centre for Advanced Laser Applications.* Munich, Ludwig-Maximilians-Universität München, Master's thesis, 3 2019.

[49] L. Flaig: *Foil Electrode Ionization Chamber with Red Light Emission for Laser-Driven Ions.* Munich, Ludwig-Maximilians-Universität München, Master's thesis, 1 2021.

[50] M.W. Berndl: *Licht-basierte Laser-Plasma Metrologie.* Munich, Ludwig-Maximilians-Universität München, Master's thesis, 9 2020.

[51] L. Tischendorf: *Transport of Laser-Accelerated Ions with Permanent Magnet Quadrupole Lenses – Effects of Field- and Alignmenterrors on the Focus Shape.* Munich, Ludwig-Maximilians-Universität München, Master's thesis, 9 2020.

[52] N. Technologies. *LION Bulk Shielding Calculations.* LION Radiation folder, 2014. Last visited on Mon. 15 Nov 2021.

[53] Fastlite. *Fastlite - Dazzler*, 2022. https://fastlite.com/produits/dazzler-ultrafast-pulse-shaper/, Last accessed on 2022-05-19.

[54] Fastlite. *Fastlite - Mazzler*, 2022. https://fastlite.com/produits/mazzler-programmable-spectral-filter/, Last accessed on 2022-05-19.

[55] UltraFast Innovations. *UltraFast Innovations - Tundra*, 2022. https://www.ultrafast-innovations.com/devices/TUNDRA.html, Last accessed on 2022-05-19.

[56] Rick Trebino. *Swamp Optics - FROG*, 2022. https://www.swampoptics.com/frog.html, Last accessed on 2022-05-19.

[57] Fastlite. *Fastlite - Wizzler*, 2022. https://fastlite.com/produits/wizzler-ultrafast-pulse-measurement/, Last accessed on 2022-05-19.

[58] Ludwig-Maximilians-Universität München. *ATLAS 3000*, 2022. https://www.pulse.physik.uni-muenchen.de/research/high-power/atlas/index.html, Last accessed on 2022-05-19.

[59] C.E. Frank: *Development of an Optical Setup to Verify the Temporal Beam Drift of an Ultrashort Pulse Petawatt Laser System.* Munich, Ludwig-Maximilians-Universität München, Bachelor's thesis, 8 2021.

[60] M. Kögler: *Construction of a vacuum microscope.* Munich, Ludwig-Maximilians-Universität München, Bachelor's thesis, 8 2014.

[61] Sasaki,Shigeyuki. *Mitutoyo Europe GmbH*, 2022. https://shop.mitutoyo.de/web/mitutoyo/de/mitutoyo/05.04.05/M%20Plan%20NIR%2020X/$catalogue/mitutoyoData/PR/378-824-5/index.xhtml, Last accessed on 2022-04-15.

[62] T. Rösch: *Characterization of a Permanent Magnet Quadrupoles Focus of Laser-accelerated Protons.* Ludwig-Maximilians-Universität München, Dissertation, 2 2022.

[63] P. Gibbon: *Short pulse laser interactions with matter: an introduction.* World Scientific, 2005.

[64] G. Mainfray und G. Manus, *Reports on Progress in Physics* **54** (1991), 1333.

[65] N.B. Delone und V.P. Krainov, *Physics-Uspekhi* **41** (1998), 469.

[66] M. Zhou, J. Bin, D. Haffa, X. Yan und J. Schreiber, *Plasma Physics and Controlled Fusion* **59** (2017), 055020.

[67] M. Kaluza, J. Schreiber, M.I. Santala, G.D. Tsakiris, K. Eidmann, J. Meyer-ter Vehn und K.J. Witte, *Physical Review Letters* **93** (2004), 045003.

[68] G. Doumy, F. Quéré, O. Gobert, M. Perdrix, P. Martin, P. Audebert, J. Gauthier, J.P. Geindre und T. Wittmann, *Physical Review E* **69** (2004), 026402.

[69] P.L. Poole, A. Krygier, G.E. Cochran, P. Foster, G. Scott, L. Wilson, J. Bailey, N. Bourgeois, C. Hernandez-Gomez, D. Neely et al. , *Scientific Reports* **6** (2016), 1.

[70] Y. Wang, S. Wang, A. Rockwood, B.M. Luther, R. Hollinger, A. Curtis, C. Calvi, C.S. Menoni und J.J. Rocca, *Optics Letters* **42** (2017), 3828.

[71] A. Macchi, M. Borghesi und M. Passoni, *Reviews of Modern Physics* **85** (2013), 751.

[72] T. Nakamura, S.V. Bulanov, T.Z. Esirkepov und M. Kando, *Physical Review Letters* **105** (2010), 135002.

[73] D. Forslund, J. Kindel, K. Lee, E. Lindman und R. Morse, *Physical Review A* **11** (1975), 679.

[74] F. Brunel, *Physical Review Letters* **59** (1987), 52.

[75] W. Kruer und K. Estabrook, *The Physics of fluids* **28** (1985), 430.

[76] H. Daido, M. Nishiuchi und A.S. Pirozhkov, *Reports on Progress in Physics* **75** (2012), 056401.

[77] S. Steinke, P. Hilz, M. Schnürer, G. Priebe, J. Bränzel, F. Abicht, D. Kiefer, C. Kreuzer, T. Ostermayr, J. Schreiber et al. , *Physical Review Special Topics-Accelerators and Beams* **16** (2013), 011303.

[78] S.P. Hatchett, C.G. Brown, T.E. Cowan, E.A. Henry, J.S. Johnson, M.H. Key, J.A. Koch, A.B. Langdon, B.F. Lasinski, R.W. Lee et al. , *Physics of Plasmas* **7** (2000), 2076.

[79] T. Esirkepov, M. Borghesi, S. Bulanov, G. Mourou und T. Tajima, *Physical Review Letters* **92** (2004), 175003.

[80] J. Bin, W. Ma, K. Allinger, H. Wang, D. Kiefer, S. Reinhardt, P. Hilz, K. Khrennikov, S. Karsch, X.Q. Yan et al. , *Physics of Plasmas* **20** (2013), 073113.

[81] L. Yin, B. Albright, B. Hegelich und J. Fernández, *Laser and Particle Beams* **24** (2006), 291.

[82] J. Schreiber, F. Bell, F. Grüner, U. Schramm, M. Geissler, M. Schnürer, S. Ter-Avetisyan, B.M. Hegelich, J. Cobble, E. Brambrink, J. Fuchs, P. Audebert und D. Habs, *Physical Review Letters* **97** (2006).

[83] M. Passoni, L. Bertagna und A. Zani, *Nuclear Instruments and Methods in Physics Research Section A: Accelerators, Spectrometers, Detectors and Associated Equipment* **620** (2010), 46.

[84] J. Fuchs, P. Antici, E. d'Humières, E. Lefebvre, M. Borghesi, E. Brambrink, C. Cecchetti, M. Kaluza, V. Malka, M. Manclossi et al. , *Nature Physics* **2** (2006), 48.

[85] K. Zeil, S. Kraft, S. Bock, M. Bussmann, T. Cowan, T. Kluge, J. Metzkes, T. Richter, R. Sauerbrey und U. Schramm, *New Journal of Physics* **12** (2010), 045015.

[86] S. Keppler, N. Elkina, G. Becker, J. Hein, M. Hornung, M. Mäusezahl, C. Rödel, I. Tamer, M. Zepf und M. Kaluza, *Physical Review Research* **4** (2022), 013065.

[87] J. Schreiber, P.R. Bolton und K. Parodi, *Review of Scientific Instruments* **87** (2016), 071101.

[88] Schreiber, Jörg. *Applications of laser-driven particle acceleration - Proton spectra*, 2022. `https://www.alpa.physik.uni-muenchen.de/protons.html`, Last accessed on 2022-04-14.

[89] P.A. Kühnemann: *Development of a self-calibrating energy measurement template for laser-driven protons.* Munich, Ludwig-Maximilians-Universität München, Bachelor's thesis, 3 2018.

[90] W. Draxinger: *Entwicklung und Charakterisierung eines Pixeldetektors für laserbeschleunigte Ionen.* Munich, Ludwig-Maximilians-Universität München, Diplomarbeit, 2012.

[91] S. Reinhardt: *Detection of laser-accelerated protons.* Ludwig-Maximilians-Universität München, Dissertation, 6 2012.

[92] S. Reinhardt, W. Draxinger, J. Schreiber und W. Assmann, *Journal of Instrumentation* **8** (2013), P03008.

[93] F. Lindner: *Online Diagnostics for Laser Accelerated Ions and Electrons.* Munich, Ludwig-Maximilians-Universität München, Master's thesis, 11 2015.

[94] F.H. Lindner, J.H. Bin, F. Englbrecht, D. Haffa, P.R. Bolton, Y. Gao, J. Hartmann, P. Hilz, C. Kreuzer, T.M. Ostermayr, T.F. Rösch, M. Speicher, K. Parodi, P.G. Thirolf und J. Schreiber, *Review of Scientific Instruments* **89** (2018), 013301.

[95] T. Graeve und G.P. Weckler: *High-resolution CMOS imaging detector. High-resolution CMOS imaging detector*, In *Medical Imaging 2001: Physics of Medical Imaging*, volume 4320. SPIE (2001) pages 68–76.

[96] H. Spieler: *Semiconductor Detector Systems.* Clarendon Press, Oxford, 2005.

[97] P. Zyla et al. , *PTEP* **2020** (2020), 083C01.

[98] J.D. Jackson, *Phys. Rev. D* **59** (1998), 017301.

[99] A. Rotondi und P. Montagna, *Nuclear Instruments and Methods in Physics Research Section B: Beam Interactions with Materials and Atoms* **47** (1990), 215.

[100] I. Henins, *Journal of Research of the National Bureau of Standards. Section A, Physics and Chemistry* **68** (1964), 529.

[101] L.D. Landau: *Collected papers of LD Landau.* Pergamon, 1965. 56. On the energy loss of fast particles by ionisation.

[102] H. Bichsel, *Rev. Mod. Phys.* **60** (1988), 663.

[103] P. Vavilov, *Soviet Phys. JETP* **5** (1957).

[104] R. Brun und F. Rademakers, *Nuclear Instruments and Methods in Physics Research Section A: accelerators, spectrometers, detectors and associated equipment* **389** (1997), 81.

[105] Pohl, David-Leon. *ROOT Reference Guide, Vavilov Class Reference*, 2022. `https://root.cern/doc/master/classROOT_1_1Math_1_1Vavilov.html`, Last accessed on 2022-03-01.

[106] D.E. Groom und S. Klein, *The European Physical Journal C-Particles and Fields* **15** (2000), 163.

[107] J.F. Ziegler, M.D. Ziegler und J.P. Biersack, *Nuclear Instruments and Methods in Physics Research Section B: Beam Interactions with Materials and Atoms* **268** (2010), 1818.

[108] David-Leon Pohl. *pylandau python package*, 2017. `https://github.com/SiLab-Bonn/pylandau`, Last accessed on 2022-03-01.

[109] T. Bortfeld, *Medical Physics* **24** (1997), 2024.

[110] P. Wang, Z. Gong, S.G. Lee, Y. Shou, Y. Geng, C. Jeon, I.J. Kim, H.W. Lee, J.W. Yoon, J.H. Sung et al. , *Physical Review X* **11** (2021), 021049.

[111] K. Schnürle, J. Bortfeldt, F.S. Englbrecht, C. Gianoli, J. Hartmann, S. Meyer, K. Niepel, G. Landry, I. Yohannes, J. Schreiber, K. Parodi und M. Würl: *Entwicklung von Protonenbildgebung mit einem einzelnen integrierenden CMOS-Detektor für eine Kleintierbestrahlungsanlage. Entwicklung von Protonenbildgebung mit einem einzelnen integrierenden CMOS-Detektor für eine Kleintierbestrahlungsanlage*, In *51. Jahrestagung der Deutschen Gesellschaft für Medizinische Physik - Abstractband*, herausgegeben von U. Wolf und B. Sattler. (2020).

[112] P. Bolton, K. Parodi und J. Schreiber: *Applications of laser-driven particle acceleration.* CRC Press, 2018.

[113] A. McIlvenny, D. Doria, L. Romagnani, H. Ahmed, N. Booth, E.J. Ditter, O. Ettlinger, G. Hicks, P. Martin, G.G. Scott et al. , *Physical Review Letters* **127** (2021), 194801.

[114] W. Ma, I.J. Kim, J. Yu, I.W. Choi, P. Singh, H.W. Lee, J.H. Sung, S.K. Lee, C. Lin, Q. Liao et al. , *Physical Review Letters* **122** (2019), 014803.

[115] F. Balling, S. Gerlach, A.K. Schmidt, V. Bagnoud, J. Hornung, B. Zielbauer, K. Parodi und J. Schreiber: *First tests of the I-BEAT detector as primary monitor for target normal sheath accelerated protons. First tests of the I-BEAT detector as primary monitor for target normal sheath accelerated protons*, In *Laser Acceleration of Electrons, Protons, and Ions VI*, volume 11779. International Society for Optics and Photonics (2021) page 117790T.

[116] Rapidobject GmbH. *Rapidobject GmbH*, 2022. `https://www.rapidobject.com/3d-druck-materialien/kunststoffe/`, Last accessed on 2022-04-22.

[117] F. Balling: *Test of dynamic range extension of the RadEye sensor using a laser diode*. Munich, Ludwig-Maximilians-Universität München, Bachelor's thesis, 6 2017.

Danksagung

Ich möchte allen danken die diese Arbeit möglich gemacht haben. Zuerst Prof. Dr. Jörg Schreiber für die Betreuung, die immer inspirierenden Diskussionen und die gelegentlichen aufmunternden Worte während dieser Zeit. Vielen Dank an Prof. Dr. Peter Thirolf für die Übernahme der Zweitkorrektur dieser Arbeit.

Mein Dank gebührt ebenfalls den 'Eternals', die mich die ganze Zeit über begleitet haben: Johannes Gebhard, Martin Speicher und Thomas Rösch für die unermüdliche Unterstützung insbesondere während der CALA Aufbauphase und den Strahlzeiten. Leonard Doyle ebenso für seinen großen Einsatz in und um LION. Danke Felix Balling, Sonja Gerlach, Anna-Katharina Schmidt und Julia Liese für die 'Übernahme', die stetige Motivation und den Drang die Experimente zu verbessern. Ebenfalls großes Dankeschön für die vielen Cappuccinos. Für die Unterstützung während des Aufbaus möchte ich mich bei Pablo Kühnemann für die PABLONE und Matthew S'ng für die Arbeit an CM49 bedanken. Während der ersten CALA Experimente konnte ich mich ausserdem immer auf Mark Berndl, Lotta Flaig und Luisa Tischendorf verlassen, danke dafür.

Ein großes Danke gilt auch Daniel Haffa, der während seiner Arbeit in LEX grundlegende Teile von CALA und LION vorbereitet und aufgebaut hat. Während der LEX - CALA Übergangszeit konnte ich viel von Jianhui Bin, Ying Gao, Christian Kreuzer und Paul Bolton lernen, insbesondere möchte ich mich bei Peter Hilz und Tobias Ostermayr für die Gelegenheiten bedanken an externen Strahlzeiten teilzunehmen. Gefreut habe ich mich ebenfalls sehr über meine Bürokollegen Florian Lindner und Alexander Prasselsberger.

Danke an die Gruppe um Prof. Dr. Katia Parodi, insbesondere Franz Englbrecht für seine Hilfe mit Detektoren, Simulationen und die Gespräche während der letzten Wochen. Kathrin Schnürle und Matthias Würl für Diskussionen über den CM49 und anderen Detektoren, sowie für die Bereitstellung des Plastik-Phantoms.

Stellvertretend für die AG Karsch möchte ich Stefan Karsch, Gregor Schilling und Moritz Förster für die Arbeit an ATLAS, sowie für die vielen lehreichen Stunden im Laserlabor danken. Danke an das Targetlabor von Jerzy Szerypo für die Herstellung der ganzen Folien, sowie Daniel Hahner für die Diskussionen über deren Feinheiten. Ebenfalls danken möchte ich der HF-Gruppe, Erin Grace Fitzpatrik, Laura Geulig und Kilian Unterguggenberger.

Vielen lieben Dank an das Team um Hans Wirth das den täglichen Betrieb von CALA betreut: An Nikolce Gjotev und Oliver Gosau für alles technische im und ums

Vakuum sowie viel How-To Wissen um von einer Idee zu einer Umsetzung zu kommen. An Florian Saran für die Unterstützung beim Kranfahren und all die vielen kleinen Dinge die einem manchmal gar nicht bewusst sind. Und an Andreas Bär stellvertretend für die Instandhaltung der geheimnisvollen Technikzentrale. Ebenfalls danke an die Konstruktionsabteilung um Johannes Wulz und der großartigen Mechanischen Werkstatt um Rolf Öhm.

Zu guter letzt möchte ich meiner Familie danken, insbesondere meiner Freundin, meiner Schwester und meinen Eltern für deren anhaltende Unterstützung.